WAVE INTERACTIONS WITH ARRAYS OF VERTICAL BOTTOM-MOUNTED DEFORMABLE CYLINDERS

A Thesis

by

QILIN XU

Submitted to the Office of Graduate and Professional Studies of
Texas A&M University
in partial fulfillment of the requirements for the degree of

MASTER OF SCIENCE

Chair of Committee,	Richard S. Mercier
Committee Members,	Hamn-Ching Chen
	Prabir Daripa
Head of Department,	Sharath Girimaji

May 2017

Major Subject: Ocean Engineering

ABSTRACT

This thesis describes research regarding the trapping of water waves through hydro-elastic interaction with bottom-mounted cylinder arrays in shallow water. A modal decomposition and superposition approach has been applied to the calculation of the hydro-elastic response of arrays of deformable cylinders exposed to incident long waves. The cylinder array is considered as an effective medium, and the theory associated with the Fabry-Pérot Interferometer is applied. Therefore, the refraction index within the array and the transmittance and reflectance by the array can be determined. Equations of motion for a single deformable cylinder are derived from the theory of vibration for thin shells, and added mass, radiation damping and stiffness matrices are defined. Analytical solutions for the response of a single deformable cylinder are calculated and compared with the numerical results from WAMIT. The results show a good agreement. Transmission and reflection coefficients for rigid cylinder arrays have been calculated based on effective medium theory and found to match those determined from WAMIT. The final step of the research involves investigating the hydro-elastic response of deformable cylinder arrays exposed to incident waves. Wave interactions of arrays of elastic cylinders that can expand and contract radially are simulated using WAMIT, and the associated wave fields within and outside the array are analyzed and discussed.

The main objective of this research is to investigate whether significant "wave trapping" can occur when waves encounter elastic cylinders arranged in periodic or random arrays. If the insertion loss calculated in the case of flexible cylinder arrays is significant, one may conclude that in shallow water those arrays could attenuate incident long waves of certain frequencies. The research is motivated by analogous theories of wave trapping that can occur when acoustic waves encounter bubbly media, such as breaking water waves. Furthermore, such arrangement of pulsating cylinders may lead to

novel ways of extracting wave energy through hydro-mechanical coupling with suitable devices.

ACKNOWLEDGEMENTS

I would like to thank my committee chair, Dr. Richard S. Mercier, for his guidance and kind support throughout my research. I am grateful for the effort he made and the encouragement he gave me. I would also like to thank my committee members, Dr. Hamn-Ching Chen and Dr. Prabir Daripa, for their great help during my research.

Thanks also go to my friends and colleagues and the faculty and staff at Department of Ocean Engineering for making my time at Texas A&M University an amazing experience.

Finally, thanks to my parents for their supports and encouragements throughout my study at Texas A&M University.

TABLE OF CONTENTS

Page

LIST OF FIGURES

LIST OF TABLES

1. INTRODUCTION

The interaction between water waves and arrays of bottom-mounted cylinders has become more important and much work has been done in this field. Most of the interest is stimulated by the fact that the wave effect on cylindrical supporting columns of oil platforms plays an important role in engineering design. It is known that when incident waves of certain frequencies encounter finite periodic linear arrays or circular arrays of cylinders, resonant interactions may occur, which leads to a near-trapping of water waves (Evans and Porter, 1997). In particular, pure wave trapping exists for the case of infinite linear arrays.

The scope of this research is limited to wave interactions with large periodic arrays of bottom-mounted deformable cylinders. In the long wavelength limit, periodic arrays of rigid cylinders can behave like an effective medium during wave transmission and reflection processes (Hu and Chan, 2005). The effective depth and a renormalized gravitational constant inside the medium can be different from outside. Hu and Chan (2005) investigated this phenomenon and derived the analytic formulas for those effective parameters, which are proved to be very useful in analyzing wave refraction, reflection, and transmission processes. The Fabry-Pérot effect is invoked in Hu and Chan's (2005) theory to describe modal reflection transmission by a cylinder array. Therefore, the theory associated with the Fabry-Pérot Interferometer, which is an optical device, has been used in this study to account for multiple reflections and transmissions, and the reflectance and transmittance of the entire array can be determined. In addition, for the array of finite length, the far ends of the arrays may exert a so-called "tip effect" on the wave field. The effect can cause a distortion of the wave crests and troughs near the tips, while the middle area of the array is less affected and can be called the "shadow zone". The "tip effect" is of special importance in analyzing the wave interactions with large cylinder arrays. By

investigating the “tip effect” we can understand how the intensities of reflection and transmission vary in different parts of the wave domain, especially in the area close to and far from the tip. It also reveals that for cylinder arrays of different lengths, the wave field responds differently when the wave propagates through the tip.

In the field of acoustics, it is well-studied that acoustic pulses can be trapped when the waves are transmitted by a system of random bubbly water. As a result, air bubbles in water have been used for the mitigation of underwater acoustic noise that is in the low frequency range (Lee et al., 2011). The trapping of pulses will occur regardless of the configuration of randomly spaced bubbles, but the degree of trapping is highly sensitive to the frequencies of incident acoustic signals (Wang and Ye, 2001).

The motivation of this thesis is to investigate the analogous theories of trapping and localization of acoustic waves and water waves. If the presence of air bubbles could cause the attenuation of acoustic pulses, one can expect a similar effect in the case of deformable cylinders and water waves. Elastic cylinders can function as air bubbles in the water, and the deformation of the cylinders may be simulated from the theory for the vibration of thin shells with proper choice of boundary conditions. Because of the trapping and reflecting of waves, elastic cylinder arrays can be used in designing coastal protection structures, such as offshore breakwaters. Arrays of elastic cylinders may also be used to improve the efficiency of wave energy extraction devices.

1.1. Research Objectives

The research plan is organized around three main research objectives:

- Investigate the interaction between incident long waves and arrays of bottom-mounted rigid cylinders using the effective medium approach to validate the setup of the WAMIT model.
- For purposes of verifying the setup of the WAMIT model, formulate analytical

solutions of the hydro-elastic response of a single deformable cylinder exposed to incident waves using the modal superposition and decomposition approach.

- Investigate the interaction between incident long waves and arrays of bottom-mounted deformable cylinders to quantify the insertion loss.

The research work can be divided into three phases that correspond to the above three objectives, respectively.

1.1.1. Arrays of bottom-mounted rigid cylinders

For the first phase of an array of rigid cylinders, WAMIT is used to generate the detailed wave fields on either side and within rectangular arrays of rigid cylinders. The reflection and transmission coefficients associated with the wave fields are identified using least-squares minimization, specifically using the pseudo-inverse method. The identified reflection and transmission coefficients from the WAMIT results are compared with the result calculated by the effective medium approach.

1.1.2. One single deformable cylinder

Generalized modes corresponding to deformations of the cylinder's surface will be formulated. WAMIT's Fortran subroutine code is then modified to incorporate the generalized modes into the hydro-elastic analysis. Equations of motion for a single deformable cylinder are developed and expressed from the Donnell-Mushtari theory of vibration for thin shells, and mass and stiffness matrices are defined. Those equations are formulated in matrix form consistent with the generalized modes. Using the analytical expressions for the diffraction and radiation potentials, the expressions for added mass, radiation damping, and exciting force can be formulated. The next steps include comparing the analytical solutions with numerical results from WAMIT. Those solutions are also validated with the results for the vibration of a fluid-filled cylinder in air. Material

properties are selected to set the “breathing” mode natural period of the cylinder at the lower end of studied wave periods.

1.1.3. Arrays of bottom-mounted deformable cylinders

Upon successful completion of the second phase, the last part of the research is conducted. Hydro-elastic analysis of periodic arrays of deformable cylinders exposed to incident long waves are performed using WAMIT. Then the reflection and transmission process of the array is described analytically with the same approach applied in the case of arrays of rigid cylinders. Finally, surface elevations are plotted and the relation between radiation and scattering problems is verified by Newman’s (1975) procedure. Observations are made to study the degree to which the wave amplitudes may be attenuated, and hence to determine whether the trapping of waves is achieved.

1.2. Literature Review

The scattering of water waves by bottom-mounted cylinder arrays has been studied previously by many researchers in the field. For example, Evans and Porter (1997) examined the trapping of waves when waves interact with several different arrangements of bottom-mounted rigid cylinders, including a circular arrangement, finite linear arrays, and infinite periodic arrays.

Using an effective water medium approach, Hu and Chan (2005) demonstrated that long water waves propagate through an array of bottom-mounted cylinders as if it is a uniform medium with an effective depth and gravitational constant. They defined an effective refractive index which can be used with the Snell refractive law to model the reflection and refraction of long waves encountering the array.

In the field of acoustics, the effects of air bubbles in water are well known. Junger and Cole (1980) investigated sound propagation in bubble swarms. They analyzed a

system that contains a force-excited, extended plate radiating acoustic waves through an air bubble swarm into the ambient liquid. A formulation of the Insertion Loss (IL) for various frequency ranges was then given by comparing the difference of far-field pressures with and without the bubble swarm.

Commander and Prosperetti (1989) reviewed a model of the propagation of pressure waves in bubbly liquids which was proposed by Van Wijngaarden (1968). They validated the model using experimental data of linear acoustic wave propagation and attenuation in bubbly liquids. Moreover, as a step toward the application of Commander and Prosperetti's theory, Lee et al. (2011) conducted an experiment that showed that large tethered encapsulated bubbles could be used for the attenuation of low frequency under water noise, which further validated Commander and Prosperetti's model experimentally.

Leissa (1973) organized and discussed the main theories associated with the vibration of shells in a NASA report. One of those theories, the Donnell-Mushtari theory, will be used in the derivation of the equations of motion in the present study. Dean and Dalrymple (1991) gave an analytical solution for the radiation potential of different types of cylindrical wavemakers that satisfy different boundary conditions. In the present research of hydro-elastic response of a deformable cylinder, the expression for the velocity potential of the pulsating wavemaker in Dean and Dalrymple's theory will be used.

Newman (1994) developed a general methodology for modeling hydro-elastic wave-body interactions by specifying generalized modal shape functions in addition to conventional six rigid-body modes. The analysis of three-dimensional wave radiation and diffraction by rigid bodies can thereby be extended to deformable bodies. Similar procedures will be applied in the derivation of the added mass, radiation damping, hydrostatic stiffness, and wave exciting force for the pulsating cylinder.

The analytical models for the hydro-elastic response of a single cylinder can be verified through comparison with results from other studies. Goncalves and Ramos (1996)

investigated the dynamic behavior of cylindrical tanks that are partially filled with liquid. Koga and Tsushima (1990) gave a method to calculate the natural frequency of the breathing vibration of thin shells partially filled with liquids.

1.3. Organization of Thesis

This thesis is organized in a section-subsection format.

Section 1 provides an introduction and background information of this thesis, a review of the literature, the research objectives, and the organization of this thesis.

Section 2 discusses the effective medium approach used in the analysis of wave interactions with arrays of rigid cylinders. The theory associated with Fabry-Pérot interferometry is also introduced in the calculation of transmittance and reflectance of the arrays. Data output from WAMIT is presented and compared with the results generated from the effective medium approach. Moreover, this section includes an analysis of the so-called “tip effect” which can be seen at the ends of the arrays.

Section 3 gives the analysis of the hydro-elastic response of vertical deformable cylinders exposed to incident waves. This section develops the analytical model for the cylinder considered, and then gives a brief introduction of the software WAMIT used in the project. Next, the numerical data is discussed, and the model selection process is outlined.

Section 4 presents the cases of regular arrays of deformable cylinders. The methods and approaches discussed in Section 2 and Section 3 are combined and applied to the analysis of wave interactions with elastic cylinder arrays. Numerical results from WAMIT will be presented and discussed.

Section 5 consists of a summary and conclusions of the research. Suggestions for possible future work related to this research will also be included in this section.

2. ARRAYS OF BOTTOM-MOUNTED RIGID CYLINDERS

In this section, the effective medium approach developed by Hu and Chan (2005) and the effect of the Fabry-Pérot interferometer will be introduced. An integration of the theories will lead to the analytical formulation for the reflectance and the transmittance of an array of rigid cylinders with the presence of multiple reflections inside the array. The pseudo-inverse method used to provide the reflectance and transmittance from WAMIT's output of surface elevation will be also presented.

A number of cases of regular arrays of uniformly spaced rigid cylinder are implemented in WAMIT. In the first step of validating the refractive index, WAMIT has been exercised for cases with five different filling ratios. Then a set of cylinder arrays with the same filling ratio but different lengths are studied in order to find the relationship between the effective width of the array and the diffraction coefficients. Once the reflectance and transmittance associated with WAMIT's calculation are determined, they will be compared with the theoretical results derived from the effective medium approach and the theory of the Fabry-Pérot interferometer.

In order to investigate the so-called "tip effect" which can be observed at the ends of cylinder arrays, five different arrays of cylinders are studied and proper grid points are chosen to calculate the surface elevation for the wave field diffracted by the arrays. The purpose is to find the correlation between the intensity of the "tip effect" and the lengths of arrays. Furthermore, a separate case of 11 by 80 cylinders is executed for four different incident wave periods.

For those cases mentioned above, WAMIT's high-order method has been used to define the geometry of the cylinder. The body surface is defined by patches, and the number of patches specified in the Geometric Definition File (GDF) is set to be the same

as the number of cylinders in each case. The arrays are considered as one single body with two planes of symmetries in the X and Y directions.

2.1. Effective Medium Approach

For long waves, a periodic bottom-mounted cylinder array can be treated as an effective medium which has an effective gravitational constant g_e, effective wavenumber k_e and an effective water depth h_e inside the medium. Those parameters depend on the filling ratio f_s of the cylinders which can be defined as (Hu and Chan, 2005):

$$f_s = \frac{volume\ \ of\ \ cylinder}{volume\ \ of\ \ medium} \tag{2.1}$$

For a square water column with surface area of a^2, which is pierced by a circular cylinder with radius r, the filling ratio f_s of this effective medium is $\frac{\pi r^2}{a^2}$. The effective medium can also be defined as a circular water column with surface area of πr_e^2. The filling ratio is independent of the total number of cylinders used for calculation. For an array of *N* identical cylinders, the value of the filling ratio will be the same as that of one single cylinder:

$$f_s = \frac{N\pi r^2}{Na^2} = \frac{\pi r^2}{a^2} \tag{2.2}$$

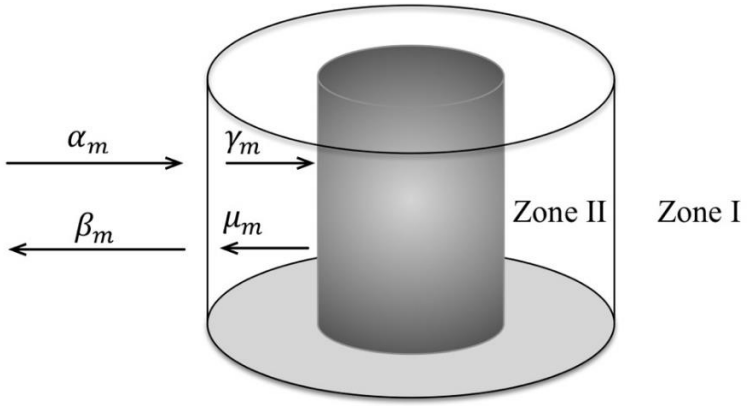

Figure 2.1. Water column pierced by a vertical rigid cylinder. Zone II is the effective medium.

Consider a circular water column with radius $R = a/\sqrt{\pi}$ pierced by a rigid circular cylinder with radius *r*. The system forms an effective medium with effective gravitational constant g_e, effective wavenumber k_e and an effective water depth h_e. A schematic diagram of the effective medium is presented in Figure 2.1. Zone I is the outside water zone and zone II is defined as the effective medium. In zone I, α_m and β_m are the amplitudes of the incident and scattered waves, respectively, while in zone II γ_m and μ_m are respectively the amplitudes of the incident and scattered waves. For harmonic water waves of frequency ω, the vertical displacement of the water surface is governed by the two-dimensional Helmholtz equations:

$$(\nabla^2 + k^2)\eta = 0 \tag{2.3}$$

where *k* is the wave number which can be obtained from the dispersion relation:

$$\omega^2 = gktanh(kh) \tag{2.4}$$

Assuming the water depth is shallow, the above equation can be simplified as:

$$\omega^2 = ghk^2 \tag{2.5}$$

Substituting equation (2.5) into equation (2.3), the Helmholtz equation becomes:

$$\nabla(h\nabla\eta) + \frac{\omega^2}{g}\eta = 0 \tag{2.6}$$

In cylindrical coordinates (ρ, ϕ), the solutions of equation (2.6) in zone I can be written as a linear combination of first kind Bessel functions and Hankel functions：

$$\eta^{\mathrm{I}} = \sum_{m=0}^{\infty} [\alpha_m J_m(k\rho) + \beta_m H_m(k\rho)]\, e^{im\phi} \tag{2.7}$$

Similarly, the solution in zone II can be written as:

$$\eta^{\mathrm{II}} = \sum_{m=0}^{\infty} [\gamma_m J_m(k_e\rho) + \mu_m H_m(k_e\rho)]\, e^{im\phi} \tag{2.8}$$

The first kind Bessel function J_m represents the incident waves, while the Hankel function H_m represents the scattering waves. At the surface of the cylinder, the boundary condition implies no flow through the cylinder wall:

$$\frac{\partial \eta}{\partial \vec{n}} = 0 \tag{2.9}$$

where $\vec{n}$ is the direction of the normal to the surface wall. In cylindrical coordinates, the boundary condition takes the form of $\frac{\partial \eta}{\partial \rho} = 0$. The continuities of η and $\mathrm{h}\frac{\partial \eta}{\partial \rho}$ at $\rho = R$ imply:

$$\eta^{\mathrm{I}}(R) = \eta^{\mathrm{II}}(R) \tag{2.10}$$

$$\mathrm{h}\frac{\partial \eta^{\mathrm{I}}(R)}{\partial \rho} = \mathrm{h}_e \frac{\partial \eta^{\mathrm{II}}(R)}{\partial \rho} \tag{2.11}$$

Expanding equation (2.10) and equation (2.11) using the analytical representations of η^{I} and η^{II}:

$$\begin{aligned} -\mathrm{hk} J_m(k_e R)[H'_m(k_e R)J'_m(kr) - J'_m(kR)H'_m(kr)] \\ + \mathrm{h}_e k_e J'_m(k_e R)[J'_m(kr)H_m(kR) \\ - H'_m(kr)J_m(kR)] = 0 \end{aligned} \tag{2.12}$$

Assuming the wave is long enough ($ka \ll 1$), the above equation can be simplified as:

$$h_e k_e^2 - (1 - f_s)hk^2 = 0 \quad \text{when } \mathrm{m} = 0 \tag{2.13}$$

$$h_e - h\frac{1 - f_s^m}{1 + f_s^m} = 0 \quad \text{when } \mathrm{m} \geq 1 \tag{2.14}$$

From the dispersion relationship in shallow water, the expressions for the wavenumbers in zone I and zone II can be determined as:

$$k_e = \frac{\omega}{\sqrt{g_e h_e}} \tag{2.15}$$

$$k = \frac{\omega}{\sqrt{gh}} \tag{2.16}$$

Substituting equation (2.15) into the non-reflection conditions for *m*=0 and *m*=1 gives the analytical expressions for g_e and h_e, respectively:

$$g_e = \frac{1}{1-f_s} g \tag{2.17}$$

$$h_e = \frac{1-f_s}{1+f_s} h \tag{2.18}$$

Combining equations (2.15) through equation (2.18), the wavenumber inside the effective medium can be obtained as:

$$k_e = n_e k \tag{2.19}$$

where $n_e = \sqrt{1+f_s}$ is the effective index of the medium. It can be used to determine the refractive angle using Snell's Law:

$$sin\theta = n_e sin\varphi \tag{2.20}$$

Using the continuities of η and $\mathrm{h}\frac{\partial \eta}{\partial \rho}$ at $\rho = R$, the amplitude reflection coefficient and the amplitude transmission coefficient can be obtained as:

$$r_a = \frac{cos\theta - cos\varphi \dfrac{1-f_s}{\sqrt{1+f_s}}}{cos\theta + cos\varphi \dfrac{1-f_s}{\sqrt{1+f_s}}} \tag{2.21}$$

$$t_a = \frac{2cos\theta}{cos\theta + cos\varphi \dfrac{1-f_s}{\sqrt{1+f_s}}} \tag{2.22}$$

These expressions will be used to determine the transmission and reflection intensities of the arrays, and further compared with those determined from WAMIT. Moreover, the Brewster angle, which leads to non-reflection, is given as:

$$\theta_0 = arccos\frac{1-f_s}{2} \tag{2.23}$$

By using the effective medium approach, one can determine the transmission and reflection coefficients of the array and further describe the refraction process analytically (Hu and Chan, 2005).

2.2. Fabry–Pérot Interferometer

In optics, a Fabry–Pérot interferometer is typically made of a transparent plate with two reflecting surfaces, or two parallel highly reflecting mirrors. Its transmission spectrum as a function of wavelength exhibits peaks of large transmission corresponding to resonances of the etalon. From the theory of the Fabry–Pérot interferometer, one can determine the reflectance and transmittance of cylinder arrays, and then the amplitudes of reflected and transmitted waves.

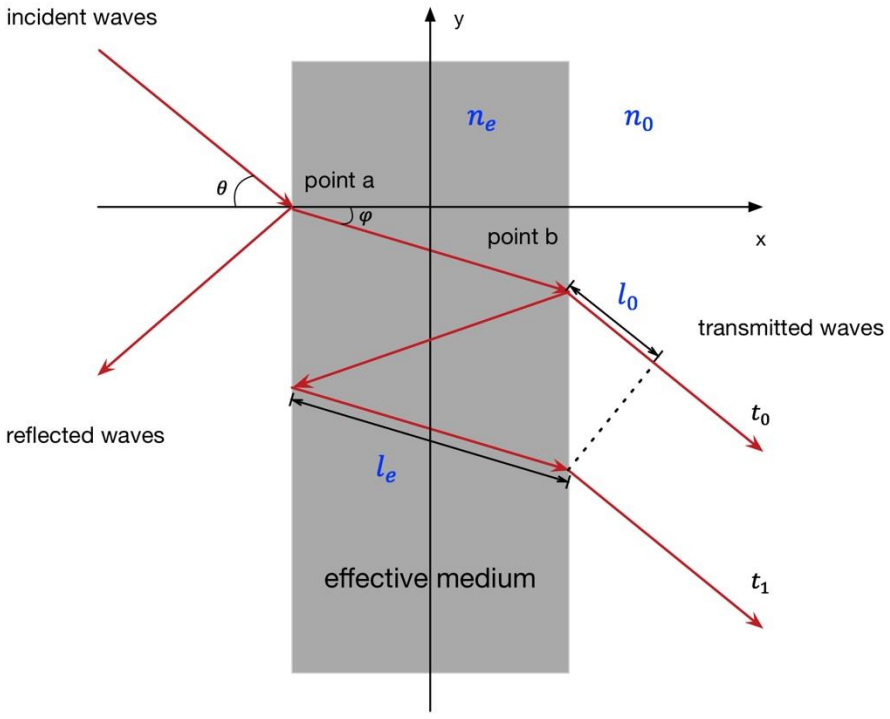

Figure 2.2. Multiple reflections and transmissions inside a Fabry-Pérot interferometer.

The system considered is shown in Figure 2.2. The Fabry–Pérot interferometer has two reflecting surfaces. The transmittance *T* and reflectance *R* of the device can be written as follow:

$$T = {t_a}^2 \tag{2.24}$$

$$R = {r_a}^2 \tag{2.25}$$

The conservation of energy requires $T+R=1$.The incident beam of unit amplitude propagates from the left and meets the first boundary with an angle θ. A part of the beam is reflected and the other part is transmitted into the interferometer. When the transmitted beam hits the second plate, part of it is transmitted and becomes the first beam on the right. The other part of the incident beam is reflected twice at the boundaries, and then transmitted through the interface on the right. At each reflection, the amplitude of the beam is reduced by $\sqrt{T}$, while the transmission through the boundary causes the amplitude to reduce by $\sqrt{R}$.

It can be seen from the figure that the phase lag between t_0 and the incident beam is $e^{ik_e l_e}$. Therefore, the transmitted beam at point b is:

$$t_0 = Te^{ik_e l_e} \tag{2.26}$$

Because the second transmitted beam t_1 has met the second plate three times, the phase lag between t_1 and the incident beam is $e^{3ik_e l_e - ik_0 l_0}$. Hence, t_1 can be represented as follows:

$$t_1 = tr^2 t(e^{3ik_e l_e - ik_0 l_0}) = TR(e^{3ik_e l_e - ik_0 l_0}) \tag{2.27}$$

The total phase difference between t_0 and t_1 is:

$$\delta = 3k_e l_e - k_0 l_0 - k_e l_e = 2k_e l_e - k_0 l_0 \tag{2.28}$$

More generally, the n^{th} transmitted beam can be written as:

$$t_n = TR^n e^{in\delta} \tag{2.29}$$

Using the Snell's Law ($sin\theta = n_e sin\varphi$), the phase difference can be rewritten as:

$$\delta = 2k_e l_e - k_0 l_0 = 2k_e l cos\varphi \tag{2.30}$$

The total transmitted amplitude is the sum of all individual beams' amplitudes:

$$A_t = \sum_{n=0}^{\infty} t_n = T \sum_{n=0}^{\infty} (Re^{i\delta})^n = \frac{T}{1 - Re^{i\delta}} \tag{2.31}$$

The intensity of the transmitted beam will be just A_t times its complex conjugate:

$$T_e = A_t A_t^* = \frac{(1-R)^2}{1 + R^2 - 2Rcos\delta} \tag{2.32}$$

Therefore, the transmitted wave amplitude can be written as:

$$a_t = \sqrt{T_e} = \frac{(1-R)}{\sqrt{1 + R^2 - 2Rcos\delta}} \tag{2.33}$$

The reflected intensity is:

$$R_e = 1 - \frac{(1-R)^2}{1 + R^2 - 2Rcos\delta} \tag{2.34}$$

and the reflected wave amplitude is determined as:

$$a_r = \sqrt{R_e} = \sqrt{1 - \frac{(1-R)^2}{1 + R^2 - 2Rcos\delta}} \tag{2.35}$$

Equation (2.33) and (2.35) will be used to predict the theoretical values of the transmitted and reflected wave amplitudes, and to compare with the results determined from WAMIT's numerical output.

2.3. Parameter Estimation using Pseudo-inverse Method

The pseudo-inverse of an arbitrary matrix is a generalization of the inverse matrix, which can be used to estimate the values of parameters for a statistical model to make the

agreement of the model and data reach maximum. The pseudo-inverse method is applied in this research to determine the reflection and transmission coefficients of the wave field from WAMIT's numerical results of wave elevation. The pseudo-inverse can be expressed from the singular value decomposition (SVD) of a $m \times n$ matrix A:

$$A = U \begin{pmatrix} S & 0 \\ 0 & 0 \end{pmatrix} V \tag{2.36}$$

where U and V are orthogonal matrices, and S is a diagonal matrix containing the singular values of *A*. The pseudo-inverse of *A* can be defined as:

$$A^{+} = V \begin{pmatrix} S^{-1} & 0 \\ 0 & 0 \end{pmatrix} U^{T} \tag{2.37}$$

If $rank(A) = n \leq m$, then we have the following expression:

$$A^{+} = (A^{T}A)^{-1}A^{T} \tag{2.38}$$

The solution to the least-squares problem $\min_{x} \|Ax - B\|_2$ can be expressed as:

$$x = A^{+}B \tag{2.39}$$

The data set from WAMIT can be decomposed as:

$$B_i = A_{ij}X_j + e_i \tag{2.40}$$

where B_i corresponds to the wave elevation data set from WAMIT, e_i is the error, and $A_{ij}X_j$ is the theoretical linear wave elevation. Equation (2.40) can be written in matrix notation:

$$\{B\} = [A]\{X\} + \{e\} \tag{2.41}$$

Using the pseudo-inverse method and applying equations (2.38) and (2.39), $\{X\}$ is solved as:

$$\{X\} = ([A]^{T}[A])^{-1}[A]^{T}\{B\} \tag{2.42}$$

The above equation will be used in the calculation of the unknowns in the studied wave domain, which can be decomposed into three zones shown in Figure 2.3. Zone 1

contains the incident wave and the reflected wave from the first edge of the effective medium. Zone 2 is the array of cylinders and the effective medium zone, which contains both the reflected wave from the second edge and the transmitted wave from the first edge. Zone 3 only contains the transmitted wave from the second edge.

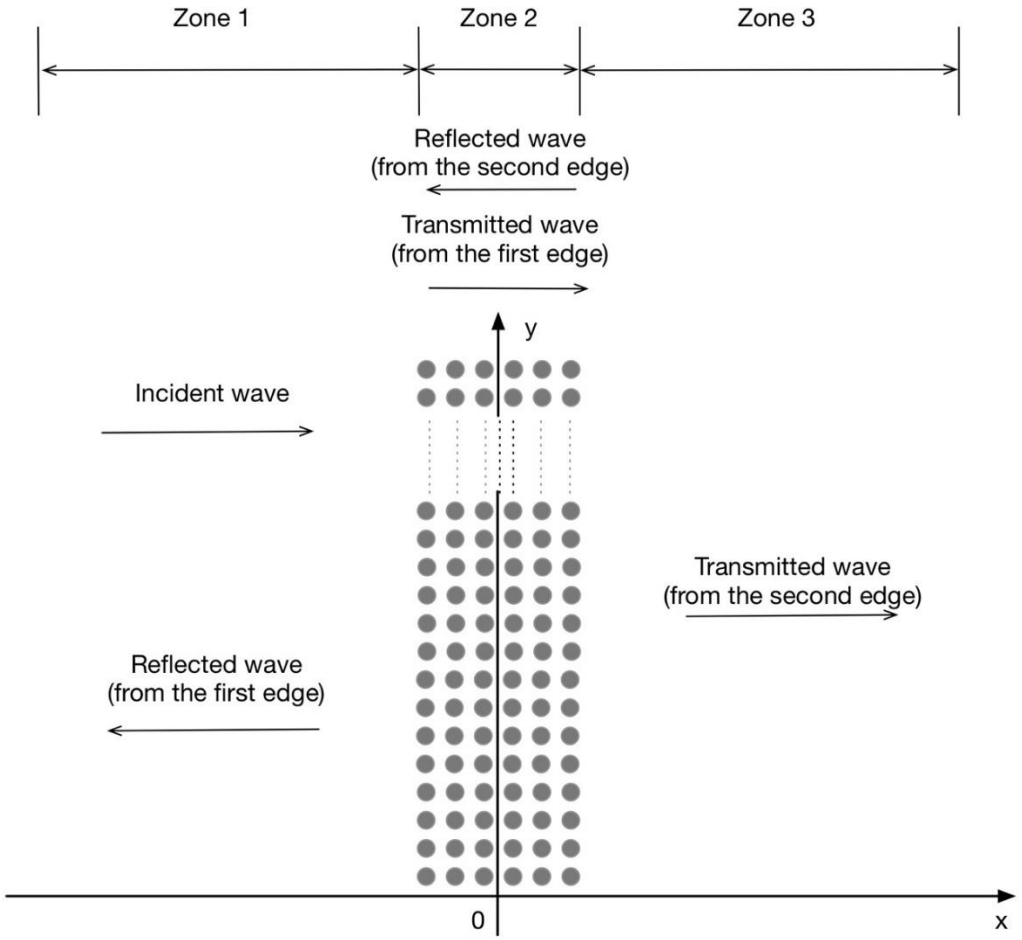

Figure 2.3. Decomposition of the studied wave domain.

Zone 1 & Zone 3:

There are two waves in Zone 1: the incident wave and the reflected wave. The amplitude P_{r1} and phase ε_{r1} of the reflected wave are the unknowns and need to be determined. Therefore, the surface wave elevation in zone 1 can be expressed as:

$$B_i = \cos(k\xi_i) + P_{r1}\cos(k\xi_i' + \varepsilon_{r1}) \tag{2.43}$$

where

$$\xi_i = x_i cos\theta - y_i sin\theta \tag{2.44}$$

$$\xi_i' = x_i cos\theta + y_i sin\theta \tag{2.45}$$

Using decomposition for the cosines:

$$\begin{aligned} B_i' &= B_i - \cos(k\xi_i) \\ &= P_{r1}\cos(k\xi_i')\cos(\varepsilon_{r1}) - P_{r1}\sin(k\xi_i')\sin(\varepsilon_{r1}) \end{aligned} \tag{2.46}$$

which can be rewritten in term of matrices:

$$\begin{bmatrix} B_1' \\ B_2' \\ \vdots \\ B_n' \end{bmatrix} = \begin{bmatrix} \cos(k\xi_1') & \sin(k\xi_1') \\ \cos(k\xi_2') & \sin(k\xi_2') \\ \vdots & \vdots \\ \cos(k\xi_n') & \sin(k\xi_n') \end{bmatrix} \begin{bmatrix} X_1 \\ X_2 \end{bmatrix} \tag{2.47}$$

with

$$X_1 = P_{r1}\cos(\varepsilon_{r1}) \tag{2.48}$$

$$X_2 = -P_{r1}\sin(\varepsilon_{r1}) \tag{2.49}$$

We can apply the pseudo-inverse method to find the least-squares solution. {X} can be determined by substituting $\begin{bmatrix} \cos(k\xi_1') & \sin(k\xi_1') \\ \cos(k\xi_2') & \sin(k\xi_2') \\ \vdots & \vdots \\ \cos(k\xi_n') & \sin(k\xi_n') \end{bmatrix}$ for [A] in equation (2.42). Once {X} is solved, the results of P_{r1} and ε_{r1} can be determined as:

$$P_{r1} = \sqrt{{X_1}^2 + {X_2}^2} \tag{2.50}$$

$$\varepsilon_{r1} = \arctan(\frac{-X_2}{X_1}) \tag{2.51}$$

There is only the transmitted wave in Zone 3, and the MLE can be set up in a similar way as in Zone 1. The unknowns are the amplitude of the transmitted wave P_{t3} and its phase ε_{t3}. Applying the pseudo-inverse method in this zone, we have

$$B_i = P_{t3}\cos(k\xi_i' + \varepsilon_{t3}) \tag{2.52}$$

which can be expressed as

$$\begin{bmatrix} B_1 \\ B_2 \\ \vdots \\ B_n \end{bmatrix} = \begin{bmatrix} \cos(k\xi_1') & \sin(k\xi_1') \\ \cos(k\xi_2') & \sin(k\xi_2') \\ \vdots & \vdots \\ \cos(k\xi_n') & \sin(k\xi_n') \end{bmatrix} \begin{bmatrix} X_1 \\ X_2 \end{bmatrix} \tag{2.53}$$

Again, {X} will be solved using equation (2.42). Hence, the desired amplitude P_{t3} and the phase ε_{t3} of the transmitted wave can be determined from:

$$X_1 = P_{t3}\cos(\varepsilon_{t3}) \tag{2.54}$$

$$X_2 = -P_{t3}\sin(\varepsilon_{t3}) \tag{2.55}$$

$$P_{t3} = \sqrt{{X_1}^2 + {X_2}^2} \tag{2.56}$$

$$\varepsilon_{t3} = \arctan\left(\frac{-X_2}{X_1}\right) \tag{2.57}$$

Zone 2:

The effective medium domain contains two waves, which are the transmitted wave and the reflected wave from the second edge of the array. There are six unknowns inside this domain, which are the effective wavenumber k_e, the phase lag φ induced by the reflection and transmission process, the amplitude of the transmitted wave P_{t2}, the amplitude of the reflected wave P_{r2}, the phase of the transmitted wave ε_{t2}, and the phase of the reflected wave ε_{r2}. Both the transmitted wave and reflected waves contribute to the total surface wave elevation. Therefore, the pseudo-inverse method can be set up as:

$$B_i = P_{t2}\cos(k_e\xi_i + \varepsilon_{t2}) + P_{r2}\cos(k_e\xi_i' + \varepsilon_{r2}) \tag{2.58}$$

where

$$\xi_i = x_i cos\theta - y_i sin\theta \tag{2.59}$$

$$\xi_i' = x_i cos\theta + y_i sin\theta$$

Using the decomposition for the cosines, and writing the equation in term of matrices:

$$\begin{bmatrix} B_1 \\ B_2 \\ \vdots \\ B_n \end{bmatrix} = \begin{bmatrix} \cos(k_e\xi_1) & \sin(k_e\xi_1) & \cos(k_e\xi_1') & \sin(k_e\xi_1') \\ \cos(k_e\xi_2) & \sin(k_e\xi_2) & \cos(k_e\xi_2') & \sin(k_e\xi_2') \\ \vdots & \vdots & \vdots & \vdots \\ \cos(k_e\xi_n) & \sin(k_e\xi_n) & \cos(k_e\xi_n') & \sin(k_e\xi_n') \end{bmatrix} \begin{bmatrix} X_1 \\ X_2 \\ X_3 \\ X_4 \end{bmatrix} \tag{2.60}$$

where

$$X_1 = P_{t2}\cos(\varepsilon_{t2}) \tag{2.61}$$

$$X_2 = -P_{t2}\sin(\varepsilon_{t2}) \tag{2.62}$$

$$X_3 = P_{r2}\cos(\varepsilon_{r2}) \tag{2.63}$$

$$X_4 = -P_{r2}\sin(\varepsilon_{r2}) \tag{2.64}$$

{X} can be determined in a similar way as in Zone 1 and Zone 3. The unknowns can thereby be determined:

$$P_{t2} = \sqrt{{X_1}^2 + {X_2}^2} \tag{2.65}$$

$$P_{r2} = \sqrt{{X_3}^2 + {X_4}^2} \tag{2.66}$$

$$\varepsilon_{t2} = \arctan(\frac{-X_2}{X_1}) \tag{2.67}$$

$$\varepsilon_{r2} = \arctan(\frac{-X_4}{X_3}) \tag{2.68}$$

2.4. Modal Superposition Analysis

The idea of modal decomposition and superposition is a powerful method to obtain the solution of free vibration problems. The method is to use free vibration mode shapes to uncouple the equations of motion, which could be further solved independently. Once the solutions are found, the original equation will be solved by a superposition of individual solutions. In this study, we first apply a modal superposition approach in the calculation of the hydro-elastic response of one single elastic cylinder exposed to incident long waves. Then the same approach may be used in the case of periodic and randomly spaced deformable cylinder arrays.

2.5. WAMIT

WAMIT is a radiation/diffraction panel program for analyzing wave interactions with vessels and offshore structures. It has two subprograms, POTEN and FORCE, that are run sequentially. The POTEN program solves for the radiation and diffraction velocity potentials, while FORCE solves for the hydrodynamic coefficients, motions, and forces of the first and second order. The intermediate output file from POTEN is the P2F file. Normally the input files of WAMIT include the configuration files, the Geometric Data File (GDF) that defines the geometry of the body, the Force Control File (FRC) that describes dynamic parameters, and the Potential Control File (POT) that is used to input parameters to POTEN. Figure 2.4 represents the flow chart of WAMIT.

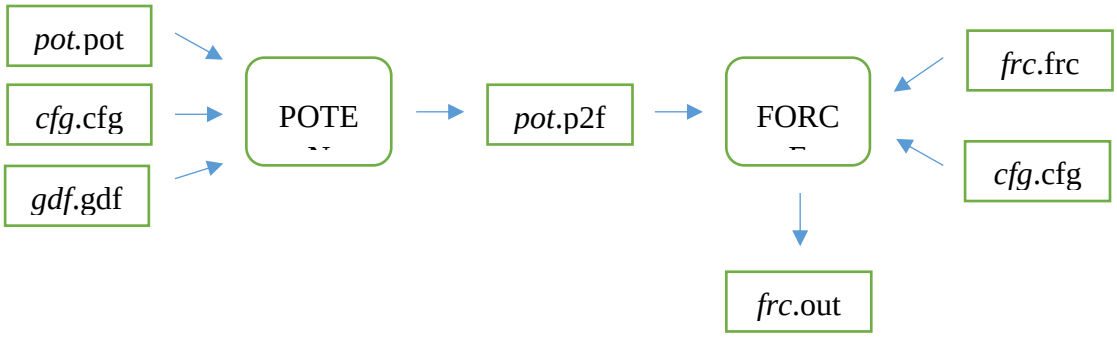

Figure 2.4. Flow chart of WAMIT

2.5.1. Low-order method and high-order method

WAMIT offers two methods, the low-order method and the high-order method, to describe the body geometry. In the low-order method, the body is represented by a set of flat quadrilateral panels. The Cartesian coordinates of of the vertices of each panel are specified in the Geometric Data File (GDF), and hence the geometry of the body can be determined. The velocity potential is evaluated by piecewise constant values on each panel.

In the high-order method, the body geometry can be discretized by panels, B-spline approximations, Multisurf geometry models, and explicit analytical models. The velocity potential is represented by B-splines in a continuous manner, which is different from the low order method. If the desired analytical expression for the geometry is not included in the options given by WAMIT's analytical models, user can modify the GEOMXACT subroutine to define specific geometries. The high-order method provides more accurate solutions with the same number of unknowns.

The high-order method has been used in this project. The body surface of the cylinder arrays is defined by patches where the Cartesian coordinates of the points on each patch are defined by mapping functions. The advantage of this method is that for one patch, the surface is smooth with continuous coordinates and slope.

2.5.2. Single and multiple bodies

WAMIT includes the capability to analyze multiple bodies which interact hydrodynamically and mechanically. Each of the bodies can oscillate independently with up to six degrees of freedom, while additional generalized body modes can be specified. In the present research, a multiple body analysis is applied in the case of diffraction by arrays of deformable cylinders. Each elastic cylinder of the array has been modeled as one single body that oscillates independently. For the case of diffraction by an array of rigid circular cylinders, the entire array was considered as a single body with X = 0 and Y = 0 planes of symmetry.

2.5.3. Generalized body modes

WAMIT's capability of analyzing generalized modes of body motion was used in this research to describe the structural deformations of the cylinders. These modes extend beyond the conventional six degrees of rigid-body translation and rotation. Each generalized mode is defined by specifying the normal velocity in the form:

$$\vec{\varphi}_{jn} = \vec{n}_j = u_j n_x + v_j n_y + w_j n_z \tag{2.69}$$

To incorporate the generalized modes into WAMIT, the Subroutine NEWMODES has been modified according to the deformations of the thin shell.

2.6. Validation of the Definition of the Refractive Index

The first step is to verify WAMIT's calculation of the refractive index before analyzing the refraction process. Six cases of uniformly spaced rigid cylinders exposed to an incident wave of 20s period are studied in this subsection, and the distances between the cylinders are set to be different (30m, 25m, 20m, 15m, 12m and 10m), which correspond to six different filling ratios of 0.0645, 0.0929, 0.1452, 0.2582, 0.4034, and 0.5809, respectively. The free surface elevation can be found in WAMIT's numerical .6p

output file. For each case, the pseudo-inverse method is applied to find the wavenumber inside the cylinder array. Then, the relation $n_e = \frac{k_e}{k}$ is used to determine the refractive indexes. In Figure 2.5, the theoretical value of n_e is determined from the relation $n_e = \sqrt{1 + f_s}$ in Hu and Chan's (2005) theory. According to the result from WAMIT, the refractive indexes match the theoretical curve of n_e. Thus, the refractive index is validated. For the cases where filling ratio are 0.1452 and 0.0929, the refractive indexes determined from WAMIT's result are slightly smaller than the theoretical value, while in the cases of 0.5809 and 0.4034 filling ratios the WAMIT's results are larger than the values on the curve.

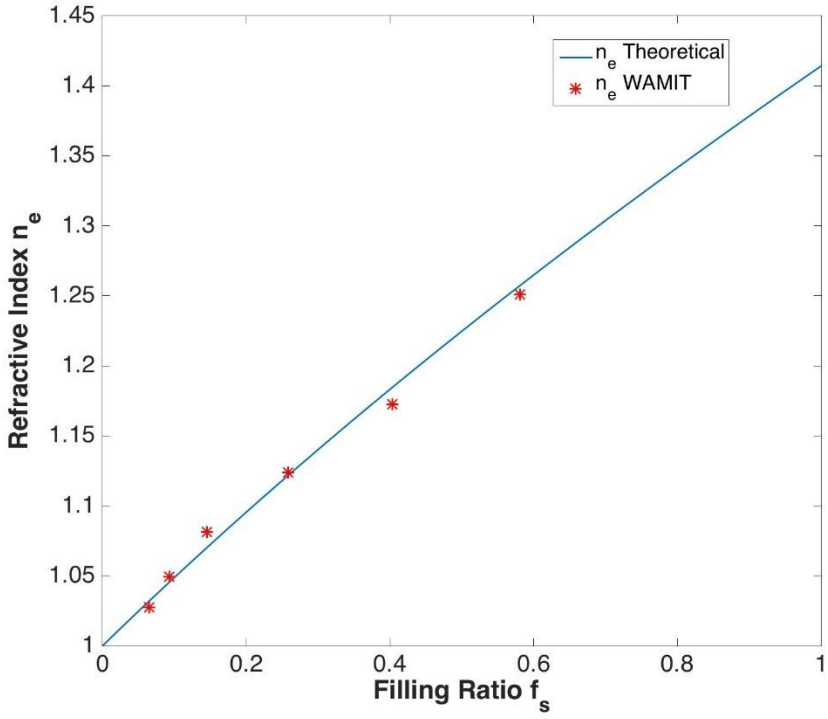

Figure 2.5. Refractive index ne as a function of the filling ratio fs of the arrays

2.7. Transmittance and Reflectance of Arrays of Uniformly Spaced Rigid Cylinders

Once the theoretical definition of the refractive index is verified, the next step is to determine the reflection and transmission coefficients for the arrays using WAMIT's numerical output. The pseudo-inverse method has been used in this study, and the theory associated with the Fabry-Pérot Interferometer is applied in order to find the intensities of reflection and transmission of the arrays. The incident wave period is 20s. Nine different arrays of rigid cylinders are studied. For each of those cases, a line of field points close to the x-axis are chosen to calculate the coefficients. The position of the line is shown in Figure 2.6. Equations (2.33) and (2.35) is used to calculate amplitude reflection coefficient and the amplitude transmission coefficient, while θ and φ are set to be zero since we are only considering an incident wave of zero degree.

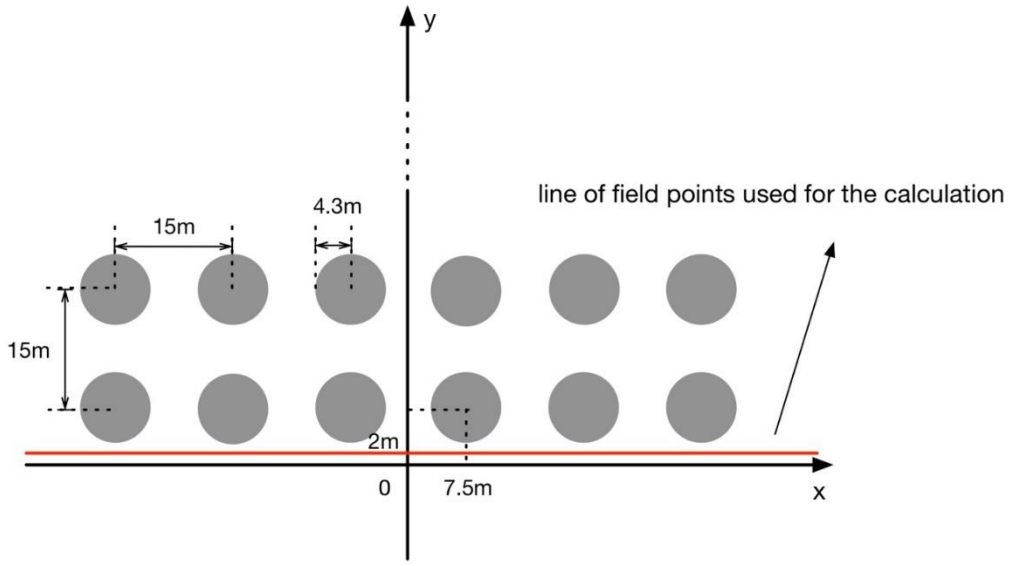

Figure 2.6. Position of the line of field points chosen to calculate the reflection and transmission coefficients.

With the coefficients calculated, one can determine the transmittance and reflectance of the arrays. Figure 2.7 shows a good agreement between the results from WAMIT and the coefficients predicted by Hu and Chan's (2005) theory. Therefore, the WAMIT setup and the pseudo-inverse method are proved to be successful. For any given array of cylinders, the reflection and transmission coefficients of the array can be determined by using pseudo-inverse method to process WAMIT's surface elevation output.

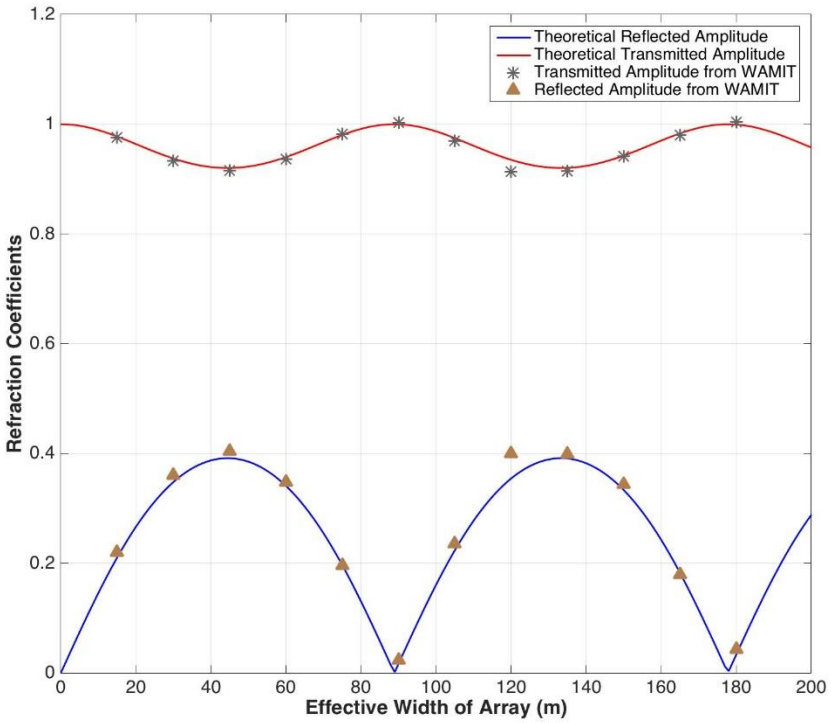

Figure 2.7. Transmittance and reflectance of waves as a function of the effective width of the arrays.

Note that these coefficients are identified from the data on a line of field points that are very close to the x-axis (i.e. the plane of symmetry), which indicates the so-called "tip effect" is not affecting the values of the coefficients determined by the pseudo-inverse

method. If we use field points that are close to the tip to calculate the parameters, the results will not be the same. Table 2.1 shows the reflection and transmission coefficients of the 7 by 126 array identified using field points that are affected by the "tip effect". We can see that the coefficients determined from those field points are different. The first row of data in this table is generated from the "least affected" field points and is used for the comparison with WAMIT's results in Figure 2.7. As the distance from x-axis increases, the "tip effect" exerted on the surface elevations of the field points becomes stronger. For some lines of field points, the transmission coefficients are even greater than 1, which indicates the "tip effect" causes the wave amplitude on the transmitted wave side to be larger than the incident wave. This is one of the reasons why the "tip effect" needs to be considered in the study of wave interactions with large cylinder arrays. Details about the effect will be discussed in the next subsection.

Table 2.1 Reflection and transmission coefficients of the 7 by 126 array calculated from surface elevations on six straight lines of field points parallel to the x-axis.

Distance from x-axis	Reflection coefficient	Transmission coefficient
2m	0.2357	0.9697
378.5m	0.2617	1.0062
755m	0.2615	0.9190
1131.5m	0.2942	1.0380
1508m	0.2217	1.0596
1884.5m	0.2681	0.9619

2.8. Tip Effect of Arrays of Uniformly Spaced Rigid Cylinders

The cases completed for this subsection are five different arrays of uniformly spaced rigid cylinders which are shown in Table 2.2. While the total number of cylinders of those cases is roughly the same (880, 882, 882, 882 and 880, respectively), the arrangements of the cylinders are different in order to analyze the relationship between the so-called "tip effect" and the length of array. The spacing between adjacent cylinders in all five cases is 15m.

Table 2.2 Arrangements of the rigid cylinder arrays

	Columns	Rows	Total	Length
Case A	5	176	880	2632.5m
Case B	6	147	882	2197.5m
Case C	7	126	882	1882.5m
Case D	9	98	882	1462.5m
Case E	11	80	880	1192.5m

The input parameters of WAMIT for the arrays are listed in Table 2.3. In this subsection the wave condition stays the same for all those five cases. Only zero incident wave angle is considered in the study. For each array, a set of wave field points with proper length and width is chosen in order to include the tip effect. The distances between adjacent points in both X-direction and Y-direction are set to be 10m.

Table 2.3 Input parameters for WAMIT in the cases of rigid cylinder arrays.

Parameter	Value
Water depth, $\boldsymbol{h}$	10.5m
Wave period, $\boldsymbol{T}$	20s
Wavenumber of incident wave, $\boldsymbol{k}$	$0.0315 m^{-1}$
Incident wave angle, $\boldsymbol{\theta}$	0
Incident wave amplitude, $\boldsymbol{A}$	1
Radius of cylinder, $\boldsymbol{R}$	4.3m
Draft of cylinder, $\boldsymbol{d}$	10.5m
Spacing between cylinders, $\boldsymbol{a}$	15m
Distance between field points, $\boldsymbol{p}$	10m
Filling ratio, $\boldsymbol{fs}$	0.2582
Gravitational acceleration, $\boldsymbol{g}$	$9.81 m/s^2$

Surface elevations associated with the five different arrays of rigid cylinders were generated by WAMIT. Linear interpolation was applied and the resolution was increased by four times, which leads to smoother images. The results are plotted from Figure 2.8 to Figure 2.12. One can observe that at the top end of each array, the wave field is more interfered than that at the bottom of the image. If we consider the x-axis as a mirror and add a mirror image of the wave field at the opposite side of the x-axis, we can find that when the incident wave encounters an array of long rigid cylinders, it is more diffracted at the far ends than at the central part of the array.

Moreover, the intensity of this so-called “tip effect” is affected by the effective length of the array, and hence the arrangement of the rigid cylinders. As the length of the array

increases, the intensity of the tip effect becomes weaker, and the “shadow” zone that is not affected by the tip effect becomes larger. On one hand, for the case of 5 by 176 array, when the length of the array reaches 2632.5m, the wave field near the top end of the array appears to be almost the same as the incident wave coming from the left. This could have been anticipated as the total length of this cylinder array is the largest among all the cases, which causes the weakest tip effect under the same wave condition. On the other hand, in Figure 2.12, the tip effect for the case of 11 by 80 array is much easier to observe, as we can see an obvious distortion of the wave crests and troughs near the tip.

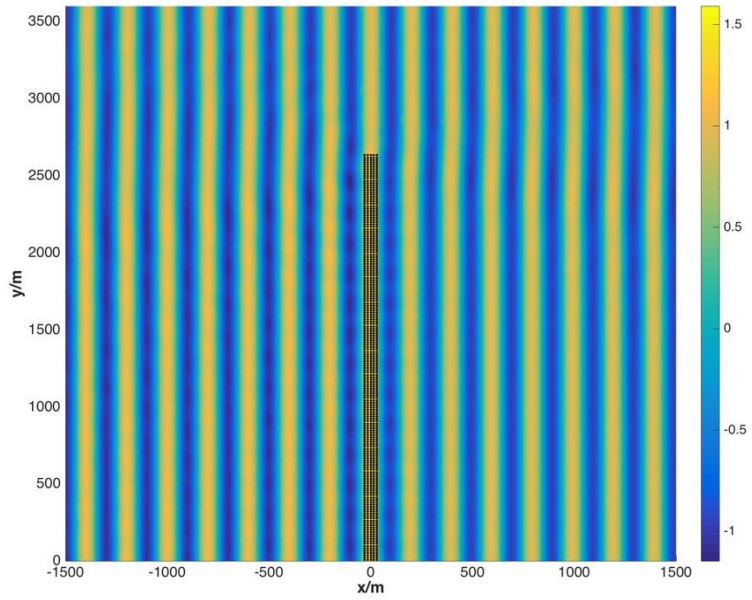

Figure 2.8. Wave surface elevation for the 5 by 176 array with an incident wave period T=20s.

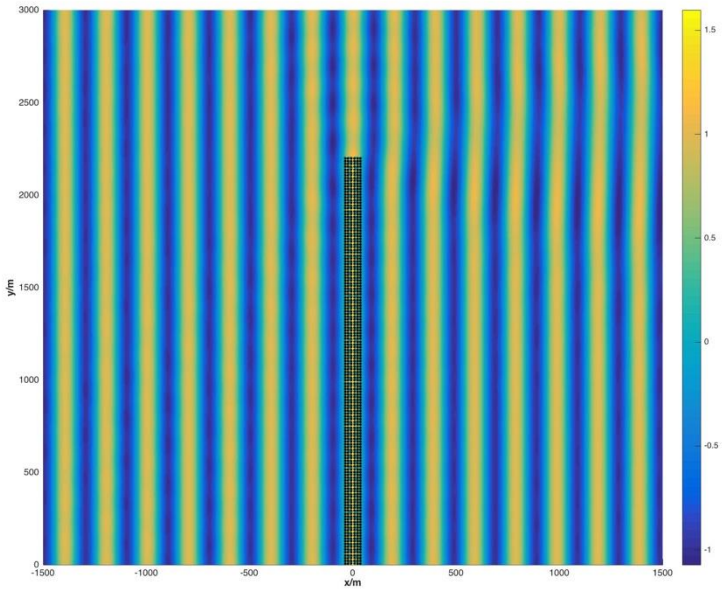

Figure 2.9. Wave surface elevation for the 6 by 147 array with an incident wave period T=20s.

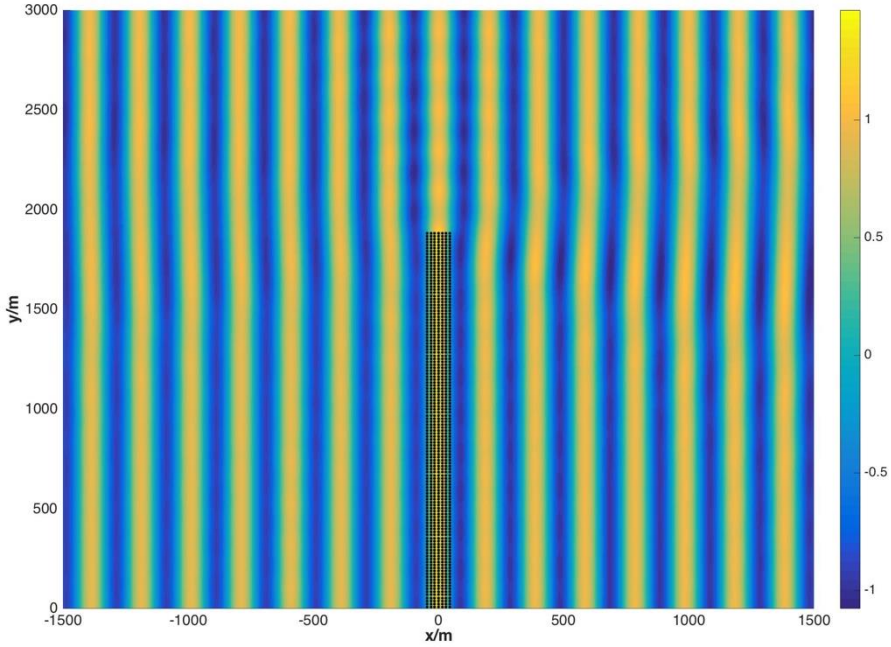

Figure 2.10. Wave surface elevation for the 7 by 126 array with an incident wave period T=20s.

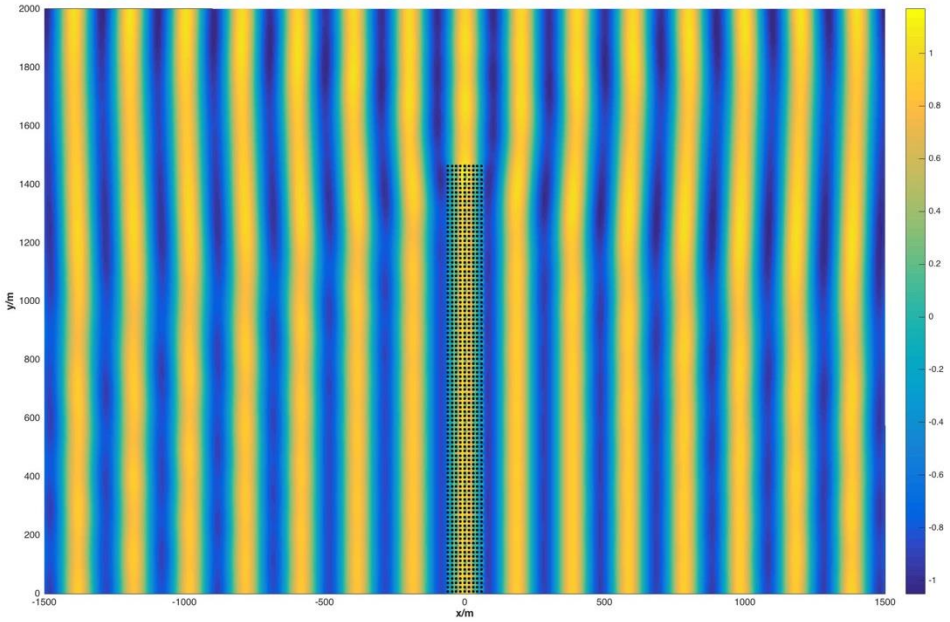

Figure 2.11. Wave surface elevation for the 9 by 98 array with an incident wave period T=20s.

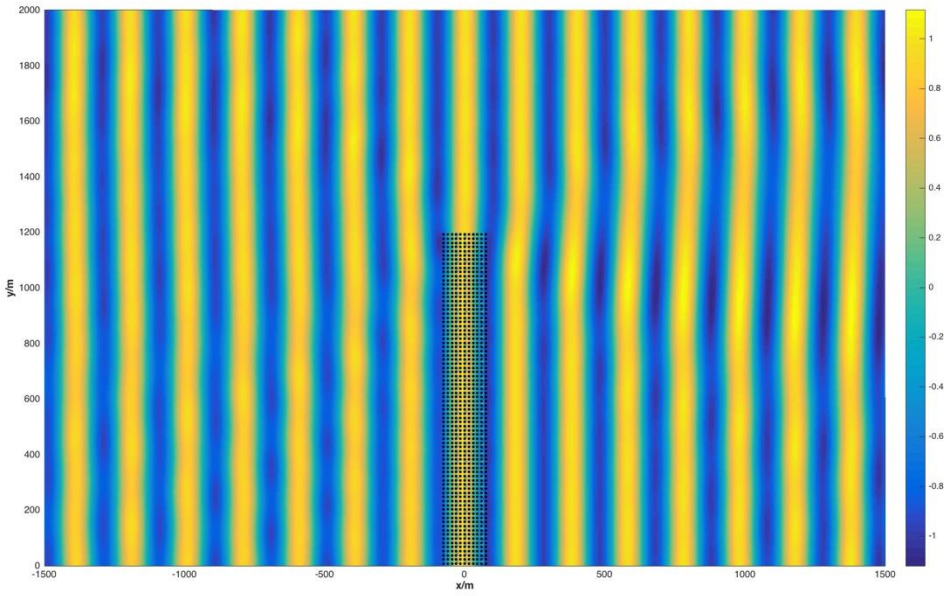

Figure 2.12. Wave surface elevation for the 11 by 80 array with an incident wave period T=20s.

2.9. Anomaly Detection of Uniformly Spaced Rigid Cylinder Arrays

To further study the intensity of the "tip effect", and to better reveal the effects at the ends, anomaly analysis is conducted for the five cases studied in Subsection 2.8. The plots are created by subtracting the incident wave from WAMIT's output of the refracted wave field. The results are presented from Figure 2.13 to Figure 2.17. As we can see in the plots, the variation of surface elevation on the incident wave side is much stronger than the transmitted wave side. In Figure 2.13, it can also be seen that some nodes exist on both the incident wave side and the transmitted wave side of the plots due to the interference of incident and reflected waves.

The effect is easy to identify at the top ends of the arrays. If we look at the transmitted wave side, we can see that the variation of wave surface elevation at the tips is stronger than that in the "shadow" area near the x-axis. Moreover, this difference of wave amplitude varies as the array length changes. In Figure 2.13, as the wave passes the longest cylinder array, similar variations of surface elevation can be seen in both the wave field close to the plane of symmetry and the area at the tips. However, this is not the case for the shortest array in Figure 2.17, where the change of wave amplitude at the top end is much greater than that in the area close to the plane of symmetry. This result supports the previous conclusion that as the length of the array increases, a weaker tip effect can be observed.

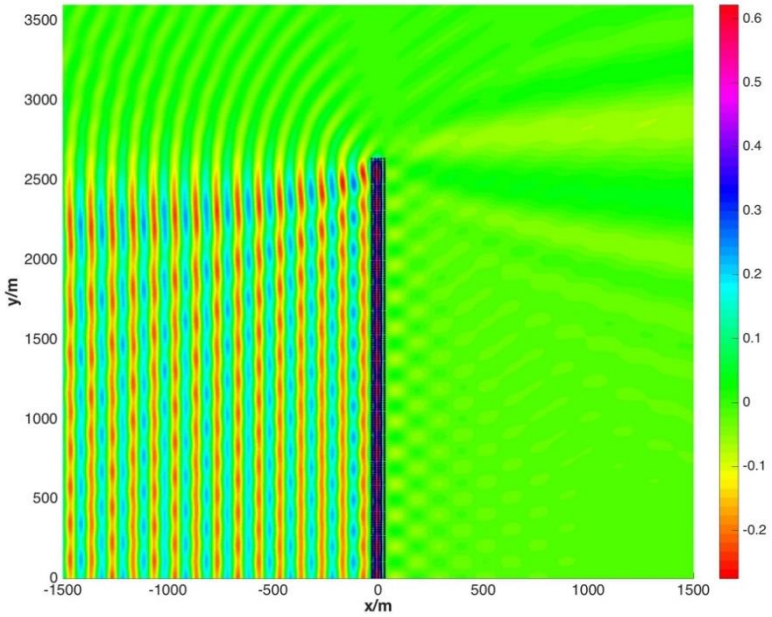

Figure 2.13. Anomaly for the 5 by 176 array with an incident wave period T=20s.

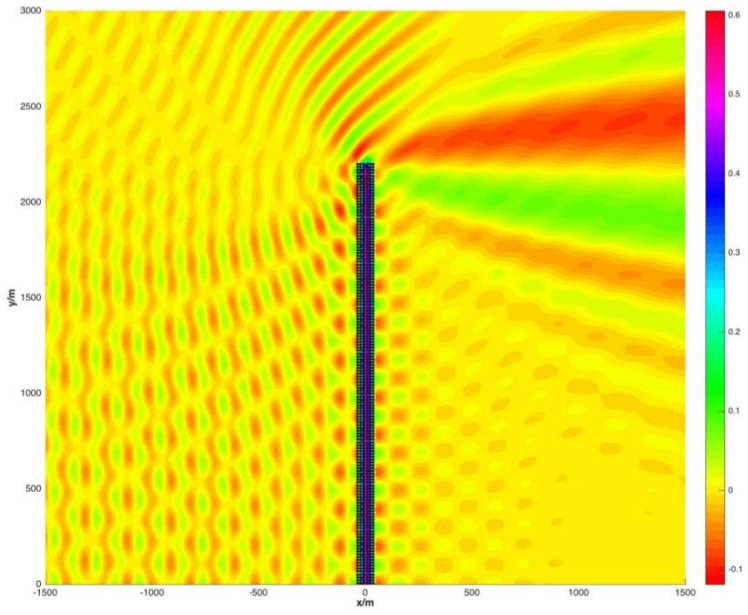

Figure 2.14. Anomaly for the 6 by 147 array with an incident wave period T=20s.

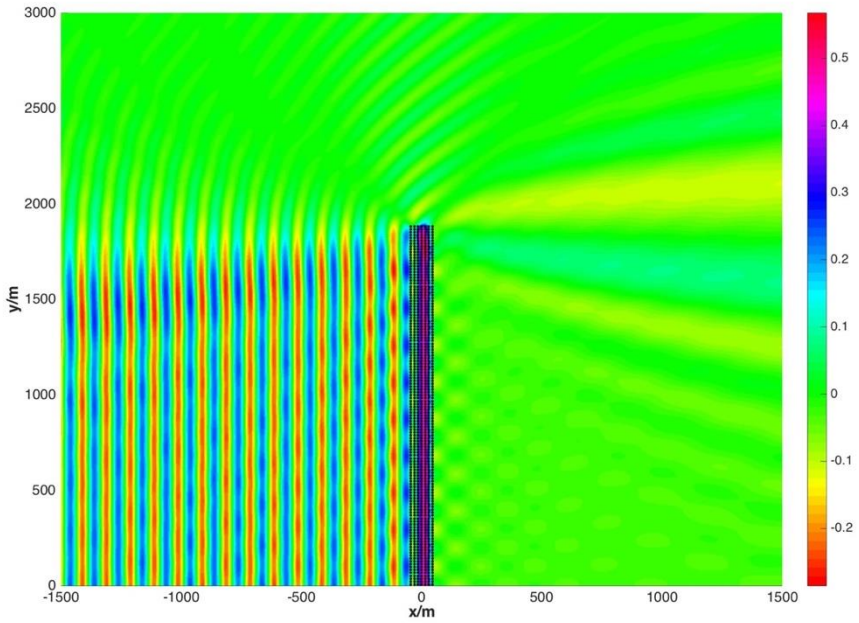

Figure 2.15. Anomaly for the 7 by 126 array with an incident wave period T=20s.

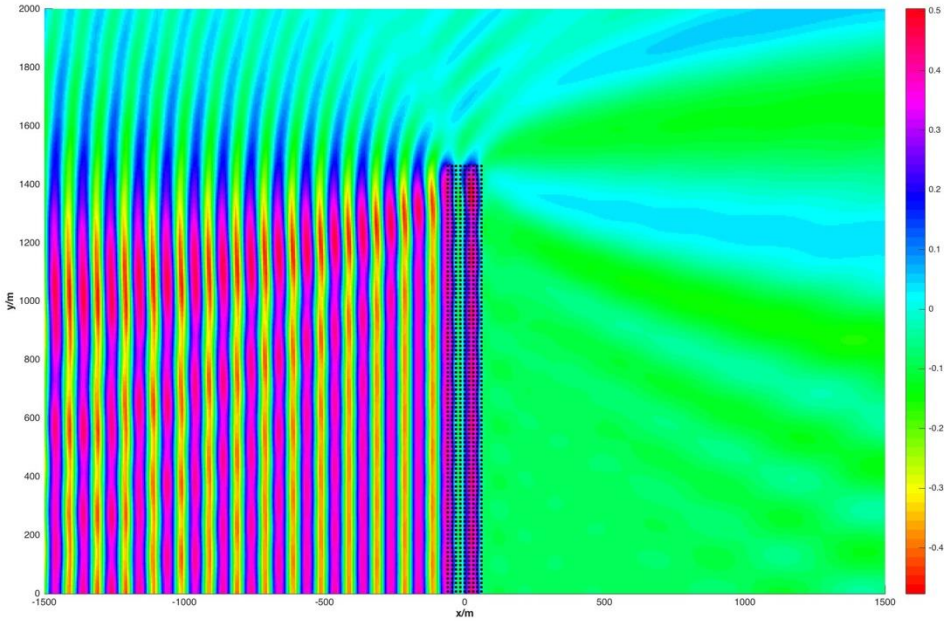

Figure 2.16. Anomaly for the 9 by 98 array with an incident wave period T=20s.

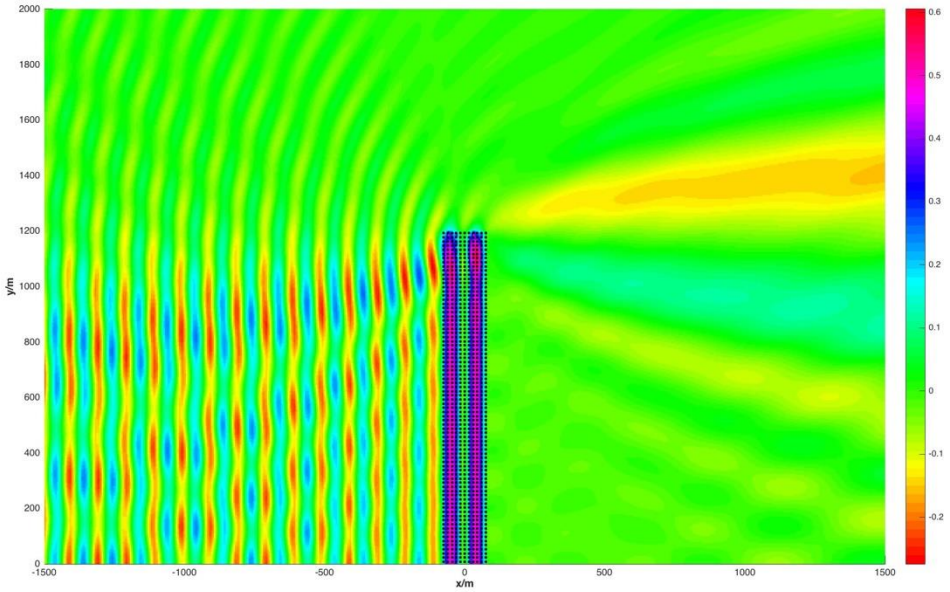

Figure 2.17. Anomaly for the 11 by 80 array with an incident wave period T=20s.

In addition, the case of 11 by 80 cylinders is run for four different incident wave periods (20s, 16s, 12s, 8s). Comparing Figures 2.17-2.23 we can see that when the same array of cylinders is exposed to shorter incident waves, the tip effect tends to be weaker and the “shadow” zone that is not affect by the effect becomes larger.

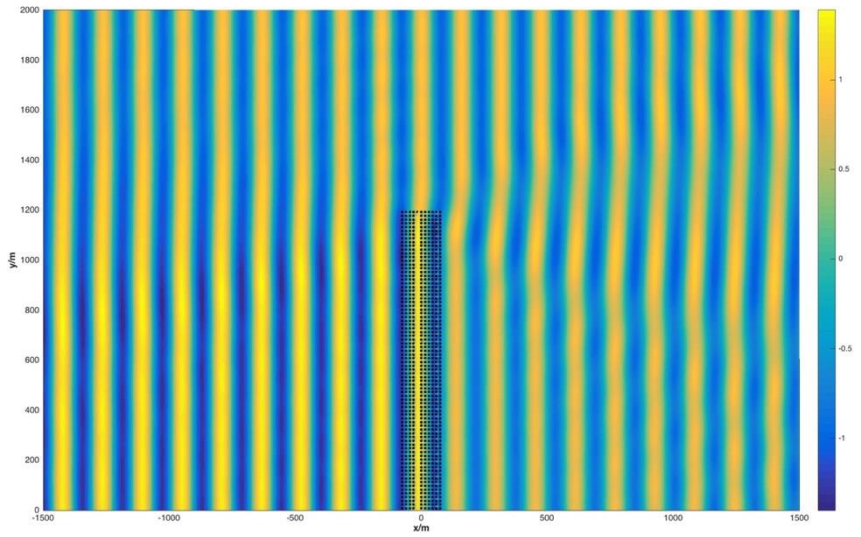

Figure 2.18. Surface elevation for the 11 by 80 array with an incident wave period T=16s.

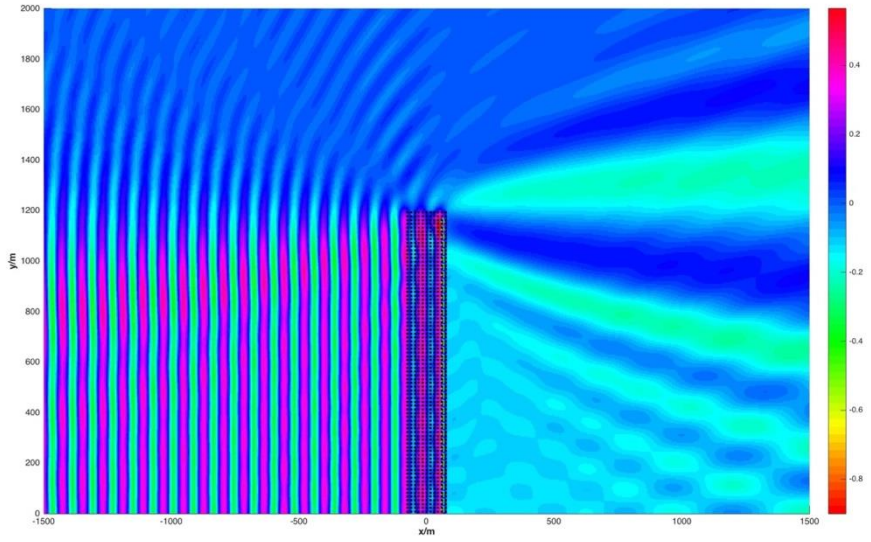

Figure 2.19. Anomaly for the 11 by 80 array with an incident wave period T=16s.

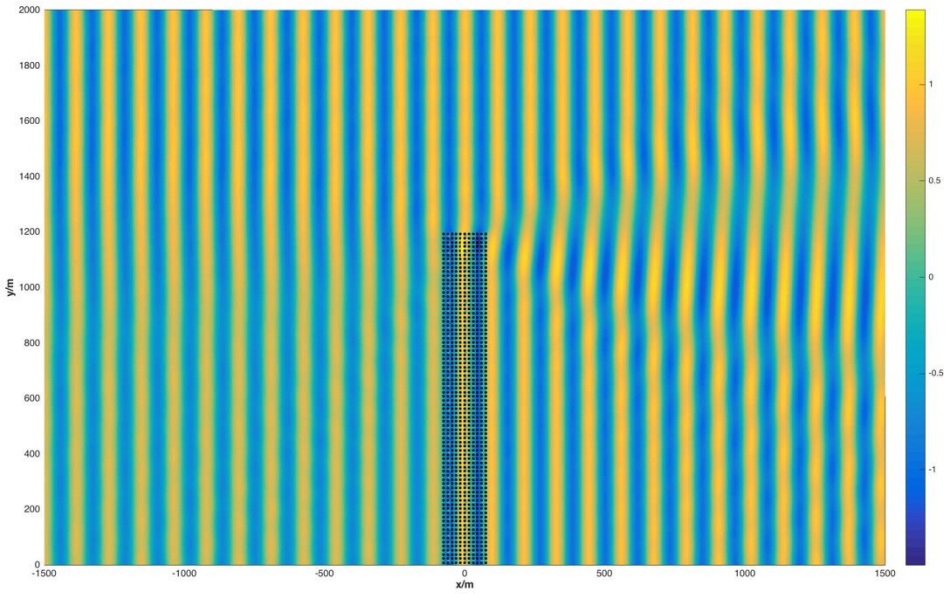

Figure 2.20. Surface elevation for the 11 by 80 array with an incident wave period T=12s.

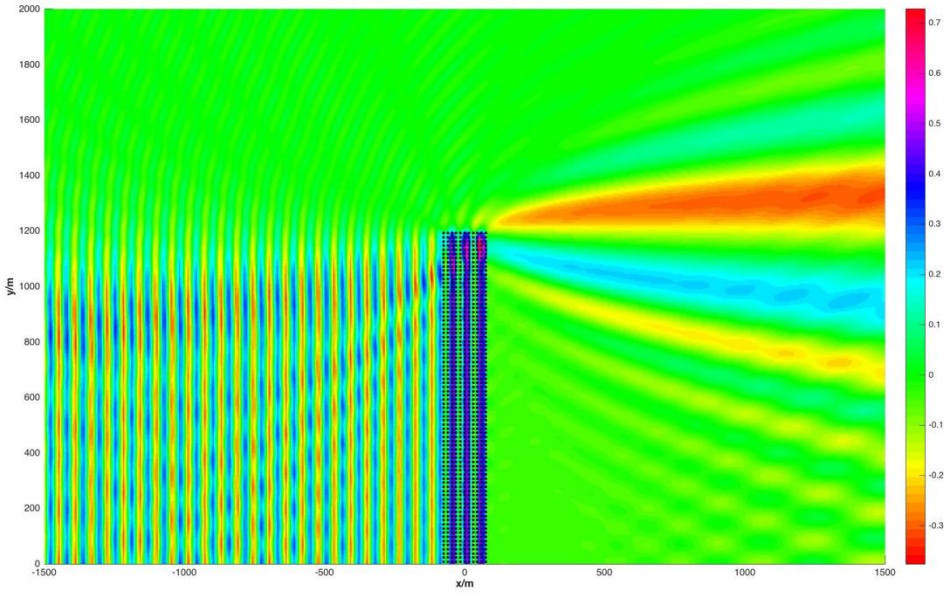

Figure 2.21. Anomaly for the 11 by 80 array with an incident wave period T=12s.

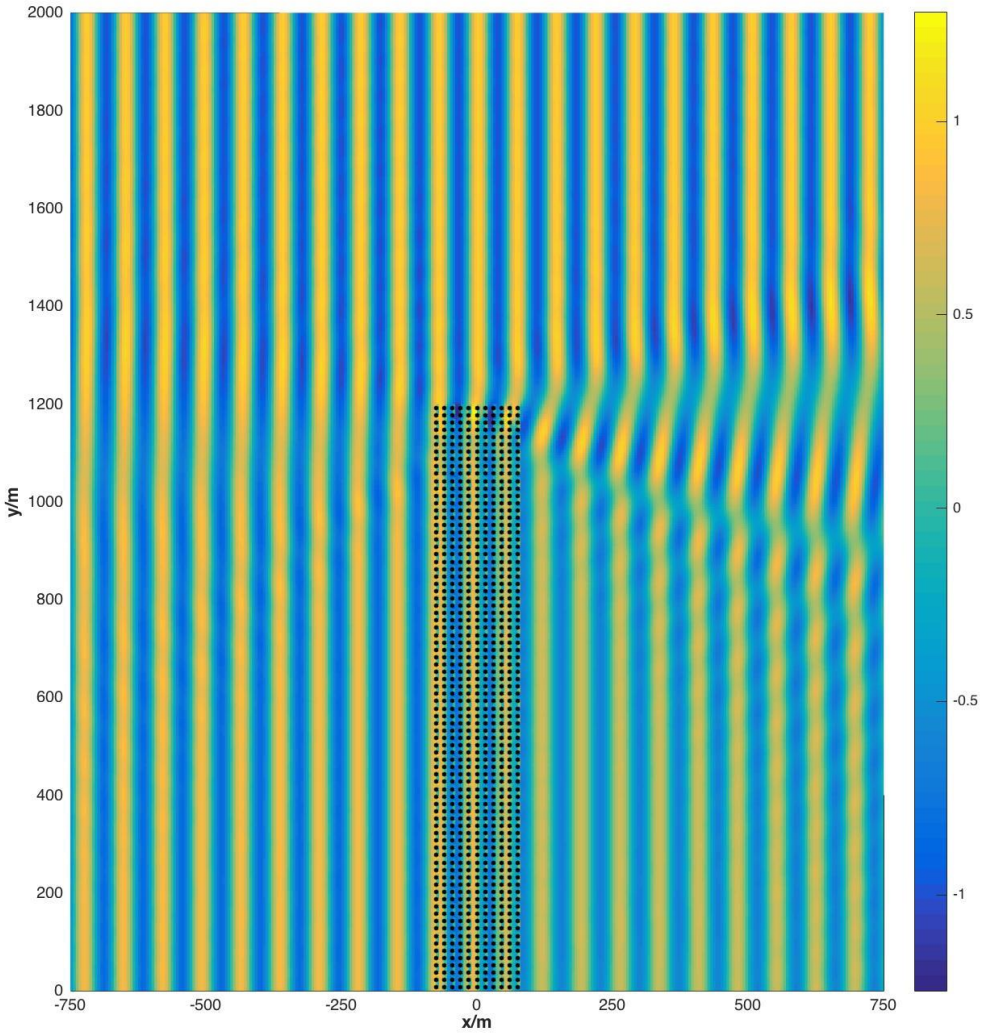

Figure 2.22. Surface elevation for the 11 by 80 array with an incident wave period T=8s.

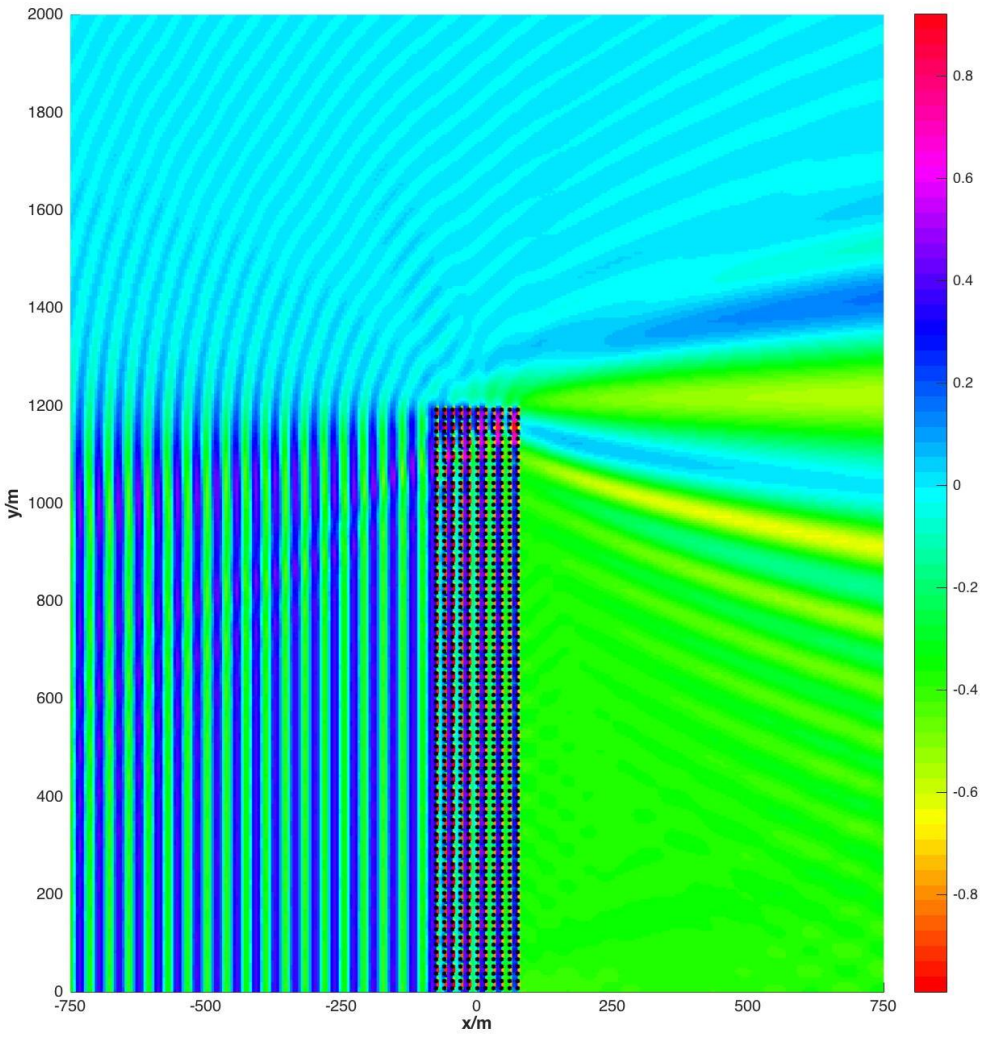

Figure 2.23. Anomaly for the 11 by 80 array with an incident wave period T=8s.

In addition, for the case C which corresponds to a 7 by 126 cylinder array, wave surface elevations on six straight lines that are parallel to the x-axis are selected from the wave domain and plotted in Figure 2.24 in order to further analyze the “tip effect”. The wave condition is the same as in Table 2.3. The y-axis coordinates (distance from the x-

axis) of the six lines are provided in Table 2.4. It can be easily seen that on the incident wave side, the wave amplitude is much larger than that on the transmitted wave side.

Moreover, the transmitted wave can be clearly identified in the plot for line A as this line is close to the plane of symmetry. However, the wave surface elevations on the transmitted wave side in lines B, C, D, E and F are strongly affected by the "tip effect", which causes the wave patterns to be erratic. Therefore, it is not possible to identify the transmitted wave component using the surface elevation data on those five lines. Note that the erratic transmitted wave pattern occurs starting from line B, which indicates for a cylinder array of 1882.5m in length, the "tip effect" starts to disturb the transmitted wave at least from the position where the distance from the plane of symmetry is 378.5m.

Table 2.4 Distances between six parallel lines and the x-axis.

	Line A	Line B	Line C	Line D	Line E	Line F
Distance	2m	378.5m	755m	1131.5m	1508m	1884.5m

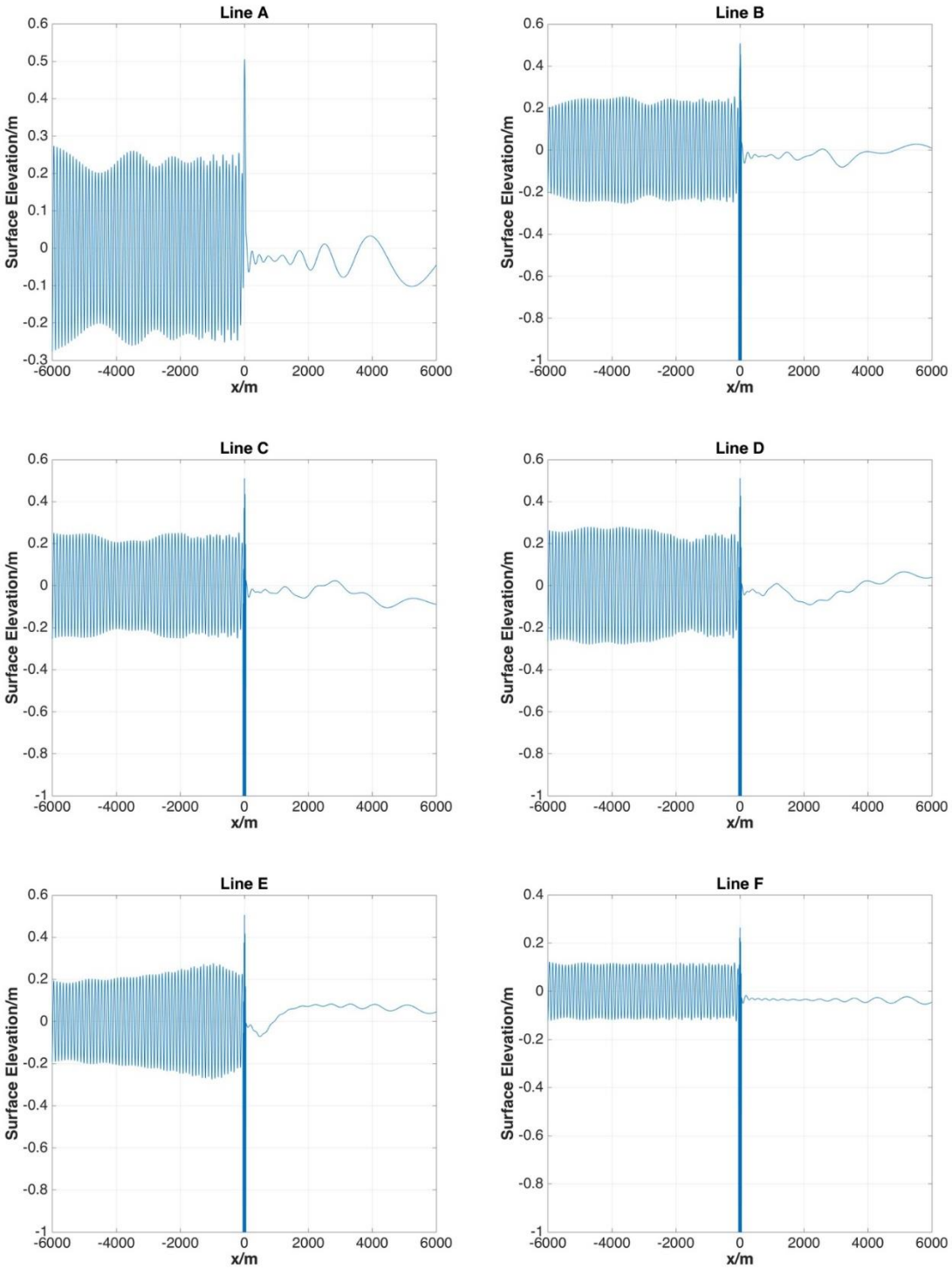

Figure 2.24. Wave surface elevation on six straight lines that are parallel to x-axis.

3. HYDRO-ELASTIC ANALYSIS OF CYLINDER ARRAYS

Starting from this section, bottom-mounted deformable vertical cylinders that are pulsating in the water will be studied in stead of rigid cylinders as in the previous sections. Deformable cylinders are treated as thin shells clamped at both top and bottom. The modal superposition approach is applied to enable calculation of the hydro-elastic response of one single elastic cylinder exposed to incident waves of length much larger than the cylinder radius. WAMIT is used in the hydro-elastic analysis of the elastic cylinder, employing its generalized modes and higher order boundary element capabilities.

The equations of motion for a single deformable cylinder are derived from the theory of vibration for thin shells, and added mass, radiation damping and stiffness matrices are defined. Those analytical expressions are in matrix form consistent with the generalized modes formulation within WAMIT. Then a design exercise is performed to select realistic material properties and cylinder dimensions so that the breathing mode natural frequency is within the range of wave frequencies. WAMIT's Fortran subroutine for generalized modes is then modified to incorporate the generalized body modes for the pulsating cylinder. To verify the implementation of the Fortran subroutines, WAMIT's numerical results for a single pulsating cylinder are compared with the exact analytical solution.

3.1. Theoretical Background

3.1.1. Equations of motion for a cylindrical shell

The system considered is a closed vertical circular cylindrical shell of radius R and length L with shear diaphragms (cover plates) at the top and bottom. Radial displacements are impossible at the top and bottom. A thin shell is a body bounded by two curved surfaces. The thickness h of the shell is much smaller than the radius or length of the

cylinder. The cylinder is bottom mounted in water of depth L and exposed to incident monochromatic gravity waves.

The following assumptions were made by Love (1892) in the classic theory of small displacements of thin shells. These assumptions are universally accepted in thin shell theories, including Donnell and Mushtari's theory which will be used in this study.

- The thickness of the shell is small compared to the other dimensions of the shell (radius and length).
- strains and displacements are sufficiently small to neglect second order effects in the strain displacement relations;
- the transverse normal stress is small compared with the other normal stress components and may be neglected;
- normals to the un-deformed middle surface remain straight and normal to the deformed middle surface and suffer no extension.

Figure 3.1 represents the single deformable cylinder considered in this section. A body-fixed (X, Y, Z) Cartesian coordinate system has its origin at the center of the top surface of the cylinder, with Z vertically upward. The radius R corresponds to the middle surface of the shell and the deformations of the shell membrane are measured by tracking the local displacements of the middle surface. With θ as the azimuthal coordinate and t as time, the local displacements $U(z, \theta, t)$, $V(z, \theta, t)$, and $W(z, \theta, t)$ are in the vertical, circumferential and radial directions, respectively.

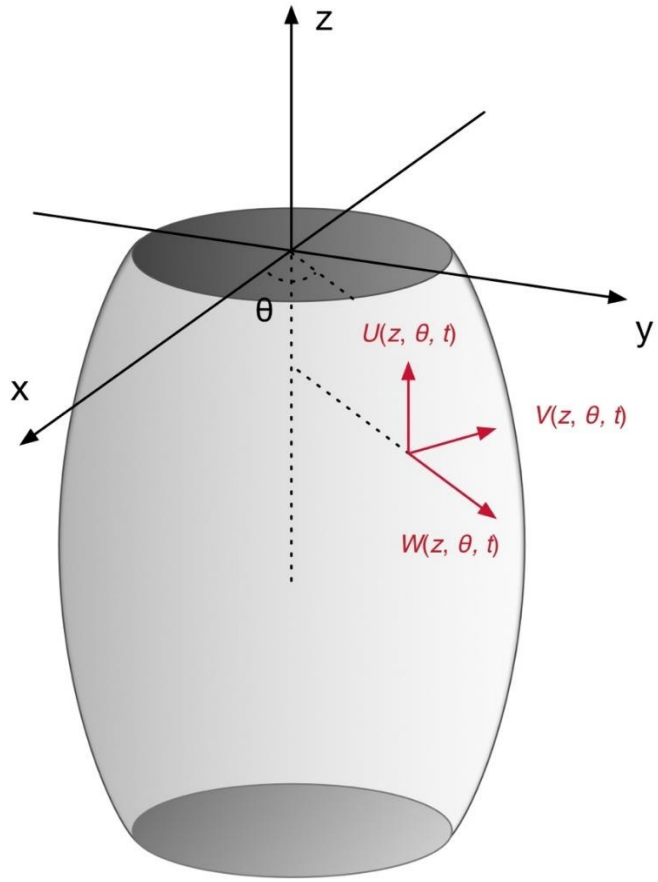

Figure 3.1. Displacements in the vertical, circumferential and radial directions.

Donnell-Mushtari's theory for vibration of thin cylindrical shells is applied in the hydro-elastic analysis of deformable cylinders, which is documented in the NASA report by Leissa (1973). According to this theory, the equations of motion for forced vibrations of the shell may be expressed as:

$$\rho_s h\frac{\partial^2 U}{\partial t^2} - \frac{Eh}{(1-\nu^2)}\frac{\partial^2 U}{\partial z^2} - \frac{Eh(1-\nu)}{2R^2(1-\nu^2)}\frac{\partial^2 U}{\partial \theta^2} - \frac{Eh(1+\nu)}{2R(1-\nu^2)}\frac{\partial^2 V}{\partial z \partial \theta} - \frac{Eh\nu}{R(1-\nu^2)}\frac{\partial W}{\partial z} = f_z \tag{3.1}$$

$$-\frac{Eh(1+\nu)}{2R(1-\nu^2)}\frac{\partial^2 U}{\partial z\partial\theta}+\rho_s h\frac{\partial^2 V}{\partial t^2}-\frac{Eh(1-\nu)}{2(1-\nu^2)}\frac{\partial^2 V}{\partial z^2}$$
$$-\frac{Eh}{R^2(1-\nu^2)}\frac{\partial^2 V}{\partial\theta^2}-\frac{Eh}{R^2(1-\nu^2)}\frac{\partial W}{\partial\theta}=f_\theta \tag{3.2}$$

$$\frac{Eh\nu}{R(1-\nu^2)}\frac{\partial U}{\partial z}+\frac{Eh}{R^2(1-\nu^2)}\frac{\partial V}{\partial\theta}+\rho_s h\frac{\partial^2 W}{\partial t^2}$$
$$+\frac{Eh^3}{12(1-\nu^2)}\frac{\partial^4 W}{\partial z^4}+\frac{Eh^3}{6R^2(1-\nu^2)}\frac{\partial^4 W}{\partial z^2\partial\theta^2}$$
$$+\frac{Eh^3}{12R^4(1-\nu^2)}\frac{\partial^4 W}{\partial\theta^4}+\frac{Eh}{R^2(1-\nu^2)}W \tag{3.3}$$
$$=f_r$$

where ν is Poisson's coefficient, E is Young's modulus, ρ_s is the mass density of the shell material, f_r is the distributed normal force (external pressure), and f_z and f_θ are the distributed shear forces in the vertical and azimuthal directions, respectively.

The equations of motion may be written in matrix form as

$$[\mathcal{L}]\{u\}=\{f\} \tag{3.1}$$

with

$$\{u\}=\begin{bmatrix}U\\V\\W\end{bmatrix} \tag{3.2}$$

$$[\mathcal{L}]=\begin{bmatrix}\mathcal{L}_{11}&\mathcal{L}_{12}&\mathcal{L}_{13}\\\mathcal{L}_{21}&\mathcal{L}_{22}&\mathcal{L}_{23}\\\mathcal{L}_{31}&\mathcal{L}_{32}&\mathcal{L}_{33}\end{bmatrix} \tag{3.3}$$

$$\{f\}=\begin{bmatrix}f_z\\f_\theta\\f_r\end{bmatrix} \tag{3.4}$$

where $\{u\}$ is the displacement vector and *U*, *V*, and *W* are the body displacements in the vertical, tangential, and radial directions, respectively. The elements of $[\mathcal{L}]$ are:

$$\mathcal{L}_{11}=\rho_s h\frac{\partial^2}{\partial t^2}-\frac{Eh}{(1-\nu^2)}\frac{\partial^2}{\partial z^2}-\frac{Eh(1-\nu)}{2R^2(1-\nu^2)}\frac{\partial^2}{\partial\theta^2} \tag{3.5}$$

$$\mathcal{L}_{12} = \mathcal{L}_{21} = -\frac{Eh(1+\nu)}{2R(1-\nu^2)}\frac{\partial^2}{\partial z \partial \theta} \tag{3.6}$$

$$\mathcal{L}_{13} = -\mathcal{L}_{31} = -\frac{Eh\nu}{R(1-\nu^2)}\frac{\partial}{\partial z} \tag{3.7}$$

$$\mathcal{L}_{22} = \rho_s h\frac{\partial^2}{\partial t^2} - \frac{Eh(1-\nu)}{2(1-\nu^2)}\frac{\partial^2}{\partial z^2} - \frac{Eh}{R^2(1-\nu^2)}\frac{\partial^2}{\partial \theta^2} \tag{3.8}$$

$$\mathcal{L}_{23} = -\mathcal{L}_{32} = -\frac{Eh}{R^2(1-\nu^2)}\frac{\partial}{\partial \theta} \tag{3.9}$$

$$\mathcal{L}_{33} = \rho_s h\frac{\partial^2}{\partial t^2} + \frac{Eh\mu}{R^2(1-\nu^2)}\nabla^4 + \frac{Eh}{R^2(1-\nu^2)} \tag{3.10}$$

with $\mu = \frac{h^2}{12R^2} \ll 1$ and

$$\nabla^4 = \nabla^2\nabla^2 = \left[R^2\frac{\partial^2}{\partial z^2} + \frac{\partial^2}{\partial \theta^2}\right]^2 \tag{3.11}$$

3.1.2. Boundary conditions

Because there are no radial or circumferential displacements at the top and bottom of the cylinder, the following boundary conditions have to be satisfied:

$$V(0,\theta,t) = V(\mathrm{L},\theta,t) = W(0,\theta,t) = W(\mathrm{L},\theta,t) = 0 \tag{3.12}$$

$$\frac{\partial U(0,\theta,t)}{\partial z} + \frac{\nu}{R}\frac{\partial V(0,\theta,t)}{\partial \theta} + \frac{\nu}{R}\,W(0,\theta,t) = 0 \tag{3.13}$$

$$\frac{\partial U(L,\theta,t)}{\partial z} + \frac{\nu}{R}\frac{\partial V(L,\theta,t)}{\partial \theta} + \frac{\nu}{R}\,W(L,\theta,t) = 0 \tag{3.14}$$

$$\frac{\nu}{R^2}\frac{\partial V(0,\theta,t)}{\partial \theta} - \frac{\partial^2 W(0,\theta,t)}{\partial z^2} - \frac{\nu}{R^2}\frac{\partial^2 W(0,\theta,t)}{\partial \theta^2} = 0 \tag{3.15}$$

$$\frac{\nu}{R^2}\frac{\partial V(L,\theta,t)}{\partial \theta} - \frac{\partial^2 W(L,\theta,t)}{\partial z^2} - \frac{\nu}{R^2}\frac{\partial^2 W(L,\theta,t)}{\partial \theta^2} = 0 \tag{3.16}$$

at *z=0* and *z=L*.

3.1.3. Modal decomposition

A modal decomposition approach is applied in this subsection. If the external forcing is harmonic or the cylinder is undergoing free vibrations, the total displacements in the vertical, tangential and radial directions may be expanded in double Fourier series according to:

$$U(z,\theta,t) = \sum_{m=1}^{\infty}\sum_{n=0}^{\infty} \alpha_{mn} \cos(m\pi z/L)\cos(n\theta)\, e^{i\omega t} \tag{3.17}$$

$$V(z,\theta,\mathrm{t}) = \sum_{m=1}^{\infty}\sum_{n=0}^{\infty} \beta_{mn} \sin(m\pi z/L)\sin(n\theta)\, e^{i\omega t} \tag{3.18}$$

$$W(z,\theta,t) = \sum_{m=1}^{\infty}\sum_{n=0}^{\infty} \gamma_{mn} \sin(m\pi z/L)\cos(n\theta)\, e^{i\omega t} \tag{3.19}$$

where α_{mn}, β_{mn} and γ_{mn} are the corresponding amplitudes of the displacements. The displacement mode corresponding to n=0 and m=1 is called the "breathing" mode and its natural frequency will receive particular attention, especially in choosing the material properties of the cylindrical shell. The modal amplitudes associated with each (m, n) mode of vibration can be written as

$$\{\xi_{mn}\} = \begin{bmatrix}\xi_{1mn}\\ \xi_{2mn}\\ \xi_{3mn}\end{bmatrix} = \begin{bmatrix}\alpha_{mn}\\ \beta_{mn}\\ \gamma_{mn}\end{bmatrix} \tag{3.20}$$

and orthogonal shape functions as

$$\{W_{mn}(z,\theta)\} = \begin{bmatrix}W_{1mn}\\ W_{2mn}\\ W_{3mn}\end{bmatrix} = \begin{bmatrix}\cos(m\pi z/L)\cos(n\theta)\\ \sin(m\pi z/L)\sin(n\theta)\\ \sin(m\pi z/L)\cos(n\theta)\end{bmatrix} \tag{3.21}$$

such that the modal displacements can be expressed as

$$\{u_{mn}\} = \begin{bmatrix} \xi_{1mn} W_{1mn} \\ \xi_{2mn} W_{2mn} \\ \xi_{3mn} W_{3mn} \end{bmatrix} \tag{3.22}$$

3.1.4. Mass and stiffness matrices

The mass and stiffness matrices for the cylindrical shell can be defined following Newman's (1994) procedure. A separate system of equations can be written for each (*m*, *n*) mode of vibration according to:

$$[\mathcal{L}]\{u_{mn}\} = [\mathcal{L}] \begin{bmatrix} \alpha_{mn} \cos(\lambda z) \cos(n\theta) \\ \beta_{mn} \sin(\lambda z) \sin(n\theta) \\ \gamma_{mn} \sin(\lambda z) \cos(n\theta) \end{bmatrix} = \{f_{mn}\} \tag{3.23}$$

with $\{f_{mn}\}$ as the modal forcing. If the cylinder is undergoing un-damped free vibrations, then $\{f_{mn}\} = 0$. Therefore, we can write

$$[\mathcal{L}]\{u_{mn}\} = [\mathcal{L}] \begin{bmatrix} \alpha_{mn} \cos(\lambda z) \cos(n\theta) \\ \beta_{mn} \sin(\lambda z) \sin(n\theta) \\ \gamma_{mn} \sin(\lambda z) \cos(n\theta) \end{bmatrix} = [\mathcal{L}'] \begin{bmatrix} \alpha_{mn} \\ \beta_{mn} \\ \gamma_{mn} \end{bmatrix} = 0 \tag{3.24}$$

With

$$[\mathcal{L}'] = \begin{bmatrix} \mathcal{L}'_{11} & \mathcal{L}'_{12} & \mathcal{L}'_{13} \\ \mathcal{L}'_{21} & \mathcal{L}'_{22} & \mathcal{L}'_{23} \\ \mathcal{L}'_{31} & \mathcal{L}'_{32} & \mathcal{L}'_{33} \end{bmatrix} \tag{3.25}$$

where

$$\mathcal{L}'_{11} = -\rho_s h\omega^2 + \frac{Eh}{R^2(1-\nu^2)}\lambda^2 + \frac{Eh(1-\nu)}{2R^2(1-\nu^2)}n^2 \tag{3.26}$$

$$\mathcal{L}'_{12} = \mathcal{L}'_{21} = -\frac{Eh(1+\nu)}{2R^2(1-\nu^2)}\lambda n \tag{3.27}$$

$$\mathcal{L}'_{13} = \mathcal{L}'_{31} = -\frac{Eh\nu}{R^2(1-\nu^2)}\lambda \tag{3.28}$$

$$\mathcal{L}'_{22} = -\rho_s h\omega^2 + \frac{Eh(1-\nu)}{2R^2(1-\nu^2)}\lambda^2 + \frac{Eh}{R^2(1-\nu^2)}n^2 \tag{3.29}$$

$$\mathcal{L}'_{23} = \mathcal{L}'_{32} = \frac{Eh}{R^2(1-\nu^2)}n \tag{3.30}$$

$$\mathcal{L}'_{33} = -\rho_s h\omega^2 + \frac{Eh\mu}{R^2(1-\nu^2)}(\lambda^2+n^2)^2 + \frac{Eh}{R^2(1-\nu^2)} \tag{3.31}$$

The parameter λ is defined as $\lambda = m\pi R/L$, which is consistent with the expression presented in Leissa's report (1973). It can be seen that the *U*, *V* and *W* degrees of freedom are coupled through the stiffness matrix. If the radial displacement $\xi_{3mn} = \gamma_{mn}$ is known, then the free vibration problem

$$[\mathcal{L}']\{\xi_{mn}\} = 0 \tag{3.32}$$

can be written as

$$\begin{bmatrix} \mathcal{L}'_{11} & \mathcal{L}'_{12} \\ \mathcal{L}'_{21} & \mathcal{L}'_{22} \end{bmatrix} \begin{bmatrix} \alpha_{mn}/\gamma_{mn} \\ \beta_{mn}/\gamma_{mn} \end{bmatrix} = \begin{bmatrix} -\mathcal{L}'_{13} \\ -\mathcal{L}'_{23} \end{bmatrix} \tag{3.33}$$

Only pressure forces can be exerted on the cylinder and $f_z = f_\theta = 0$. Under this condition the modal force equilibrium equations can be written as

$$\mathcal{L}'_{11}\alpha_{mn} + \mathcal{L}'_{12}\beta_{mn} = -\mathcal{L}'_{13}\gamma_{mn} \tag{3.34}$$

$$\mathcal{L}'_{21}\alpha_{mn} + \mathcal{L}'_{22}\beta_{mn} = -\mathcal{L}'_{23}\gamma_{mn} \tag{3.35}$$

$$(\mathcal{L}'_{31}\alpha_{mn} + \mathcal{L}'_{32}\beta_{mn} + \mathcal{L}'_{33}\gamma_{mn})W_{3mn} = f_{rmn} \tag{3.36}$$

Substitute α_{mn} and β_{mn} into the radial modal force equilibrium equation to obtain

$$(\mathcal{L}_1'' + \mathcal{L}_2'' + \mathcal{L}_3'')\gamma_{mn}W_{3mn} = f_{rmn} \tag{3.37}$$

with

$$
\begin{aligned}
&\mathcal{L}_1'' + \mathcal{L}_2'' + \mathcal{L}_3'' \\
&= -\rho_s h\omega^2 + \frac{Eh}{R^2(1-\nu^2)}[1 + \mu(\lambda^2 + n^2)^2] \\
&- \frac{Eh}{R^2(1-\nu^2)}\nu\lambda\left(\frac{-c_2\lambda n^2 + \nu\lambda\ \ (c_1\lambda^2 + n^2)}{(\lambda^2 + c_1 n^2)(c_1\lambda^2 + n^2) - (c_2\lambda n)^2}\right) \\
&+ \frac{Eh}{R^2(1-\nu^2)}n\left(\frac{c_2\nu\lambda^2 n\ \ - (\lambda^2 + c_1 n^2)n}{(\lambda^2 + c_1 n^2)(c_1\lambda^2 + n^2) - (c_2\lambda n)^2}\right)
\end{aligned}
\tag{3.38}
$$

Hence, the radial modal force equilibrium equation (3.40) becomes

$$
\begin{aligned}
&\left(-\omega^2[\rho_s h]\right. \\
&+ \frac{Eh}{R^2(1-\nu^2)}\left[1 + \mu(\lambda^2 + n^2)^2\right. \\
&\left.\left. + \frac{(2c_2\nu\lambda^2 - \lambda^2 - c_1 n^2)n^2 - (\nu\lambda)^2\ \ (c_1\lambda^2 + n^2)}{(\lambda^2 + c_1 n^2)(c_1\lambda^2 + n^2) - (c_2\lambda n)^2}\right]\right)\gamma_{mn}W_{3mn} \\
&= f_{rmn}
\end{aligned}
\tag{3.39}
$$

Summing over all (m, n) modes we obtain

$$
\begin{aligned}
&\sum_{m,n}\left(-\omega^2[\rho_s h]\right. \\
&+ \frac{Eh}{R^2(1-\nu^2)}\left[1 + \mu(\lambda^2 + n^2)^2\right. \\
&\left.\left. + \frac{(2c_2\nu\lambda^2 - \lambda^2 - c_1 n^2)n^2 - (\nu\lambda)^2\ \ (c_1\lambda^2 + n^2)}{(\lambda^2 + c_1 n^2)(c_1\lambda^2 + n^2) - (c_2\lambda n)^2}\right]\right)\gamma_{mn}W_{3mn} \\
&= \sum_{m,n} f_{rmn} = f_r
\end{aligned}
\tag{3.40}
$$

From the method of weighted residuals, we can multiply equation (3.43) by $W_{3j\ell}$ and integrated over the surface of the cylinder to obtain

$$\sum_{m,n}\gamma_{mn}\int_{-L}^{0}\int_{0}^{2\pi}W_{3j\ell}\Bigg(-\omega^2[\rho_s h]+\frac{Eh}{R^2(1-\nu^2)}\Bigg[1+\mu(\lambda^2+n^2)^2+\frac{(2c_2\nu\lambda^2-\lambda^2-c_1n^2)n^2-(\nu\lambda)^2\ \ (c_1\lambda^2+n^2)}{(\lambda^2+c_1n^2)(c_1\lambda^2+n^2)-(c_2\lambda n)^2}\Bigg]\Bigg)W_{3mn}\ \ R\ \ d\theta\ \ dz$$
$$=\int_{-L}^{0}\int_{0}^{2\pi}W_{3j\ell}f_r(z,\theta)\ \ R\ \ d\theta\ \ dz \tag{3.41}$$

which can be rewritten as

$$\sum_{m,n}\left(-\omega^2M_{j\ell mn}+C_{j\ell mn}\right)\gamma_{mn}=\int_{-L}^{0}\int_{0}^{2\pi}W_{3j\ell}(z,\theta)f_r(z,\theta)R\ \ d\theta\ \ dz \tag{3.42}$$

with mass matrix

$$M_{j\ell mn}=\rho_s h\int_{-L}^{0}\int_{0}^{2\pi}W_{3j\ell}W_{3mn}\,R\ \ d\theta\ \ dz=\rho_s 2\pi RLh\left(\frac{\delta_{jm}}{2}\right)\left(\frac{\delta_{\ell n}}{\varepsilon_\ell}\right) \tag{3.43}$$

and stiffness matrix

$$C_{j\ell mn}$$
$$=\frac{Eh}{R^2(1-\nu^2)}\Bigg[1+\mu(\lambda^2+n^2)^2+\frac{(2c_2\nu\lambda^2-\lambda^2-c_1n^2)n^2-(\nu\lambda)^2\ \ (c_1\lambda^2+n^2)}{(\lambda^2+c_1n^2)(c_1\lambda^2+n^2)-(c_2\lambda n)^2}\Bigg]\int_{-L}^{0}\int_{0}^{2\pi}W_{3j\ell}W_{3mn}\,R\ \ d\theta\ \ dz$$
$$=2\pi\frac{EhL}{R(1-\nu^2)}\Bigg[1+\mu(\lambda^2+n^2)^2+\frac{(2c_2\nu\lambda^2-\lambda^2-c_1n^2)n^2-(\nu\lambda)^2\ \ (c_1\lambda^2+n^2)}{(\lambda^2+c_1n^2)(c_1\lambda^2+n^2)-(c_2\lambda n)^2}\Bigg]\left(\frac{\delta_{jm}}{2}\right)\left(\frac{\delta_{\ell n}}{\varepsilon_\ell}\right) \tag{3.44}$$

where δ_{jm} is the Kronecker delta and ε_n is the Jacobi factor:

$$\delta_{jm} = \begin{cases} 1 & \text{for} \quad j = m \\ 0 & \text{for} \quad j \neq m \end{cases} \tag{3.45}$$

$$\varepsilon_n = \begin{cases} 1 & \text{for} \quad n = 0 \\ 2 & \text{for} \quad n \geq 1 \end{cases} \tag{3.46}$$

3.1.5. Hydrostatic stiffness matrix

In order to complete the equations of motion, we need to determine the hydrostatic stiffness matrix. This can be done by calculating the hydrostatic contributions from the external pressure. The integral on the right hand side of equation (3.44) represents the linearized pressure force on the cylinder. The external pressure on the cylinder $-f_r$ can be decomposed into hydrodynamic and hydrostatic contributions according to

$$-f_r(z,\theta) = -i\omega\rho\varphi(R,\theta,z) - \rho g z \tag{3.47}$$

The total hydrostatic force on the cylinder is

$$\begin{aligned} -\rho g \int_{-L}^{0}\int_{0}^{2\pi} \sum_{m=1}^{\infty}\sum_{n=0}^{\infty} \gamma_{mn} \sin(m\pi z/L)\cos(n\theta)\, z \;\; R \;\; d\theta \;\; dz \\ = -\rho g \int_{-L}^{0}\int_{0}^{2\pi} W_{3j\ell}(z,\theta) \;\; z \;\; R \;\; d\theta \;\; dz \end{aligned} \tag{3.48}$$

According to Newman (1994), the hydrostatic stiffness matrix is determined as

$$c_{j\ell mn} = -\rho g \int_{-L}^{0}\int_{0}^{2\pi} \left(w_{jl} + zD_{jl}\right) W_{3mn} \;\; R \;\; d\theta \;\; dz \tag{3.49}$$

where w_{jl} is the vertical Cartesian component of the shape function W_{3jl} and the divergence

$$D_{jl} = \nabla \cdot \{W_{3jl}\} \tag{3.50}$$

The Cartesian components of the shape function W_{3jl} are

$$\begin{bmatrix} u_{jl} \\ v_{jl} \\ w_{jl} \end{bmatrix} = \begin{bmatrix} \sin(j\pi z/L)\cos(\ell\theta)\cos(\theta) \\ \sin(j\pi z/L)\cos(\ell\theta)\sin(\theta) \\ \cos(j\pi z/L)\cos(\ell\theta) \end{bmatrix} \tag{3.51}$$

In order to evaluate the divergence of W_{3jl} in Cartesian coordinates, we apply the Tchebytchev decomposition of $\cos(\ell\theta)$

$$\begin{aligned} \cos(\ell\theta) &= \sum_{k=0}^{\left[\frac{\ell}{2}\right]} \binom{\ell}{\ell - 2k} (-1)^k (\cos\theta)^{\ell-2k} (1-(\cos\theta)^2)^k \\ &= T_\ell(\cos\theta) \end{aligned} \tag{3.52}$$

With

$$\begin{aligned} T_0(\cos\theta) &= 1 \\ T_1(\cos\theta) &= \cos\theta \\ T_\ell(\cos\theta) &= 2\ \cos\theta\ \ T_{\ell-1}(\cos\theta) - T_{\ell-2}(\cos\theta) \quad \text{for} \quad \ell \geq 2 \end{aligned} \tag{3.53}$$

WAMIT assumes that unit normals on the cylinder are pointed inward from the fluid domain toward the center of the cylinder; therefore a positive divergence should be associated with a decrease in buoyancy. This means that

$$\begin{aligned} D_{j0} &= -\frac{\partial u_{j0}}{\partial x} - \frac{\partial v_{j0}}{\partial y} - \frac{\partial w_{j0}}{\partial z} = \left[\frac{j\pi}{L} - \frac{1}{R}\right] \sin\left(\frac{j\pi z}{L}\right) \\ D_{j1} &= -\frac{\partial u_{j1}}{\partial x} - \frac{\partial v_{j1}}{\partial y} - \frac{\partial w_{j1}}{\partial z} = \left[\frac{j\pi}{L} - \frac{1}{R}\right] \sin\left(\frac{j\pi z}{L}\right) \cos\theta \\ D_{j2} &= -\frac{\partial u_{j2}}{\partial x} - \frac{\partial v_{j2}}{\partial y} - \frac{\partial w_{j2}}{\partial z} = \left[\frac{j\pi}{L} - \frac{1}{R}\right] \sin\left(\frac{j\pi z}{L}\right) \cos(2\theta) \end{aligned} \tag{3.54}$$

Evidently,

$$D_{jl} = \left[\frac{j\pi}{L} - \frac{1}{R}\right]\ \sin\left(\frac{j\pi z}{L}\right) \cos(\ell\theta) \tag{3.55}$$

The hydrostatic stiffness matrix can be separated into two components:

$$c^{(1)}_{j\ell mn} = -\rho g \int_{-L}^{0}\int_{0}^{2\pi} w_{jl} W_{3mn}\ R\ d\theta\ dz$$

$$= -\rho g \int_{-L}^{0}\int_{0}^{2\pi} \sin\left(\frac{m\pi z}{L}\right)\cos(n\theta)\cos\left(\frac{j\pi z}{L}\right)\cos(\ell\theta)\, R\ d\theta\ dz \tag{3.56}$$

$$= \begin{cases} -\rho g \dfrac{RL\delta_{\ell n}}{\varepsilon_{\ell n}}\left[\dfrac{\cos\big((m-j)\pi\big)-1}{(m-j)} + \dfrac{\cos\big((m+j)\pi\big)-1}{(m+j)}\right] & \text{for} \quad |m-j| = 1 \\ 0 & \text{otherwise} \end{cases}$$

where

$$\varepsilon_{\ell n} = \begin{cases} 1 & \text{for} \quad (\ell \times n) = 0 \\ 2 & \text{for} \quad (\ell \times n) \geq 1 \end{cases} \tag{3.57}$$

and

$$c^{(2)}_{j\ell mn} = -\rho g \int_{-L}^{0}\int_{0}^{2\pi} z\ D_{jl}\ W_{3mn}\ R\ d\theta\ dz$$

$$= -\rho g \int_{-L}^{0}\int_{0}^{2\pi} z\ \sin\left(\frac{m\pi z}{L}\right)\cos(n\theta)\sin\left(\frac{j\pi z}{L}\right)\cos(l\theta)\, d\theta\ dz \tag{3.58}$$

From equation (3.58), the second component of the hydrostatic stiffness matrix is

$$c^{(2)}_{j\ell mn} = -\rho g \int_{-L}^{0}\int_{0}^{2\pi} z\ D_{jl}\ W_{3mn}\ R\ d\theta\ dz$$

$$= -\rho g \int_{-L}^{0}\int_{0}^{2\pi} z\left[\frac{j\pi}{L} - \frac{1}{R}\right]\ \sin\left(\frac{j\pi z}{L}\right)\ \sin\left(\frac{m\pi z}{L}\right)\cos(\ell\theta)\ \cos(n\theta)\ R\ d\theta\ dz \tag{3.59}$$

$$= \begin{cases} \rho g L^2 \dfrac{\delta_{\ell n}}{\pi\varepsilon_{\ell n}}\left(1 - \dfrac{j\pi R}{L}\right)\left[\dfrac{\cos\big((m+j)\pi\big)-1}{(m+j)^2} - \dfrac{\cos\big((m-j)\pi\big)-1}{(m-j)^2}\right] & \text{for}\ \ m \neq j \\ \rho g L^2 \dfrac{\pi\delta_{\ell n}}{2\varepsilon_{\ell n}}\left(1 - \dfrac{j\pi R}{L}\right) & \text{for}\ \ m = j \end{cases}$$

The velocity potential can be decomposed into diffracted and radiated components according to

$$\phi = \varphi e^{i\omega t} = \phi_{\mathrm{D}} + \phi_{\mathrm{R}} = \left(\varphi_{\mathrm{D}} + \sum_{m} \gamma_{mn}\varphi_{mn}\right) e^{i\omega t} \tag{3.60}$$

The diffracted velocity potential can be further decomposed into incident and scattered wave components according to

$$\phi_{\mathrm{D}} = \phi_{\mathrm{I}} + \phi_{\mathrm{S}} = (\varphi_{\mathrm{I}} + \varphi_{\mathrm{S}}) e^{i\omega t} \tag{3.61}$$

The wave exciting force $F_{j\ell}$ can be found as

$$F_{j\ell} = -i\omega\rho \int_{-L}^{0}\int_{0}^{2\pi} W_{3j\ell}\ (\varphi_{\mathrm{I}} + \varphi_{\mathrm{S}})|_{r=R}\quad R\ d\theta\ dz \tag{3.65}$$

The radiation components will be further decomposed into added mass ($\omega^2 a_{j\ell mn}\gamma_{mn}$) and radiation damping ($-i\omega b_{j\ell mn}\gamma_{mn}$) contributions according to

$$\left(\omega^2 a_{j\ell mn} - i\omega b_{j\ell mn}\right)\gamma_{mn} = -i\omega\rho\gamma_{mn} \int_{-L}^{0}\int_{0}^{2\pi} W_{3j\ell}\ \varphi_{mn}\ R\ d\theta\ dz \tag{3.66}$$

Thus, we have the following set of equations of motion to be incorporated in WAMIT:

$$\sum_{m,n}\Big[-\omega^2\left(M_{j\ell mn} + a_{j\ell mn}\right) + i\omega b_{j\ell mn} + \left(C_{j\ell mn} + c^{(1)}_{j\ell mn} + c^{(2)}_{j\ell mn}\right)\Big]\gamma_{mn} = F_{j\ell} \tag{3.67}$$

3.1.6. Natural frequencies

The natural frequencies of the elastic cylinder may be determined by finding the roots of the characteristic equation, which is obtained by calculating the determinant of $[\mathcal{L}']$. Denoting

$$\Omega^2 = \frac{\rho_s(1-\nu^2)R^2\omega^2}{E} \tag{3.68}$$

the determinant of $[\mathcal{L}']$ is

$$\begin{vmatrix} -\Omega^2 + \lambda^2 + c_1 n^2 & -c_2\lambda n & -\nu\lambda \\ -c_2\lambda n & -\Omega^2 + c_1\lambda^2 + n^2 & n \\ -\nu\lambda & n & -\Omega^2 + 1 + \mu(\lambda^2 + n^2)^2 \end{vmatrix} \tag{3.69}$$

Setting the determinant of $[\mathcal{L}']$ equal to zero leads to the frequency equation

$$\Omega^6 - K_2\Omega^4 + K_1\Omega^2 - K_0 = 0 \tag{3.70}$$

where

$$K_2 = 1 + (1 + c_1)(n^2 + \lambda^2) + \mu(n^2 + \lambda^2)^2 \tag{3.71}$$

$$K_1 = c_1[(3 + 2\nu)\lambda^2 + n^2 + (n^2 + \lambda^2)^2] + (1 + c_1)\mu(n^2 + \lambda^2)^3 \tag{3.72}$$

$$K_0 = c_1[(1 - \nu^2)\lambda^4 + \mu(n^2 + \lambda^2)^4] \tag{3.73}$$

Each of the roots of equation (3.70) is associated with a natural frequency ω_n. According to Leissa (1973), the lowest one corresponds to radial displacements. In order to set the natural frequency of the shell in the range of studied wave frequencies, the material properties of the cylinder are chosen. Table 3.1 presents the selected material properties and geometric characteristics of the cylinder. Table 3.2 shows the natural periods associated with each (m, n) mode of vibration. Note that these natural periods of the cylinder are determined under the assumption that there is no interior flow inside the cylinder. For the case where the cylinder is filled with water, the natural period need to be identified through the calculation of the Response Amplitude Operator (RAO).

Table 3.1 Material properties of the elastic cylinder

Parameter	Value
Radius of cylinder, R	4.3m
Draft of cylinder, d	10.5m
Water depth, L	10.5m
Thickness of cylinder, h	0.025m
Poisson's coefficient, v	0.49
Young's modulus, E	1 MPa
Density, ρ_s	2300 kg/m^3

Table 3.2 Natural periods of the elastic cylinder (not filled with water).

	n=0	n=1	n=2	n=3
m=1	1.7386	2.6834	5.0069	8.7874
m=2	1.3218	1.5815	2.2207	3.2043
m=3	1.3061	1.4063	1.6891	2.1351
m=4	1.3001	1.3529	1.5076	1.7574

3.1.7. Diffraction and radiation potentials – exterior flow

The incident wave propagating in the $\theta = 0$ direction can be expressed in cylindrical coordinates as:

$$\phi_I(r,\theta,z,t) = i\frac{gA}{\omega}\ \frac{\cosh(k(z+L))}{\cosh(kL)}\ \left\{\sum_{n=0}^{\infty} i^{-n}\varepsilon_n\ J_n(kr)\ \cos(n\theta)\right\} e^{i\omega t} \tag{3.74}$$

where $J_n(kr)$ is the Bessel function of the first kind and

$$\varepsilon_n = \begin{cases} 1 & \text{for} \quad n = 0 \\ 2 & \text{for} \quad n \geq 1 \end{cases} \tag{3.75}$$

The free surface elevation associated with this velocity potential is

$$\begin{aligned} \eta_{\mathrm{I}} &= -\frac{1}{g}\frac{\partial \Phi_{\mathrm{I}}}{\partial t}\bigg|_{z=0} \\ &= \mathrm{Re}\left\{ A e^{i\omega t} \sum_{n=0}^{\infty} i^{-n} \varepsilon_n \; J_n(kr)\cos(n\theta) \right\} \\ &= A\cos(kx - \omega t) \end{aligned} \tag{3.76}$$

The first-order velocity potential for the wave scattered by a rigid, bottom-mounted circular cylinder in the domain $r \geq R$, expressed in cylindrical coordinates, is given by MacCamy and Fuchs (1954):

$$\begin{aligned} \phi_{\mathrm{s}}(r,\theta,z,t) = \; & -i\frac{gA}{\omega} \; \frac{\cosh\big(k(z+L)\big)}{\cosh(kL)} \cdot \\ & \left\{ \sum_{n=0}^{\infty} i^{-n} \varepsilon_n \; \frac{J_n'(kR)}{\left[H_n^{(2)}(kR)\right]'} \; H_n^{(2)}(kr) \; \cos(n\theta) \right\} e^{i\omega t} \end{aligned} \tag{3.77}$$

where $H_n^{(2)}(kr)$ is the Hankel function of the second kind and $[\cdot]'$ denotes the derivative with respect to the argument of the function. For the deformable cylinder the scattering potential is the same as the one for the non-deformable body as specified by Newman (1994).

The first-order pressure on the cylinder due to the combined effects of the incident and scattered waves is

$$
\begin{aligned}
&-\rho \frac{\partial \Phi_{\mathrm{D}}}{\partial t}\Big|_{r=R} \\
&= \rho g A \ \frac{\cosh(k(z+L))}{\cosh(kL)} \ \left\{ \sum_{n=0}^{\infty} i^{-n} \varepsilon_n \ \left[J_n(kR) \right.\right. \\
&- \left.\left. \frac{J_n'(kR)}{\left[H_n^{(2)}(kR)\right]'} \ H_n^{(2)}(kR) \right] \ \cos(n\theta) \right\} e^{i\omega t} \qquad (3.78) \\
&= -2i \frac{\rho g A}{\pi k R} \ \frac{\cosh(k(z+L))}{\cosh(kL)} \ \left\{ \sum_{n=0}^{\infty} \frac{i^{-n} \varepsilon_n}{\left[H_n^{(2)}(kR)\right]'} \ \cos(n\theta) \right\} e^{i\omega t}
\end{aligned}
$$

where use is made of the identity

$$
J_n(kR) - \frac{J_n'(kR)}{\left[H_n^{(2)}(kR)\right]'} \ H_n^{(2)}(kR) = -\frac{2i}{\pi k R \left[H_n^{(2)}(kR)\right]'} \qquad (3.79)
$$

The diffraction force on the rigid cylinder (without the $e^{i\omega t}$ factor) is

$$
\begin{aligned}
F_D &= -i\omega\rho \int_{-L}^{0} \int_{0}^{2\pi} (\varphi_{\mathrm{I}} + \varphi_{\mathrm{S}})|_{r=R} \, R \ \cos\theta \, d\theta \ dz \\
&= 2i \frac{\rho g A}{\pi k} \ \int_{-L}^{0} \frac{\cosh\big(k(z+L)\big)}{\cosh(kL)} dz \ \left\{ \int_{0}^{2\pi} \sum_{n=0}^{\infty} \frac{i^{-n} \varepsilon_n}{\left[H_n^{(2)}(kR)\right]'} \ \cos(n\theta) \cos\theta \, d\theta \right\} \qquad (3.80) \\
&= 4\rho g A \ \frac{\tanh(kL)}{k^2 \left[H_1^{(2)}(kR)\right]'}
\end{aligned}
$$

and the diffraction moment about the origin of the global coordinate system is

$$M_D = -i\omega\rho \int_{-L}^{0}\int_{0}^{2\pi} (\varphi_{\mathrm{I}} + \varphi_{\mathrm{S}})|_{r=R} \;\; z \;\; R \;\; \cos\theta \, d\theta \;\; dz$$

$$= \;\; 2i\frac{\rho g A}{\pi k} \;\; \int_{-L}^{0} \frac{z \;\; \cosh\big(k(z+L)\big)}{\cosh(kL)} dz \;\; \left\{ \int_{0}^{2\pi} \sum_{n=0}^{\infty} \frac{i^{-n}\varepsilon_n}{\left[H_n^{(2)}(kR)\right]'} \;\; \cos(n\theta)\cos\theta \, d\theta \right\} \quad (3.81$$

$$= 4\rho g A \;\; \frac{[\mathrm{sech}(kL) - 1]}{k^3\left[H_1^{(2)}(kR)\right]'}$$

The deformable cylinder has a pulsating boundary with oscillatory radial displacements about $r = R$. Dean and Dalrymple (1991) gave an analytical solution for the velocity potential of a pulsating cylindrical wave maker which has radial displacements. In that case, the associated radial velocity is

$$\frac{\partial}{\partial t} W(z,\theta,t) = i\omega \sum_{m=1}^{\infty}\sum_{n=0}^{\infty} \gamma_{mn} \sin(m\pi z/L)\cos(n\theta)\, e^{i\omega t} \tag{3.82}$$

and the velocity potential of the radiated wave field in the domain $r \geq R$, in cylindrical coordinates, is

$$\begin{aligned} \phi_{\mathrm{R}}(r,\theta,z,t) = \;\; & -i\frac{g}{\omega} \sum_{m=1}^{\infty}\sum_{n=0}^{\infty} \Bigg\{ P_{mn} \;\; H_n^{(1)}(kr)\cosh\big(k(z+L)\big) \\ & + \left[\sum_{q=1}^{\infty} E_{mnq} \;\; K_n\big(\kappa_q r\big) \;\; \cos\Big(\kappa_q (z \right. \\ & \left. + L)\Big) \right] \Bigg\} \cos(n\theta) e^{i\omega t} \end{aligned} \tag{3.83}$$

where $H_n^{(1)}(kr)$ is the Hankel function of the first kind and $K_n\big(\kappa_q r\big)$ is the modified Bessel function of the second kind.

For the propagating wave, the following dispersion relation has to be satisfied:

$$\omega^2 = gk\tanh(kL) \tag{3.84}$$

while the wavenumber κ_ℓ of the evanescent mode satisfies the dispersion relation

$$\omega^2 = -g\kappa_q \tan(\kappa_q L) \tag{3.85}$$

At the boundary (r=R), the radial velocity of the thin shell must equal the radial velocity of the fluid, therefore

$$\begin{aligned} \left.\frac{\partial \phi_R}{\partial r}\right|_{r=R} &= \frac{\partial}{\partial t} W(z,\theta,t) \\ &= i\omega \sum_{m=1}^{\infty}\sum_{n=0}^{\infty} \gamma_{mn} \sin(m\pi z/L)\cos(n\theta)\, e^{i\omega t} \end{aligned} \tag{3.86}$$

Therefore for any (m, n) mode we must have

$$\begin{aligned} \gamma_{mn}\sin\left(\frac{m\pi z}{L}\right) = -\frac{g}{\omega^2}\Bigg\{ & kP_{mn}\left[H_n^{(1)}(kR)\right]'\cosh\big(k(z+L)\big) \\ & + \left[\sum_{q=1}^{\infty} \kappa_q E_{mnq}\left[K_n(\kappa_q R)\right]' \cos\Big(\kappa_q(z+L)\Big)\right]\Bigg\} \end{aligned} \tag{3.87}$$

Multiply equation (3.87) by $\cosh\big(k(z+L)\big)$, and multiply equation (3.87) by $\cos\Big(\kappa_q(z+L)\Big)$. Then we integrate them over the water depth to obtain

$$\begin{aligned} P_{mn} &= -\gamma_{mn}\frac{\omega^2}{gk\left[H_n^{(1)}(kR)\right]'}\frac{\int_{-L}^{0}\sin(m\pi z/L)\cosh\big(k(z+L)\big)\quad dz}{\int_{-L}^{0}\cosh^2\big(k(z+L)\big)\quad dz} \\ &= -\gamma_{mn}\frac{4}{\left[H_n^{(1)}(kR)\right]'}\frac{(kL)\tanh(kL)\,(m\pi)[\cos(m\pi)-\cosh(kL)]}{[(m\pi)^2+\ (kL)^2][2kL+\sinh(2kL)]} \end{aligned} \tag{3.88}$$

$$E_{mnq} = -\gamma_{mn}\frac{\omega^2}{g\kappa_q\left[K_n(\kappa_q R)\right]'}\frac{\int_{-L}^{0}\sin\left(\frac{m\pi z}{L}\right)\cos\left(\kappa_q(z+L)\right)\quad dz}{\int_{-L}^{0}\cos^2\left(\kappa_q(z+L)\right)\quad dz}$$
$$= \gamma_{mn}\frac{4}{\left[K_n(\kappa_q R)\right]'}\frac{(\kappa_q L)\tan(\kappa_q L)(m\pi)\left[\cos(m\pi)-\cos(\kappa_q L)\right]}{\left[(m\pi)^2-\ (\kappa_q L)^2\right]\left[2\kappa_q L+\sin(2\kappa_q L)\right]} \tag{3.89}$$

Once P_{mn} and E_{mnq} are known, we can determine the added mass, radiation damping, and exciting force matrices using the analytical expressions for the velocity potentials of the incident, scattered and radiated waves

$$a_{j\ell mn}$$
$$= \rho\frac{8\pi\delta_{\ell n}}{\varepsilon_{\ell n}}RL^2\ \ Re\left\{\frac{1}{2kL+\sinh(2kL)}\frac{H_n^{(1)}(kR)}{\left[H_n^{(1)}(kR)\right]'}\right.$$
$$\cdot\frac{(m\pi)[\cos(m\pi)-\cosh(kL)]}{[(m\pi)^2+\ (kL)^2]}\ \ \frac{(j\pi)[\cos(j\pi)-\cosh(kL)]}{[(j\pi)^2+\ (kL)^2]} \tag{3.90}$$
$$+\sum_{q=1}^{\infty}\frac{1}{2\kappa_q L+\sin(2\kappa_q L)}\frac{K_n(\kappa_q R)}{\left[K_n(\kappa_q R)\right]''}$$
$$\left.\cdot\frac{(m\pi)\left[\cos(m\pi)-\cos(\kappa_q L)\right]}{\left[(m\pi)^2-\ (\kappa_q L)^2\right]}\ \ \frac{(j\pi)\left[\cos(j\pi)-\cos(\kappa_q L)\right]}{\left[(j\pi)^2-\ (\kappa_q L)^2\right]}\right\}$$

The radiation damping matrix is

$$b_{j\ell mn} = Re\left\{\rho\int_{-L}^{0}\int_{0}^{2\pi}W_{3j\ell}\ \ \varphi_{mn}\ \ R\ \ d\theta\ \ dz\right\}$$
$$= \frac{8\pi\delta_{\ell n}}{\varepsilon_{\ell n}}\rho RL^2\omega\ \ Re\left\{\frac{i}{2kL+\sinh(2kL)}\frac{H_n^{(1)}(kR)}{\left[H_n^{(1)}(kR)\right]'}\right. \tag{3.91}$$
$$\left.\cdot\frac{(m\pi)[\cos(m\pi)-\cosh(kL)]}{[(m\pi)^2+\ (kL)^2]}\ \ \frac{(j\pi)[\cos(j\pi)-\cosh(kL)]}{[(j\pi)^2+\ (kL)^2]}\right\}$$

The diffraction force vector is

$$F_{j\ell} = -i\omega\rho \int_{-L}^{0}\int_{0}^{2\pi} W_{3j\ell}\ (\varphi_{\mathrm{I}} + \varphi_{\mathrm{S}})|_{r=R} \quad R\ d\theta\ dz$$

$$= \begin{cases} \dfrac{\rho g A L}{k} \dfrac{4i}{\left[H_0^{(2)}(kR)\right]'} \dfrac{(j\pi)[\cos(j\pi) - \cosh(kL)]}{[(j\pi)^2 + (kL)^2]\cosh(kL)} & \text{for} \quad \ell = 0 \\ \dfrac{\rho g A L}{k} \dfrac{4}{\left[H_1^{(2)}(kR)\right]'} \dfrac{(j\pi)[\cos(j\pi) - \cosh(kL)]}{[(j\pi)^2 + (kL)^2]\cosh(kL)} & \text{for} \quad \ell = 1 \\ \dfrac{\rho g A L}{k} \dfrac{4i^{-\ell+1}}{\left[H_\ell^{(2)}(kR)\right]'} \dfrac{(j\pi)[\cos(j\pi) - \cosh(kL)]}{[(j\pi)^2 + (kL)^2]\cosh(kL)} & \text{for} \quad \ell \geq 2 \end{cases} \tag{3.92}$$

3.1.8. Radiation potentials – interior flow

The shell is designed to be very flexible for the case of the deformable cylinder. Therefore, in order to equilibrate the exterior hydrostatic pressure, the cylinder must be considered as filled with water. This means that the interior modes of fluid motion must be considered in the model, and the interior flow will be coupled to the exterior flow. The deformations of the cylinder will be forced by the pressure difference across the cylinder wall. We also assume that the fluid level inside the cylinder matches the mean water level outside the cylinder so that there is no net hydrostatic pressure on the cylinder wall.

The net radial pressure on the cylinder is therefore

$$f_r(z,\theta) = -i\omega\rho[\varphi_{RI}(R,\theta,z) - \varphi(R,\theta,z)] \tag{3.90}$$

Here, φ_{RI} is the radiation potential of the interior flow. Since the radius of the cylinder is small relative to the height, we assume that the symmetric pumping modes will be the primary modes so that $r = 0$ is an anti-node

$$\lim_{r\to 0} \frac{\partial \varphi_{RI}}{\partial r} = 0 \tag{3.91}$$

The radial boundary conditions suggest a radiation potential for the interior flow of the form

$$\begin{aligned}\phi_{RI}(r,\theta,z,t) &= \varphi_{RI}(r,\theta,z)e^{i\omega t} = \\ -i\frac{g}{\omega}\sum_{m=1}^{\infty}\sum_{n=0}^{\infty}\{Q_{mn}\ J_n(kr)\cosh\big(k(z+L)\big)\ &+ \\ \big[\sum_{s=1}^{\infty}D_{mns}\ I_n(\kappa_s r)\ \cos\big(\kappa_s(z+L)\big)\big]\}\cos(n\theta)e^{i\omega t}\end{aligned} \tag{3.92}$$

where $I_n(\kappa_s r)$ is the modified Bessel function of the first kind. At $r = R$, the radial velocity of the thin shell must equal the radial velocity of the fluid

$$\begin{aligned}\left.\frac{\partial\phi_{RI}}{\partial r}\right|_{r=R} &= \frac{\partial}{\partial t}W(z,\theta,t) \\ &= i\omega\sum_{m=1}^{\infty}\sum_{n=0}^{\infty}\gamma_{mn}\sin(m\pi z/L)\cos(n\theta)\,e^{i\omega t}\end{aligned} \tag{3.93}$$

Therefore, for any (m, n) mode we must have

$$\begin{aligned}&\gamma_{mn}\sin(m\pi z/L) \\ &= -\frac{g}{\omega^2}\Bigg\{\ kQ_{mn}\ \ [\ J_n(kR)]'\cosh\big(k(z+L)\big) \\ &+\left[\sum_{s=1}^{\infty}\kappa_s D_{mns}\ \ [I_n(\kappa_s R)]'\ \ \cos\big(\kappa_s(z+L)\big)\right]\Bigg\}\end{aligned} \tag{3.94}$$

Similarly, we multiply equation (3.94) by $\cosh\big(k(z+L)\big)$ and multiply equation (3.94) by $\cos\big(\kappa_s(z+L)\big)$. Integrating over the water depth leads to

$$Q_{mn} = -\gamma_{mn}\frac{\omega^2}{gk[J_n(kR)]'}\frac{\int_{-L}^{0}\sin(m\pi z/L)\cosh\big(k(z+L)\big)\quad dz}{\int_{-L}^{0}\cosh^2\big(k(z+L)\big)\quad dz}$$
$$= -\gamma_{mn}\frac{4}{[J_n(kR)]'}\frac{(kL)\tanh(kL)\,(m\pi)[\cos(m\pi)-\cosh(kL)]}{[(m\pi)^2+\ (kL)^2][2kL+\sinh(2kL)]} \tag{3.95}$$

$$D_{mns} = -\gamma_{mn}\frac{\omega^2}{g\kappa_s[I_n(\kappa_s R)]''}\frac{\int_{-L}^{0}\sin\left(\frac{m\pi z}{L}\right)\cos\big(\kappa_s(z+L)\big)\quad dz}{\int_{-L}^{0}\cos^2\big(\kappa_s(z+L)\big)\quad dz}$$
$$= \gamma_{mn}\frac{4}{[I_n(\kappa_s R)]''}\frac{(\kappa_s L)\tan(\kappa_s L)\,(m\pi)[\cos(m\pi)-\cos(\kappa_s L)]}{[(m\pi)^2-\ (\kappa_s L)^2][2\kappa_s L+\sin(2\kappa_s L)]} \tag{3.96}$$

The added mass matrix for the interior flow is

$$a^{(I)}_{j\ell mn} = Re\left\{+i\frac{\rho}{\omega}\int_{-L}^{0}\int_{0}^{2\pi} W_{3jn}\ \ \varphi_{RImn}\ \ R\ \ d\theta\ \ dz\right\}$$
$$= -\rho\frac{8\pi\delta_{\ell n}}{\varepsilon_{\ell n}}RL^2\ \ Re\Bigg\{\frac{1}{2kL+\sinh(2kL)}\frac{J_n(kR)(kR)}{[J_n(kR)(kR)]'}$$
$$\cdot\frac{(m\pi)[\cos(m\pi)-\cosh(kL)]}{[(m\pi)^2+\ (kL)^2]}\ \ \frac{(j\pi)[\cos(j\pi)-\cosh(kL)]}{[(j\pi)^2+\ (kL)^2]}$$
$$+\sum_{s=1}^{\infty}\frac{1}{2\kappa_s L+\sin(2\kappa_s L)}\frac{I_n(\kappa_s R)}{[I_n(\kappa_s R)]''}$$
$$\cdot\frac{(m\pi)[\cos(m\pi)-\cos(\kappa_s L)]}{[(m\pi)^2-\ (\kappa_s L)^2]}\quad\ \frac{(j\pi)[\cos(j\pi)-\cos(\kappa_s L)]}{[(j\pi)^2-\ (\kappa_s L)^2]}\Bigg\} \tag{3.97}$$

Since the evanescent modes do not contribute to radiation damping and $J_n(kR)$ is real valued for $n \geq 0$, we determine that the radiation damping matrix for the interior flow $b^{(I)}_{j\ell mn}$ is zero. As a result, the equations of motion for the generalized modes in the case where the elastic cylinder is filled with water will be:

$$\sum_{m,n}\left[-\omega^2\left(M_{j\ell mn}+a_{j\ell mn}+a^{(I)}_{j\ell mn}\right)+i\omega b_{j\ell mn}+C_{j\ell mn}\right]\gamma_{mn}=F_{j\ell} \qquad (3.98)$$

For the WAMIT setup, the body mass matrix $M_{j\ell mn}$ is calculated externally and incorporated into WAMIT as an external input in the .FRC file. Besides, to account for the fact that WAMIT will calculate the hydrostatic stiffness matrix $c^{(1)}_{j\ell mn}$ and use it in the calculation of the RAOs, the stiffness matrix input to WAMIT in the .FRC file should be $\left(C_{j\ell mn}-c^{(1)}_{j\ell mn}\right)$, with the matrix $c^{(1)}_{j\ell mn}$ calculated externally.

3.2. Radiation Surface Elevation of One Single Deformable Cylinder

WAMIT has been run to study the behavior of one single deformable cylinder in shallow water, and to verify the analytical expressions for added mass, radiation damping, exciting force and RAOs. The first nine generalized modes are considered in this section. Table 3.3 represents the index of these nine modes with respect to certain values of *m* and *n*. The total number of modes in the input file for WAMIT is fifteen, which includes both six fixed body modes and nine generalized modes. The radiated wave field for the first five generalized modes is shown from Figure 3.2 to Figure 3.6.

We can observe that as the mode index increases, the contribution of the radiated wave to the total wave field becomes smaller. Starting from the 4th mode, the radiation becomes negligible, especially when the distance from the cylinder is large.

Table 3.3 Index of generalized modes for a given pair of *m* and *n*.

	n=0	n=1	n=2
m=1	1	2	3
m=2	4	5	6
m=3	7	8	9

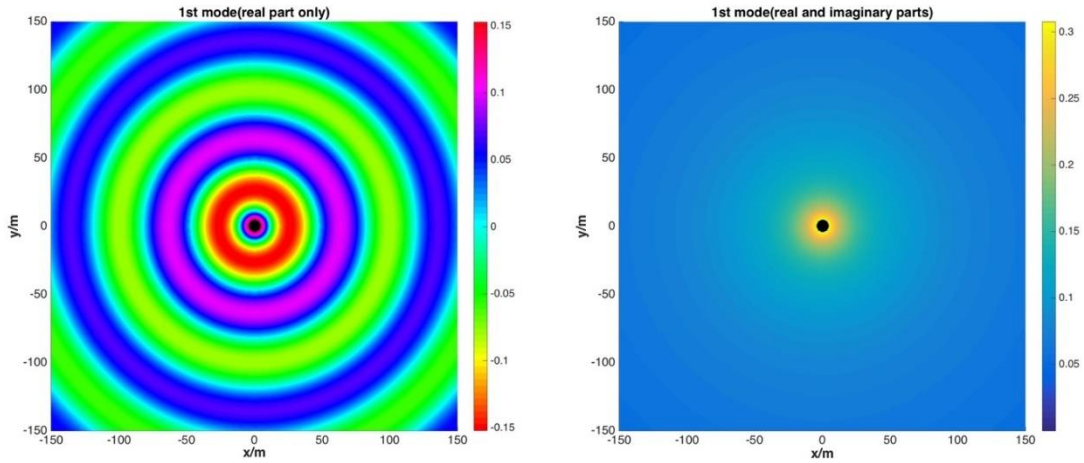

Figure 3.2. Surface elevations of radiated waves for the 1st generalized modes.

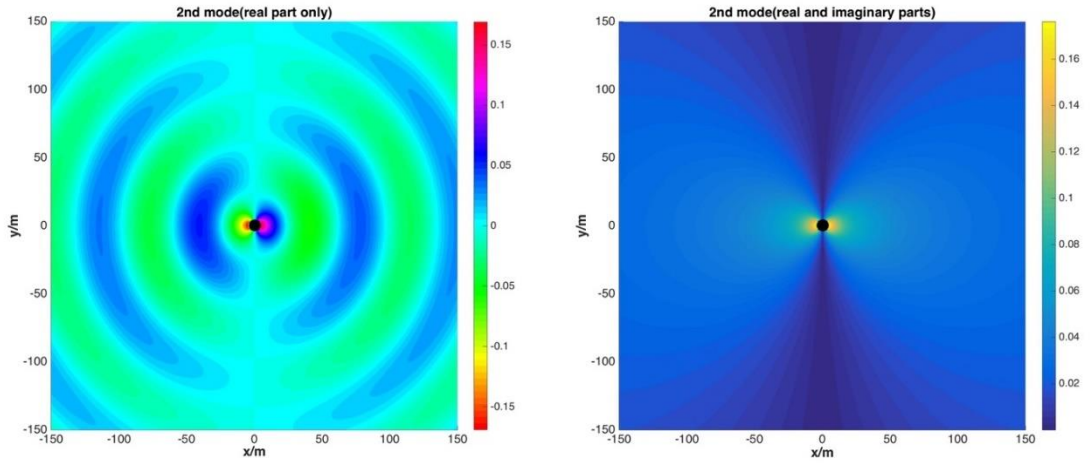

Figure 3.3. Surface elevations of radiated waves for the 2nd generalized modes.

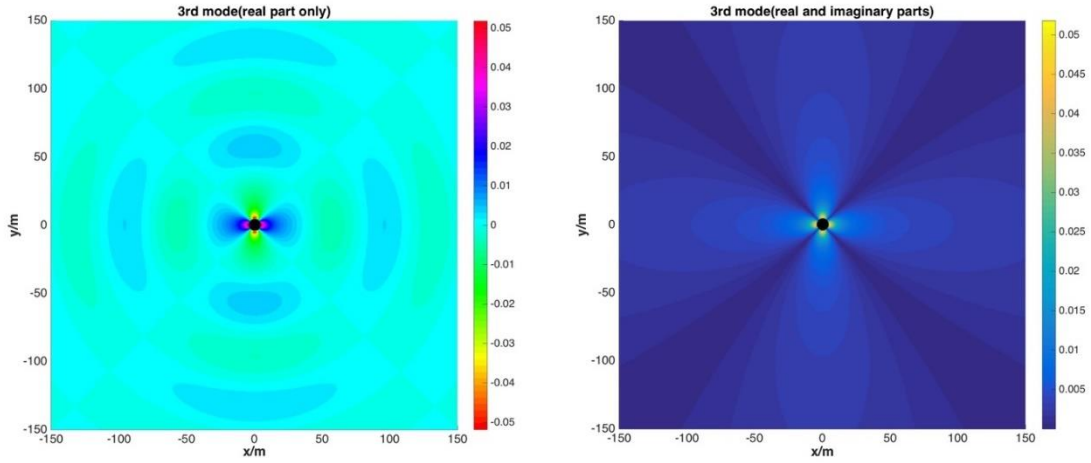

Figure 3.4. Surface elevations of radiated waves for the 3rd generalized modes.

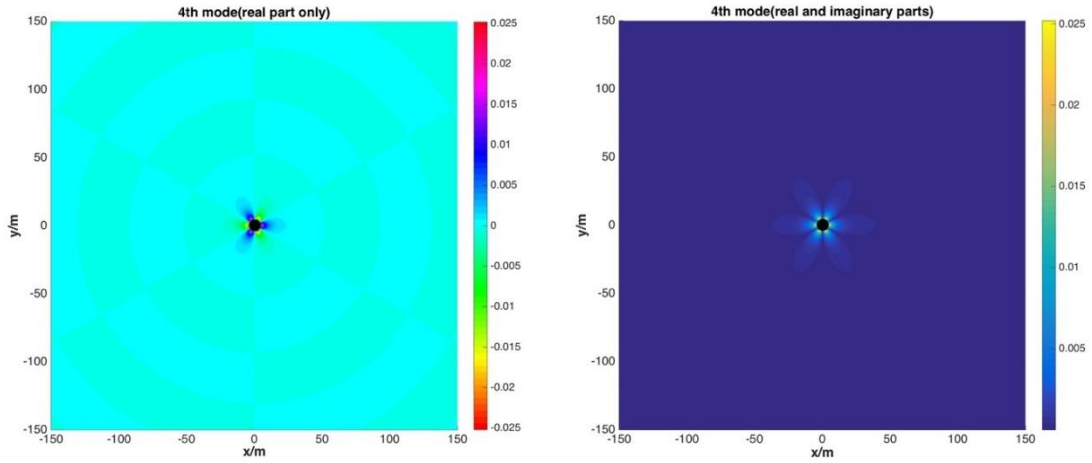

Figure 3.5. Surface elevations of radiated waves for the 4th generalized modes.

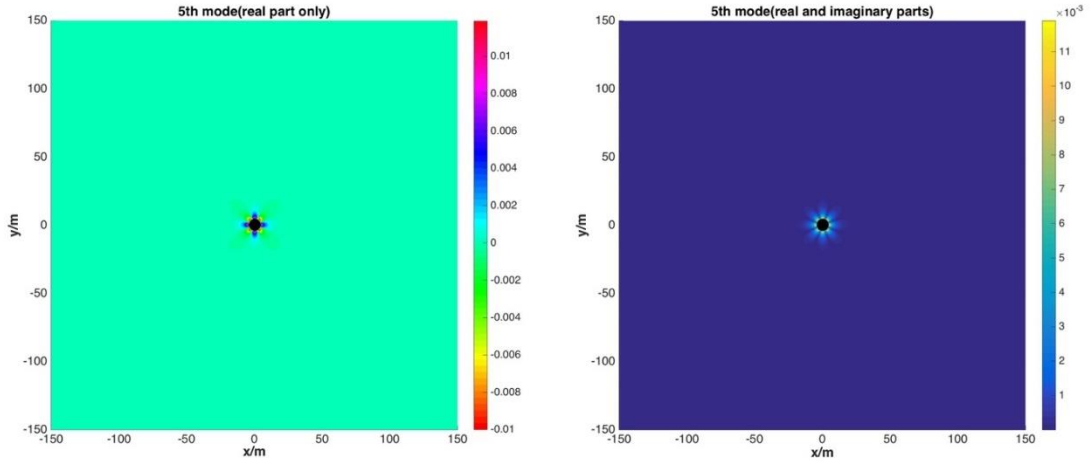

Figure 3.6. Surface elevations of radiated waves for the 5th generalized modes.

The added mass, radiation damping and exciting force coefficients of the first 6 generalized modes for the exterior flow are plotted from equation (3.90), equation (3.91) and equation (3.92) and are shown in Figures 3.7, 3.8 and 3.9. The numerical outputs from WAMIT are also shown in the figures. Comparing these two results, we can observe that

WAMIT's results are almost on top of the theoretical curves from our theory, which verifies the analytical expressions for the added mass, radiation damping and exciting force matrices. The good agreement between both results also demonstrates the accuracy for the evaluation of the velocity potentials using WAMIT's high-order method.

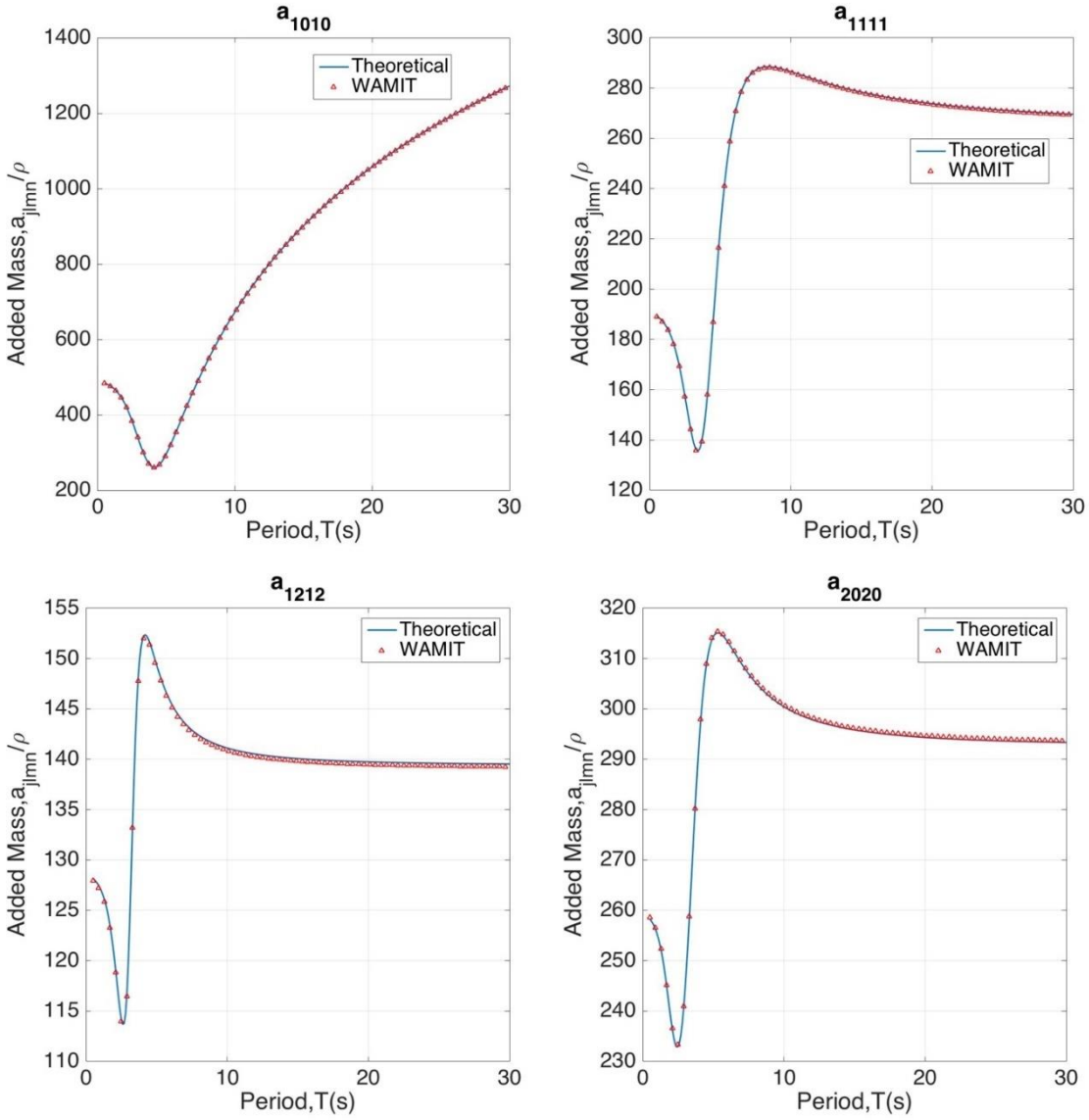

Figure 3.7. Added mass coefficients for the first six generalized modes.

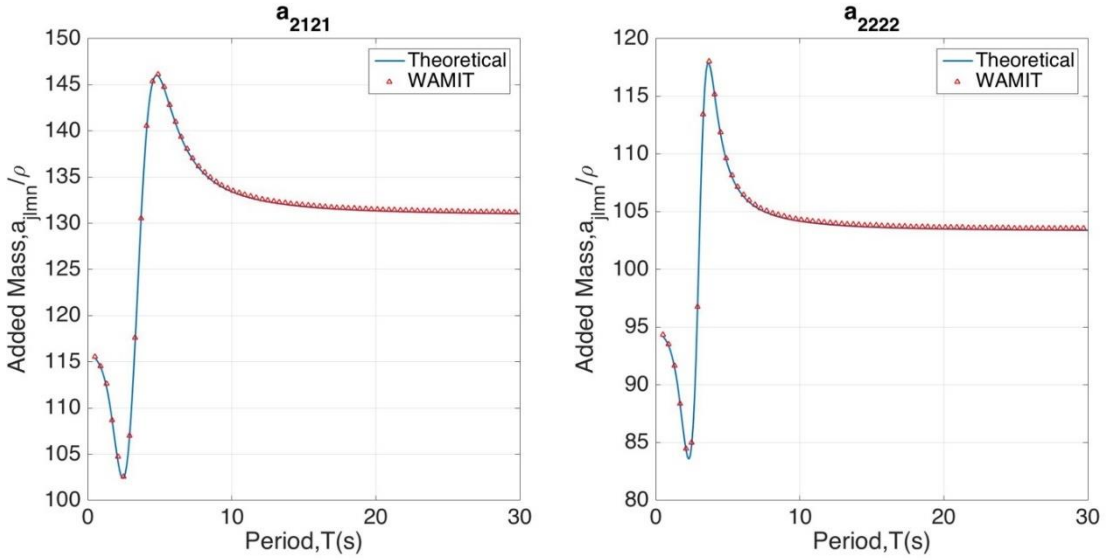

Figure 3.7. Continued.

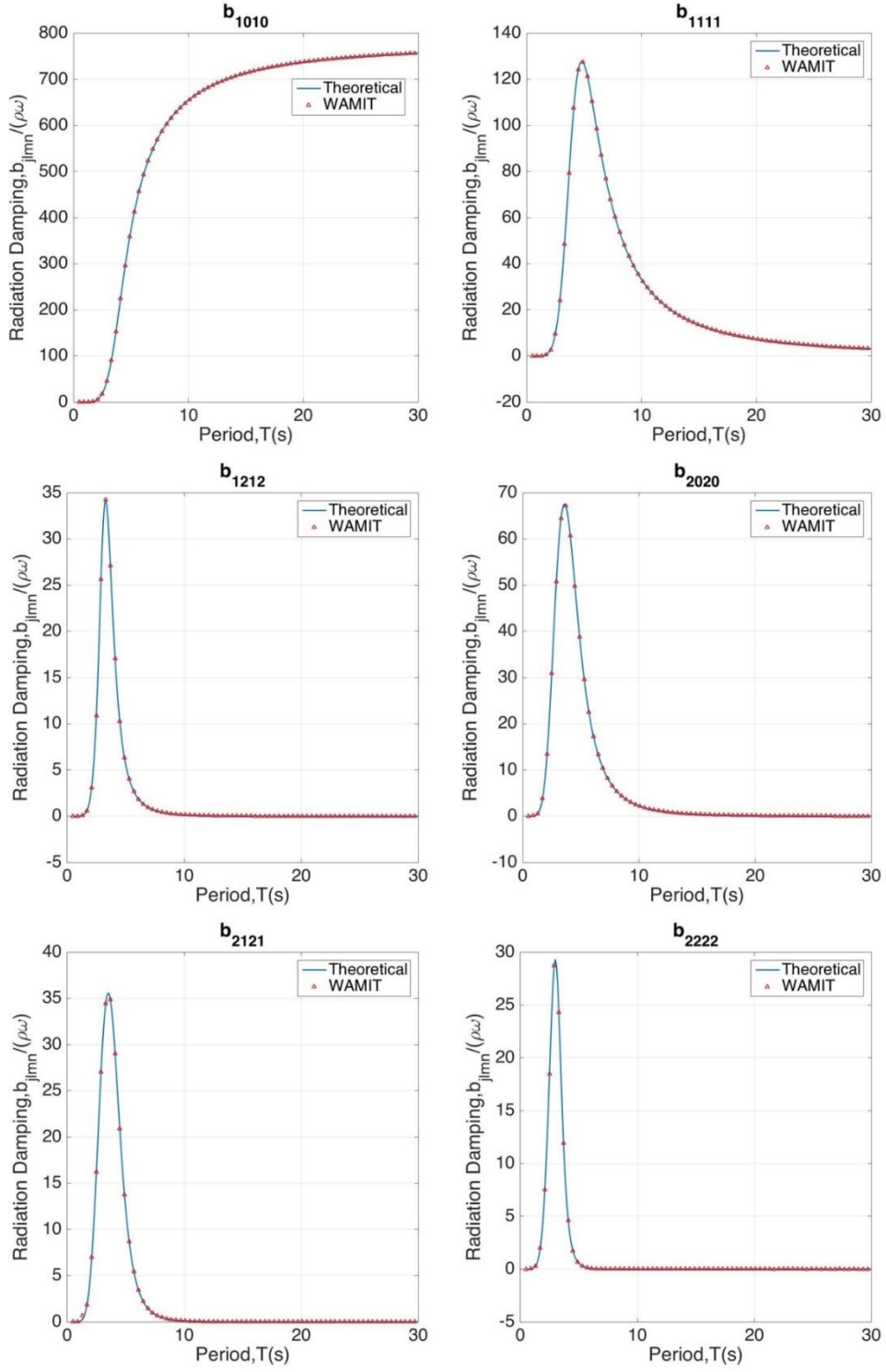

Figure 3.8. Damping coefficients for the first six generalized modes.

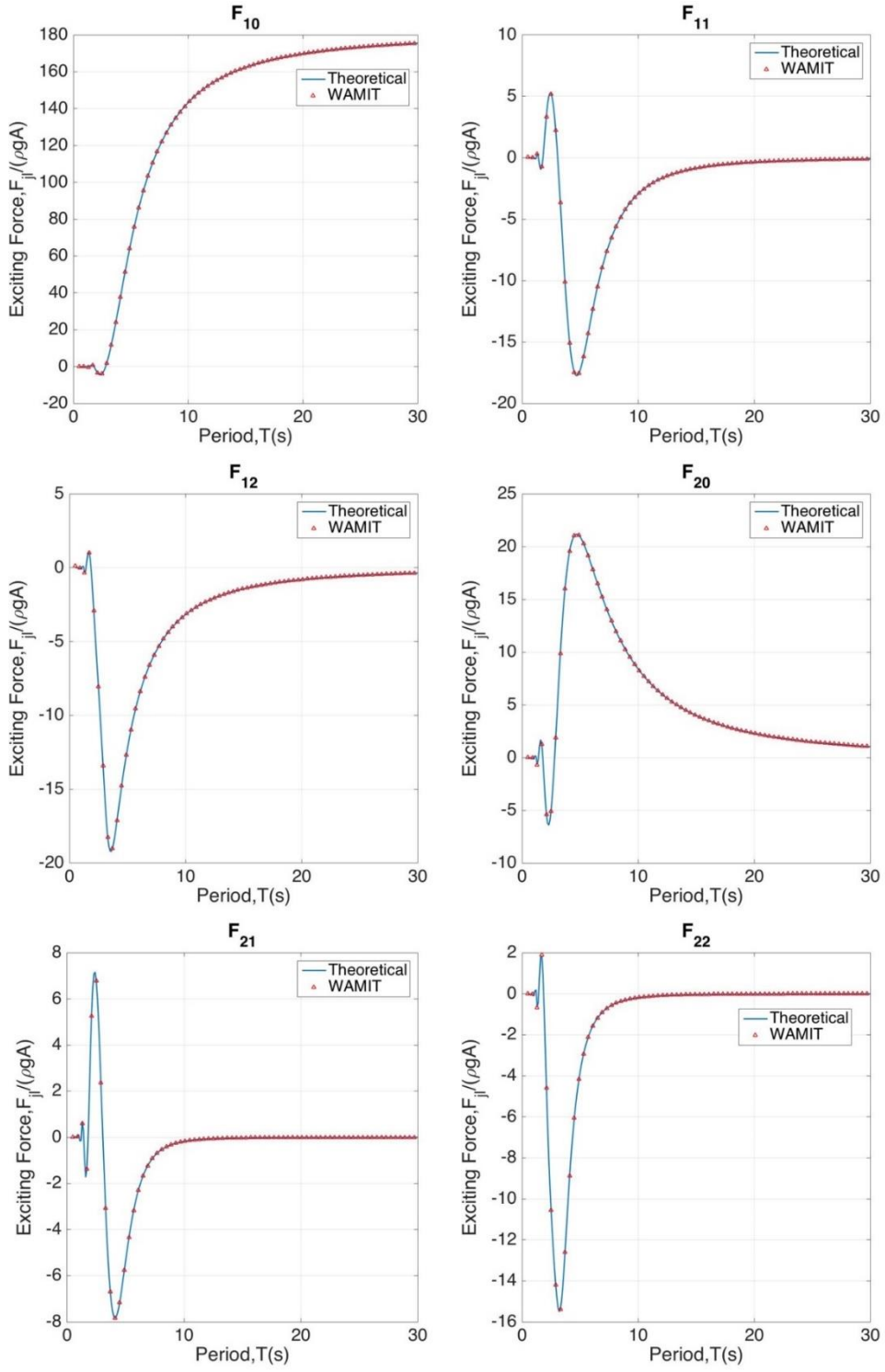

Figure 3.9. Exciting forces from Haskind relations for the first six generalized modes.

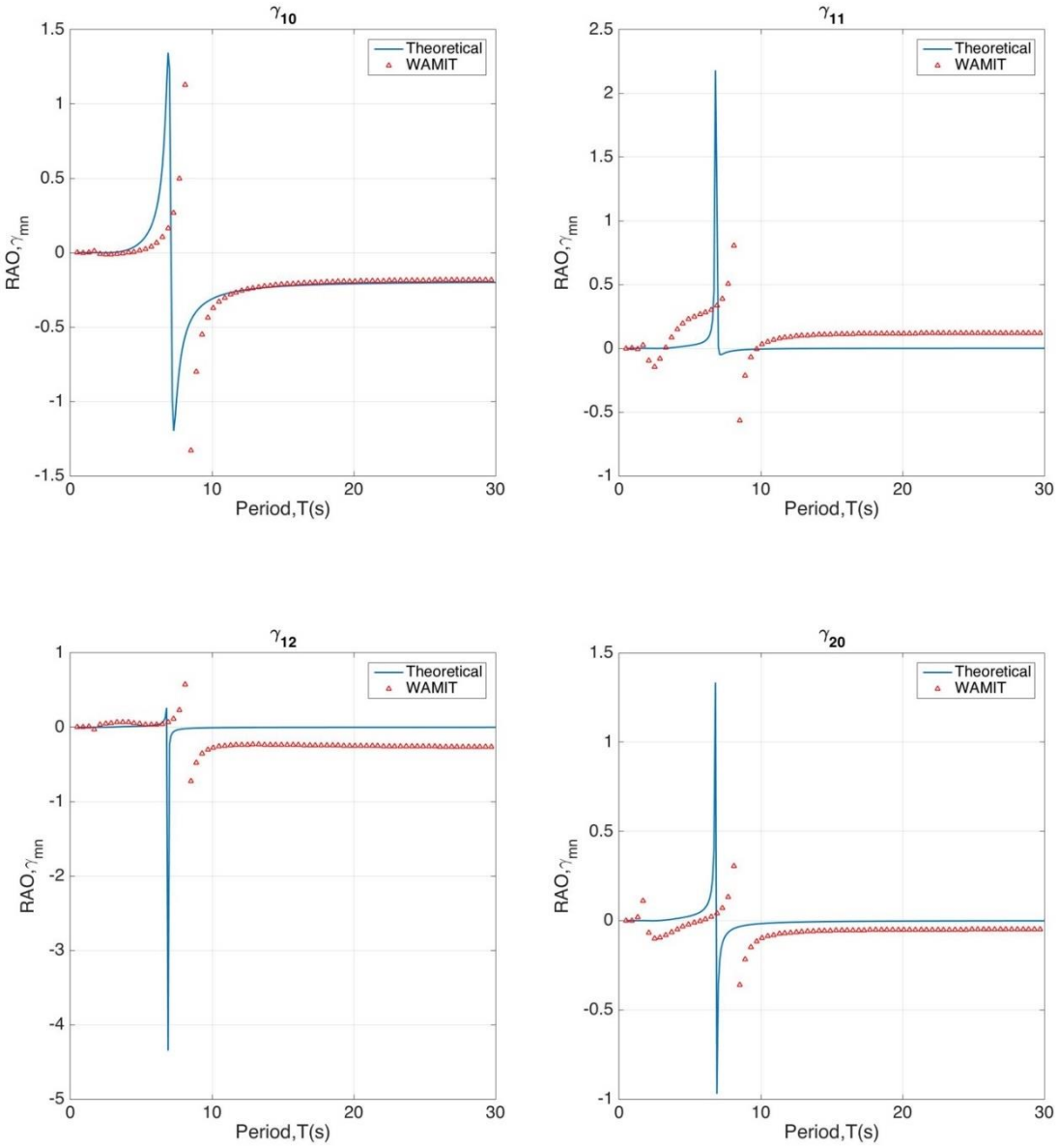

Figure 3.10. RAO for the first four generalized modes.

In addition, the RAOs for the first four modes are plotted in Figure 3.10. Agreement between the theoretical values and WAMIT's results has been reached. The 90 degree phase shift of the RAOs occurs at approximately 7.8 seconds, which indicates the natural periods associated with the first four modes are 7.8 seconds.

3.3. Natural Periods of One Single Deformable Cylinder Filled with Water: Comparison with Theoretical Values

Koga and Tsushima (1990) provided an asymptotic solution for the natural frequency of the vibration of a cylindrical shell filled with a liquid. The solution is valid for different combinations of boundary conditions at the top and bottom ends. The system considered is a circular cylindrical shell having a radius R, a length L, a thickness h, a mass per unit volume ρ_s, Poisson's ratio ν, and Young's modulus E. The shell is filled with a liquid having a mass per unit volume ρ. According to their theory, the equation for the radial displacement can yield a formula for the natural frequency:

$$\omega^2 = {\omega_0}^2 \left[1 + \frac{(1-\upsilon^2){\xi_1}^4}{\mu(n^2-1)^2}\right] \tag{3.99}$$

where ω_0 is the definite value of ω and can be expressed as:

$${\omega_0}^2 = \frac{\mu n^2 (n^2-1)^2}{\gamma n^2 + 1} \tag{3.100}$$

with $\mu = \frac{h^2}{12R^2} \ll 1$. n is the wave number for the interior flow. γ is defined as:

$$\gamma = 1 + \frac{\rho_\upsilon}{\rho_s} \tag{3.101}$$

where ρ_υ is the virtual mass of the liquid and is given approximately by:

$$\rho_\upsilon = \frac{\rho R}{nh} \tag{3.102}$$

In equation (3.99), ξ_1 is unknown and can be determined from the characteristic equations of the boundary conditions. In the present study, the ends of the cylindrical shell are clamped and the associated characteristic equation is as follows:

$$cosh(n\xi_1 L)\, cos(n\xi_1 L) - 1 = 0 \tag{3.103}$$

The eigenvalue ξ_1 is given as the minimum root of the characteristic equation:

$$\xi_1 = \frac{4.730 * R}{nL} \tag{3.104}$$

Equation (3.98) is used to determine the natural frequency of the vibrating thin shell. Once the natural frequency is obtained, it can be converted into natural period through the relation $T = \frac{2\pi}{\omega}$. The dimensions and structural parameters for the elastic cylinder in Table 3.1 are used in the calculation, and the resulting natural period is found to be 7.41 seconds, which is consistent with our observation from Figure 3.10.

4. ARRAYS OF BOTTOM-MOUNTED ELASTIC CYLINDERS

The preceding steps in the previous sections have been realized in order to study the wave interactions with elastic cylinder arrays. In the rigid cylinder cases, our setup of the WAMIT program has been validated by the effective medium approach and the theory of the Fabry–Pérot interferometer. For the elastic cylinder, the generalized deformation modes incorporated in WAMIT are also proven to be successful. Material properties of the deformable cylinder have been chosen so that the natural period of the "breathing" mode is in the range of studied incident wave periods. In this final section, both the radiation and the diffraction problems of deformable cylinder arrays will be taken into consideration. Four cases of different arrays of elastic cylinders are implemented in WAMIT, and the results of surface wave elevations are discussed. The objective is to investigate the phenomenon that the incident waves may be trapped and attenuated within the cylinder array, which is analogous to the attenuation effect that occurs when an acoustic wave propagates through bubbly water.

4.1. Diffraction and Radiation of Arrays of Elastic Cylinders

The final step of this study is to activate generalized body modes for the cylinders in WAMIT so that we can obtain the wave interactions of deformable cylinder arrays with both radiated and diffracted waves included. For this purpose, three cases of deformable cylinder arrays have been performed in WAMIT. The setup of those cases is shown in Table 4.1. The wave periods in the first three cases are 20s. The first one is a 49-cylinder case and the only generalized body mode considered in this case is the “breathing” mode. The second one is a 2 by 50 cylinder case. The third one has 200 elastic cylinders, arranged in a 4 by 50 array. The last case has the same array as the third one, but the wave period of this case is 12s. All cases have nine generalized modes activated except for the first one.

Table 4.1 Deformable cylinder array cases studied in WAMIT.

	Case D1	Case D2	Case D3	Case D4
Columns	1	2	4	4
Rows	49	50	50	50
Total	49	100	200	200
Length	727.5m	742.5m	742.5m	742.5m
Wave period	20s	20s	20s	12s
Modes considered	"breathing" mode	all nine modes	all nine modes	all nine modes

Table 4.2 Input parameters for WAMIT in the cases of deformable cylinder arrays.

Parameter	Value
Water depth, $\boldsymbol{h}$	10.5m
Wave period, $\boldsymbol{T}$	20s
Wavenumber outside array, $\boldsymbol{k}$	$0.0315 m^{-1}$
Incident wave angle, $\boldsymbol{\theta}$	0
Incident wave amplitude, $\boldsymbol{A}$	1
Radius of cylinder, $\boldsymbol{R}$	4.3m
Draft of cylinder, $\boldsymbol{d}$	10.5m
Spacing between cylinders, $\boldsymbol{a}$	15m
Filling ratio, $\boldsymbol{fs}$	0.2582
Gravitational acceleration, $\boldsymbol{g}$	$9.81 m/s^2$

Input parameters for the WAMIT can be found in Table 4.2. The results of all four cases are shown from Figure 4.1 to Figure 4.20. The radiated wave fields are shown in Figures 4.1, 4.3, 4.8, 4.13 and 4.18, while the free surface elevations associated with both radiation and diffraction are represented in Figures 4.5, 4.10, 4.15 and 4.19.

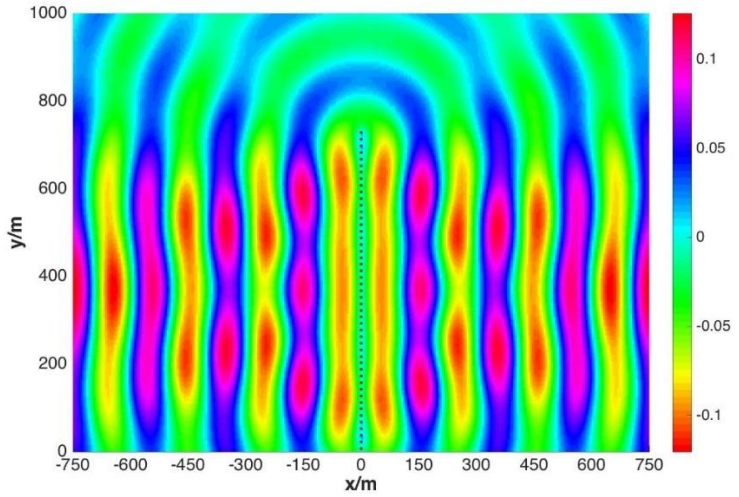

Figure 4.1. Radiated wave field for the 50 deformable cylinders with an incident wave of 20s period.

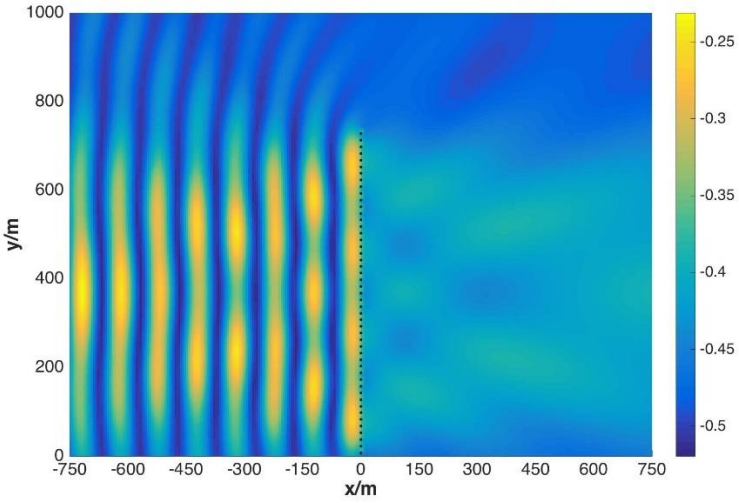

Figure 4.2. Anomaly for the 50 deformable cylinders with an incident wave period T=20s. Both radiation and diffraction are included.

For cases D2, D3 and D4, a comparison of the surface elevation contributions from the diffraction and the radiation is executed from WAMIT's output. First the cylinders are treated as rigid bodies that cannot deform, then the radiation is added to get the complete wave field of the deformable cylinder problem. The objective of this comparison is to analyze the effect caused by the vibration of cylinders. Results are shown in Figures 4.4, 4.5, 4.9, 4.10, 4.14 and 4.15. For those plots the surface wave elevation is determined from only the real part of WAMIT's result, therefore the phase difference is not presented. Only diffraction problem is considered in Figures 4.4, 4.9 and 4.14, while in Figures 4.5, 4.10 and 4.15 both radiation and diffraction are calculated. The wave fields in those two figures seem to be similar, however there exists difference in term of the position of amplitude changes. In Figure 4.4, where waves are only diffracted by rigid cylinders, a variation of wave amplitude can be observed on the incident wave side, while the wave pattern on the transmitted side is much more stable. However, on the contrary, the transmitted wave in Figure 4.5 is more disturbed than the waves coming from the incident side. This is due to the fact that in Figure 4.5, the wave radiated by the vibrating cylinders not only compensates the reflected waves on the left hand side, but also disturbs the transmitted waves on the right hand side.

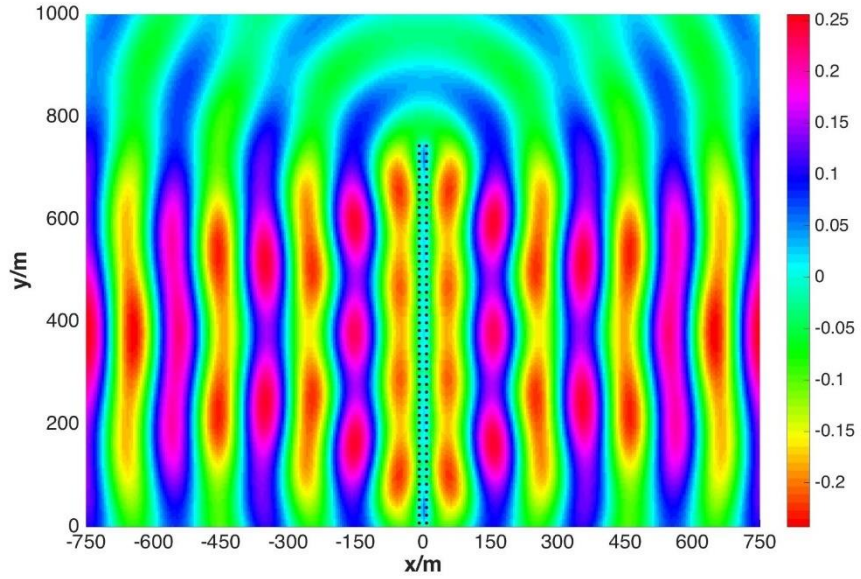

Figure 4.3. Radiated wave field for the 2 by 50 deformable cylinders with an incident wave period T=20s.

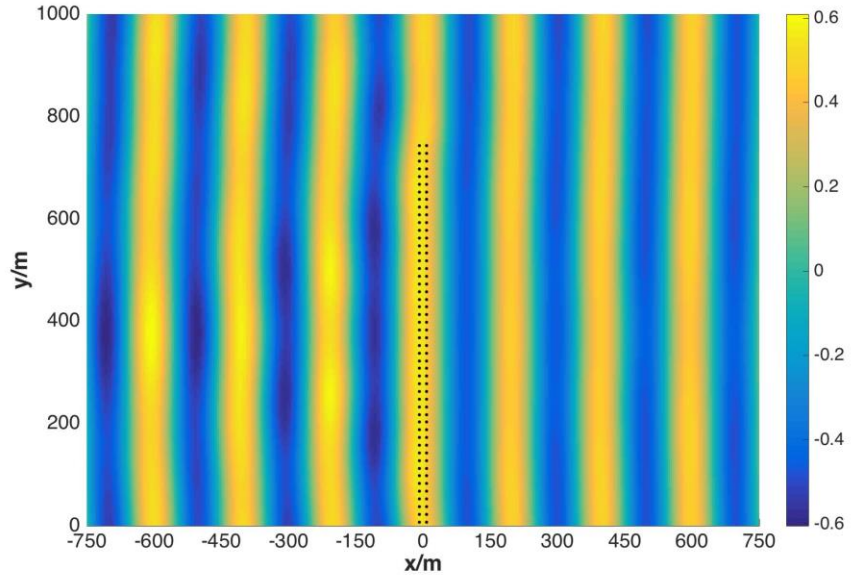

Figure 4.4. Diffraction wave surface elevation for the 2 by 50 deformable cylinders with an incident wave period T=20s.

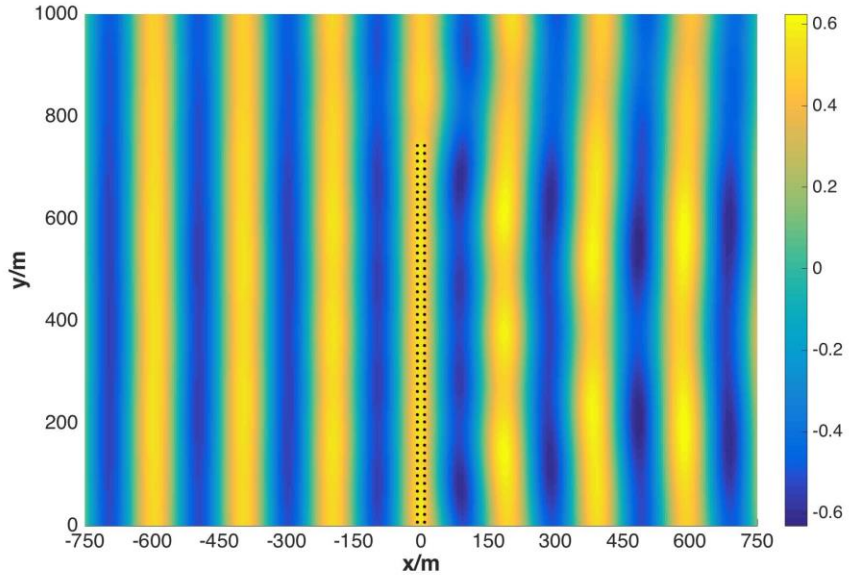

Figure 4.5. Diffraction and radiation wave surface elevation for the 2 by 50 deformable cylinders with an incident wave period T=20s.

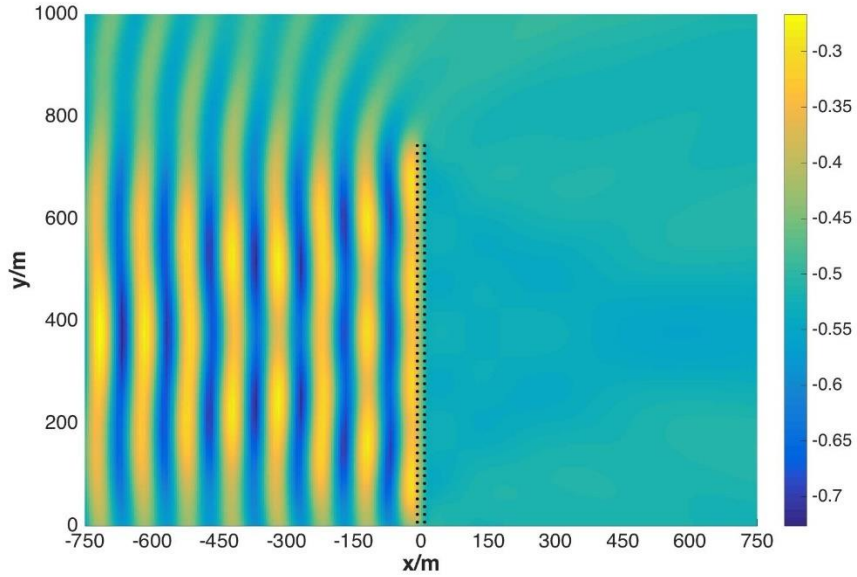

Figure 4.6. Anomaly for the 2 by 50 deformable cylinders with an incident wave period T=20s. Only diffraction problem is included.

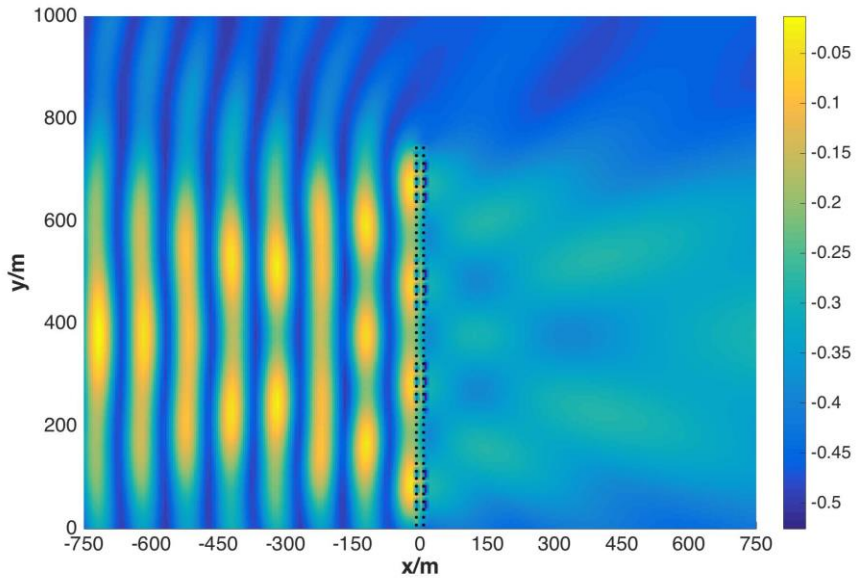

Figure 4.7. Anomaly for the 2 by 50 deformable cylinders with an incident wave period T=20s. Both radiation and diffraction are included.

To better reveal the contribution from radiation, we can apply the anomaly analysis to this comparison. From Figure 4.6 and Figure 4.7, one can notice that the contribution from radiation is easy to identify, as the range of surface elevation changes from [-0.05, -0.5] to [-0.3, -0.7] as the radiation is introduced in Figure 4.7. In addition, when the cylinders are radiating waves, the variation of wave amplitude is more obvious on both sides of the array. The "tip effect" can be seen on the plot where only the contribution of wave elevation from diffraction is considered.

From Figure 4.10 and Figure 4.15, one can observe that for the same 4 by 50 array, the variation of wave amplitude becomes easier to identify as the incident wave length decreases. For the 12s case the "focusing" area where the wave amplitude is relatively larger than the surrounding area is also more obvious.

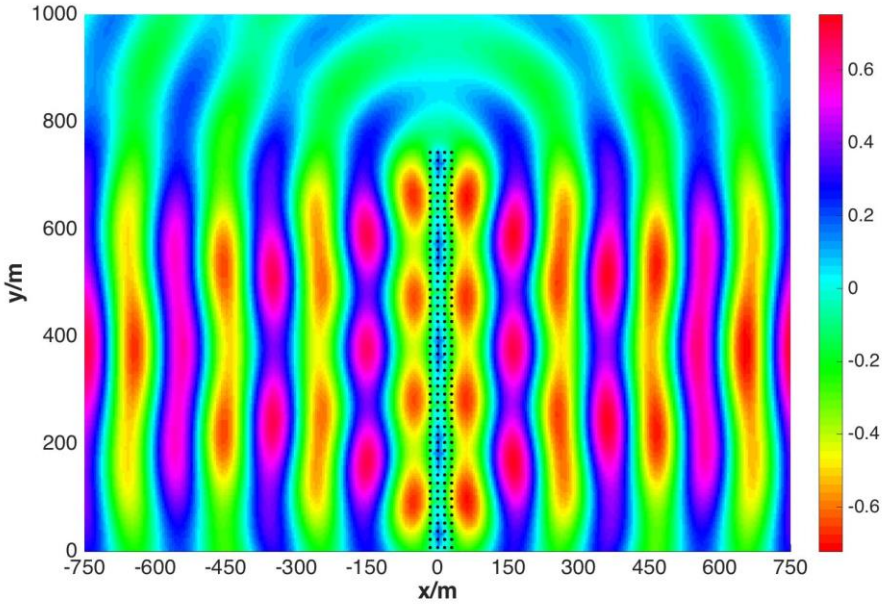

Figure 4.8. Radiated wave field for the 4 by 50 deformable cylinders with an incident wave period T=20s.

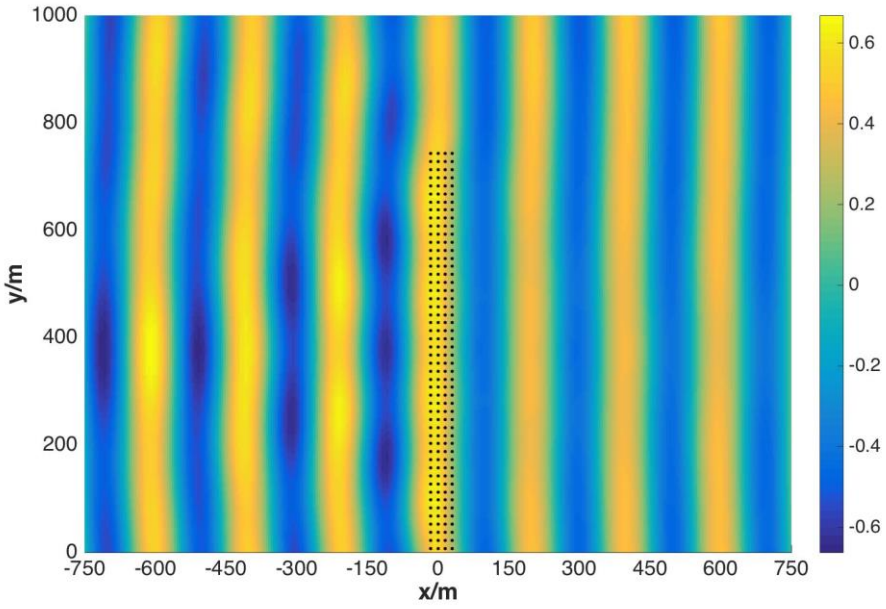

Figure 4.9. Diffraction wave surface elevation for the 4 by 50 deformable cylinders with an incident wave period T=20s.

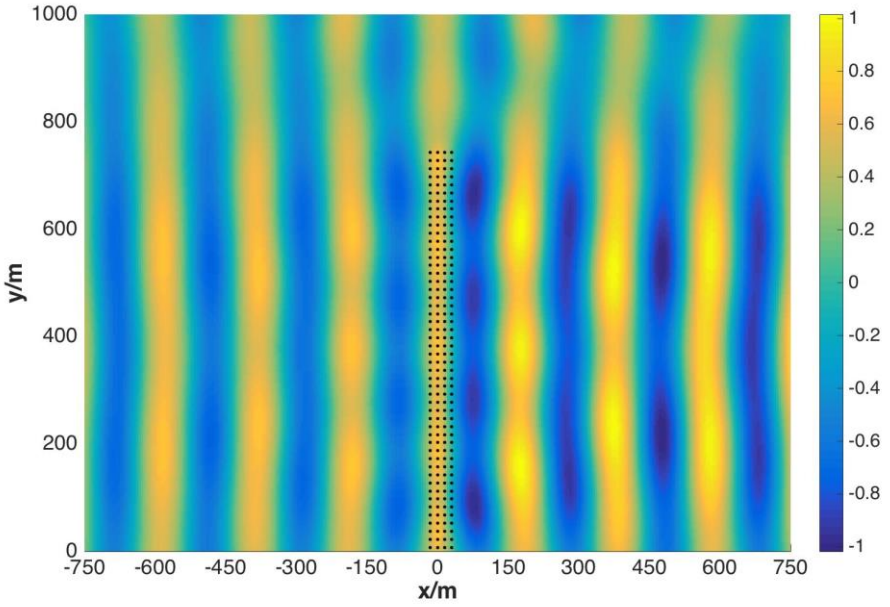

Figure 4.10. Diffraction and radiation wave surface elevation for the 4 by 50 deformable cylinders with an incident wave period T=20s.

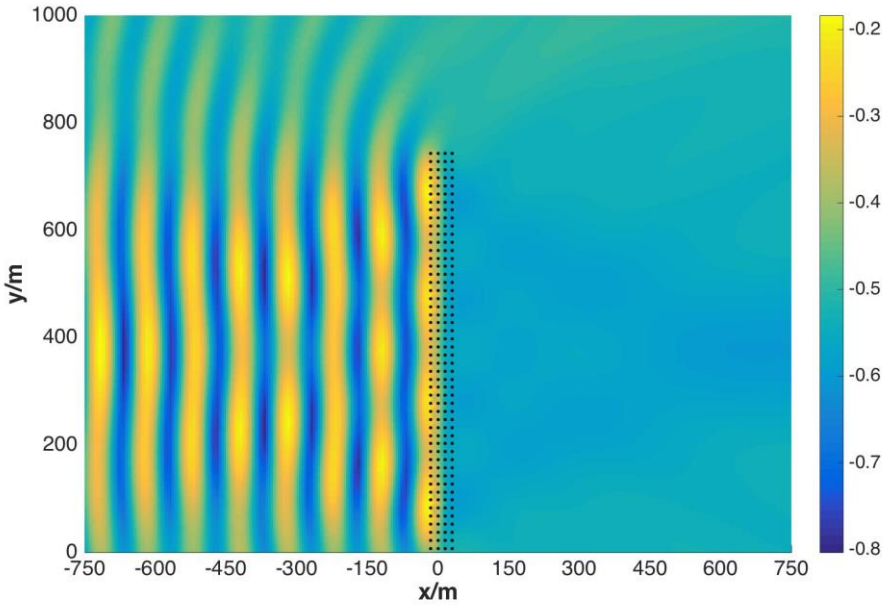

Figure 4.11. Anomaly for the 4 by 50 deformable cylinders with an incident wave period T=20s. Only diffraction problem is included.

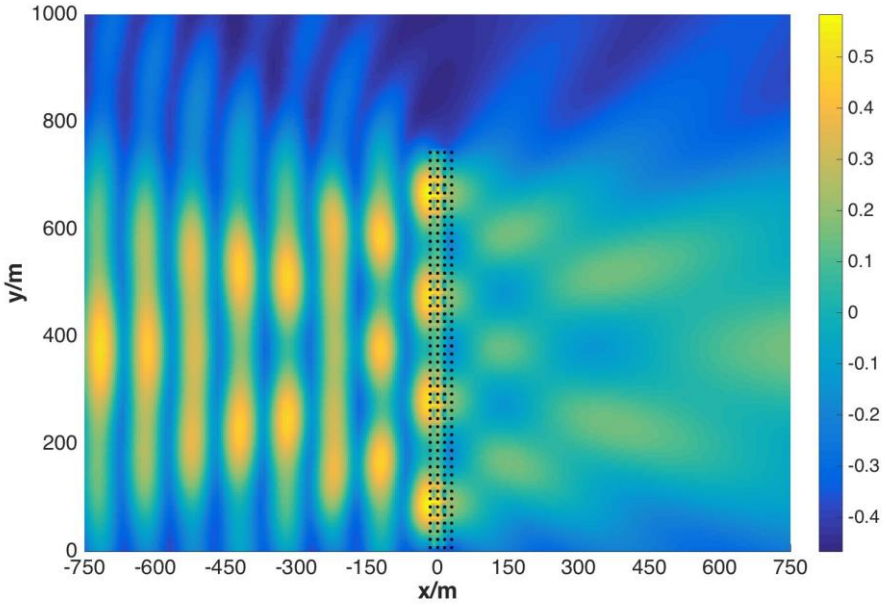

Figure 4.12. Anomaly for the 4 by 50 deformable cylinders with an incident wave period T=20s. Both radiation and diffraction are included.

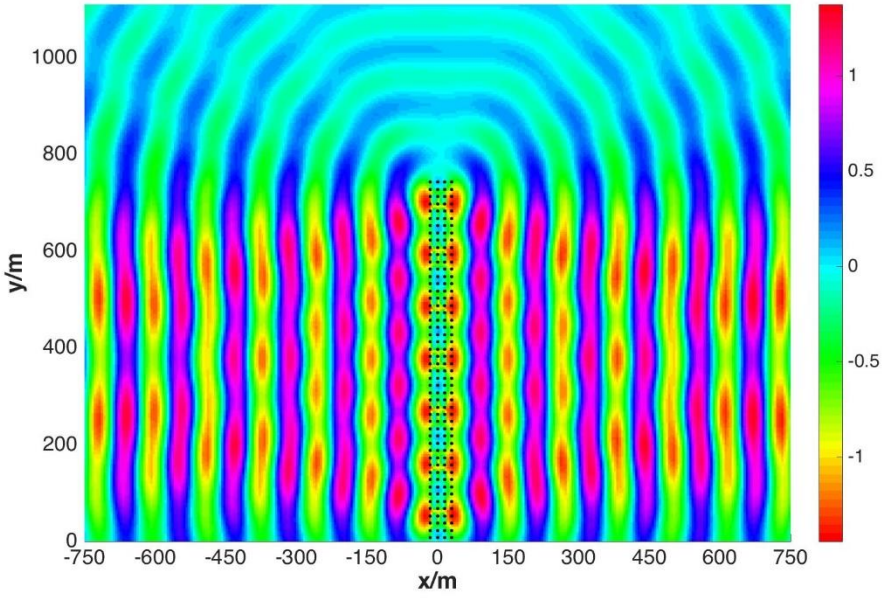

Figure 4.13. Radiated wave field for the 4 by 50 deformable cylinders with an incident wave period T=12s.

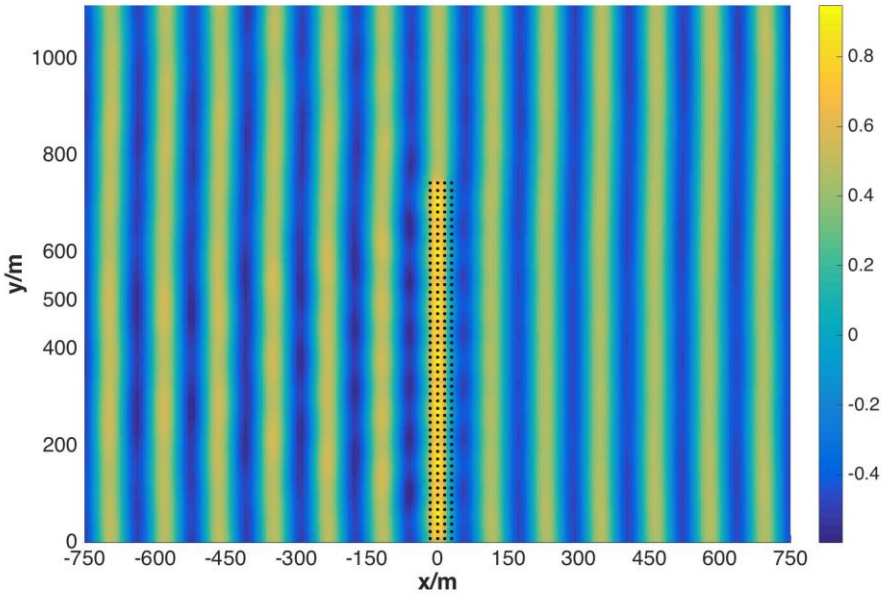

Figure 4.14. Diffraction wave surface elevation for the 4 by 50 deformable cylinders with an incident wave period T=12s.

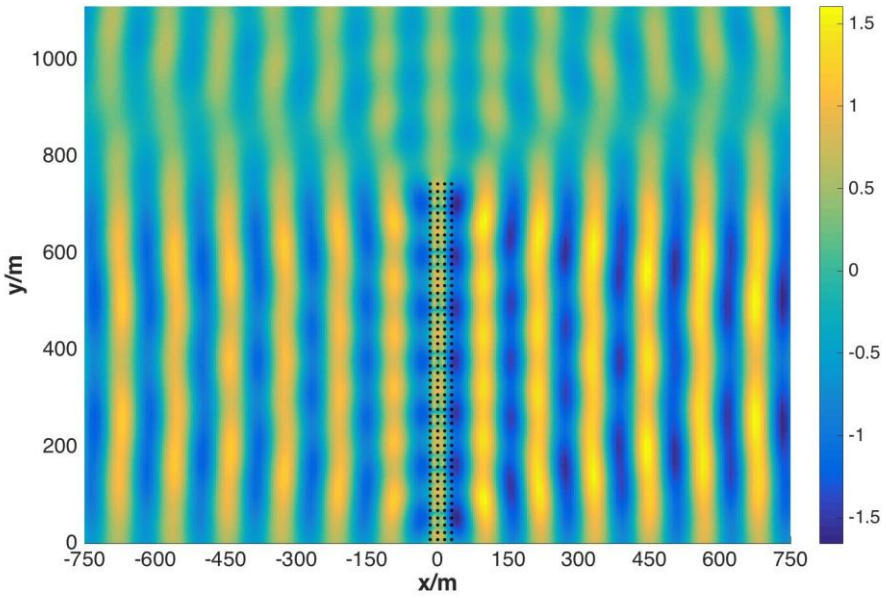

Figure 4.15. Diffraction and radiation wave surface elevation for the 4 by 50 deformable cylinders with an incident wave period T=12s.

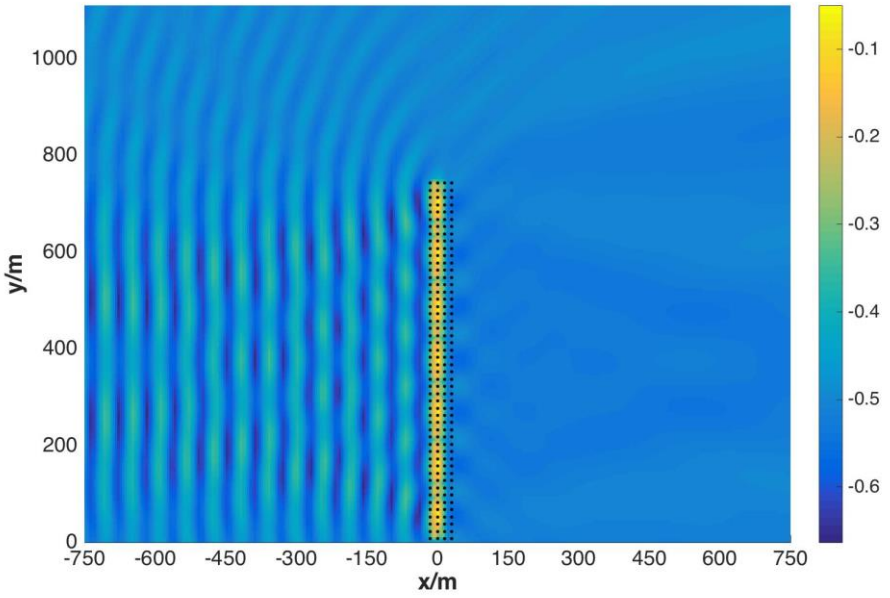

Figure 4.16. Anomaly for the 4 by 50 deformable cylinders with an incident wave period T=12s. Only diffraction problem is included.

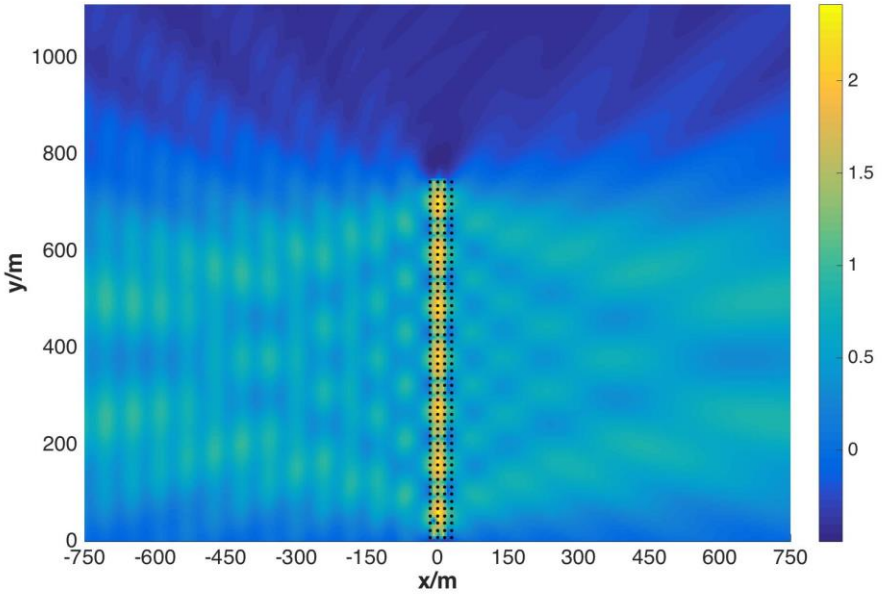

Figure 4.17. Anomaly for the 4 by 50 deformable cylinders with an incident wave period T=12s. Both radiation and diffraction are included.

In addition, the radiated wave component that caused by the first mode (the "breathing" mode) is extracted from the nine modes, and the associated radiation and diffraction surface elevations and anomaly of this single mode are plotted in Figures 4.18, 4.19 and 4.20. Comparing Figures 4.13, 4.15 and 4.17 with Figures 4.18, 4.19 and 4.20, one can find that the radiated wave field generated from all nine generalized modes appears to be similar as the radiated wave field caused by only the "breathing" mode. This similarity has further verified the previous conclusion that the contribution from higher body modes is very small comparing to lower modes.

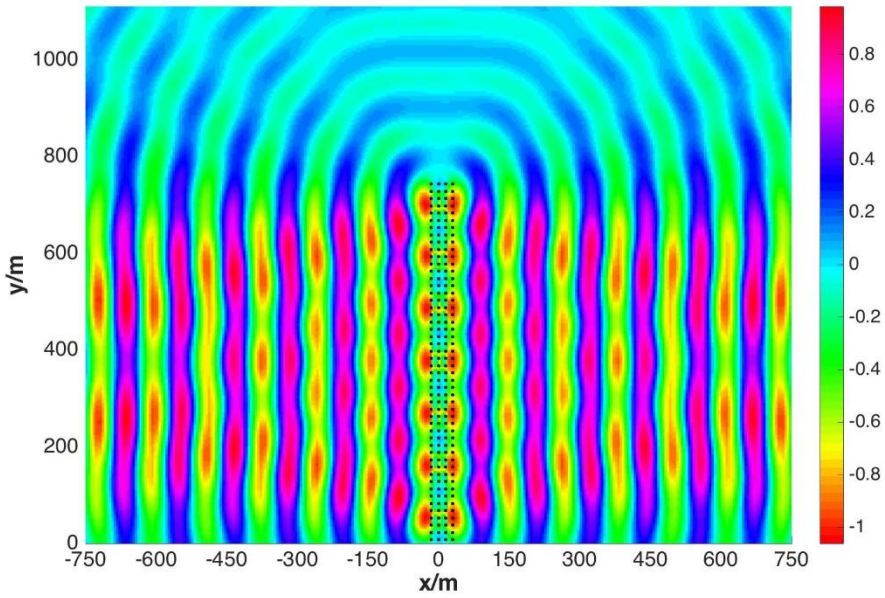

Figure 4.18. Radiated wave field of the first mode ("breathing" mode) for the 4 by 50 deformable cylinders with an incident wave period T=12s.

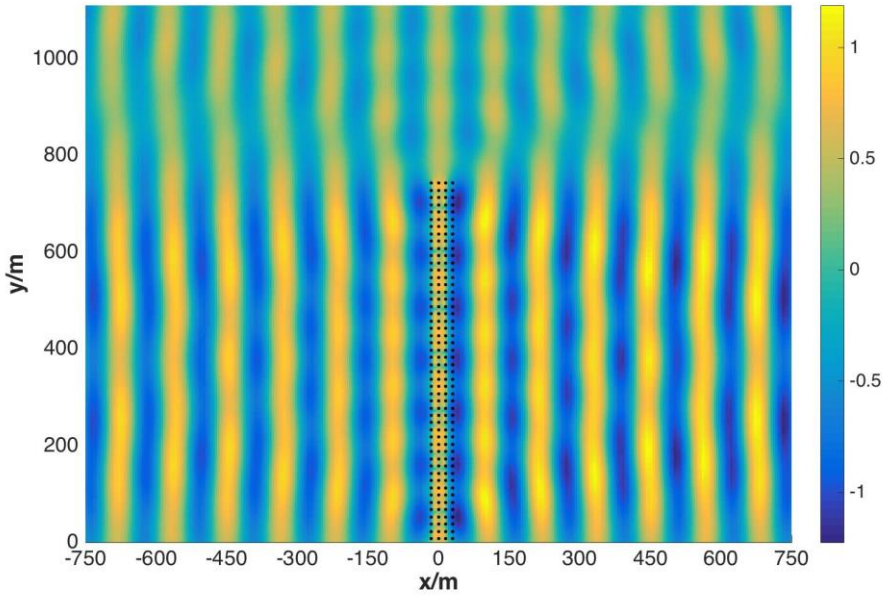

Figure 4.19. Diffraction and radiation wave surface elevation for the 4 by 50 deformable cylinders with an incident wave period T=12s. Only the first mode ("breathing" mode) is included.

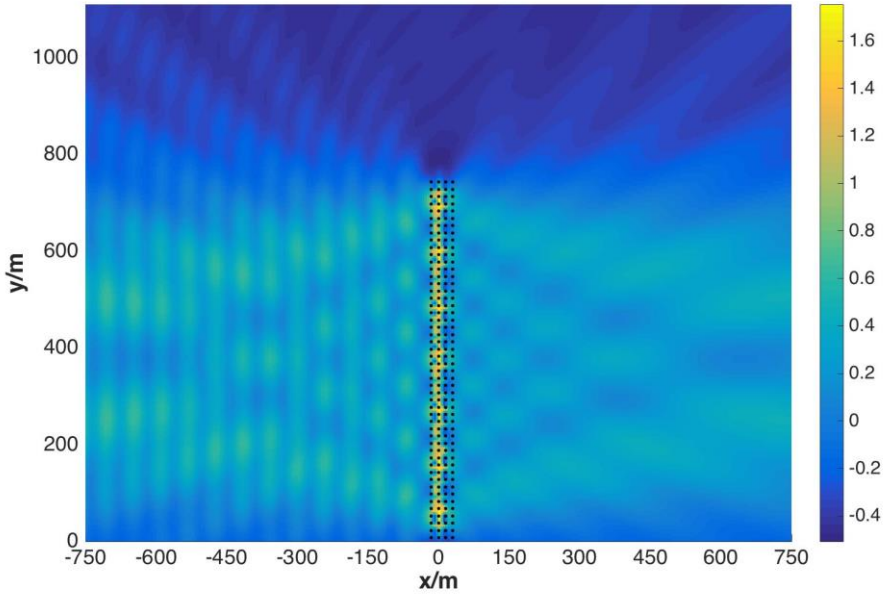

Figure 4.20. Anomaly for the 4 by 50 deformable cylinders with an incident wave period T=12s. Both radiation and diffraction problems are considered. Only the first mode ("breathing" mode) is included.

4.2. Reflection and Transmission Coefficients of Arrays of Elastic Cylinders

The reflection and transmission coefficients for the completed deformable cylinder cases are listed in Table 4.3. To further compare the cases where the cylinders are rigid with the cases that the cylinders are deformable, and to analyze contribution from the radiation, the coefficients associated with the diffraction problem for the same arrays are also provided. In addition, for the case D4, the reflection and transmission coefficients associated with the situation where only the "breathing" mode is included are calculated. As we can see in the table, when the radiation is included, the calculated transmission coefficients tend to be larger than those in the rigid cylinder cases. However, we expected the transmission coefficients to decrease when the radiation is added to the cases. This indicates that for the cases currently studied, the trapping of waves has not yet been reached.

Table 4.3 Reflection and transmission coefficients for the deformable cylinder cases.

Case	Array size	Generalized modes considered	Wave period	Include radiation	Reflection coefficient	Transmission coefficient
D1	1 by 50	"breathing" mode	20s	No	0.5016	0.4944
				Yes	0.4672	0.5202
D2	2 by 50	9 modes	20s	No	0.5015	0.4840
				Yes	0.4740	0.5196
D3	4 by 50	9 modes	20s	No	0.4915	0.4655
				Yes	0.4942	0.6084
D4	4 by 50	9 modes	12s	No	0.5028	0.4832
				Yes	0.6987	0.7845
D4	4 by 50	"breathing"mode	12s	Yes	0.5771	0.6372

4.3. Response Amplitude Operator (RAO) of Arrays of Elastic Cylinders

In Figure 4.21, the RAOs of the cylinders for the case of 4 by 50 cylinders is plotted with respect to the cylinder index. The index of the cylinders always increases in the positive directions of the x-axis and the y-axis. As we can see in the plots, for the 1st and 2nd generalized body modes, larger RAOs can be found on the cylinders in the first edge of the effective medium. The incident wave encounters those cylinders first, and therefore the ratio of the cylinder's motion to the wave amplitude causing that motion becomes higher. However, for other modes, the largest RAOs are identified on the second column of cylinders in the 4 by 50 cylinders array.

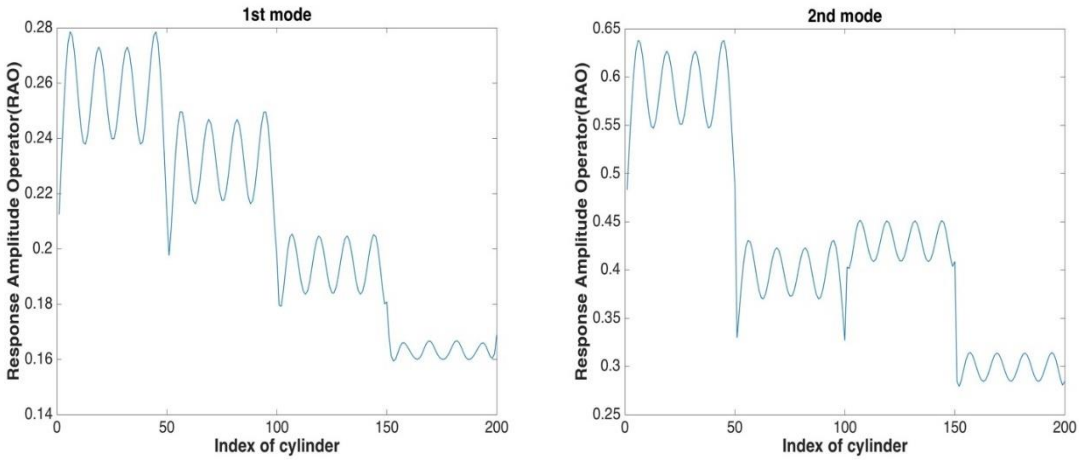

Figure 4.21. RAO for the first six generalized modes in the case of 200 elastic cylinders.

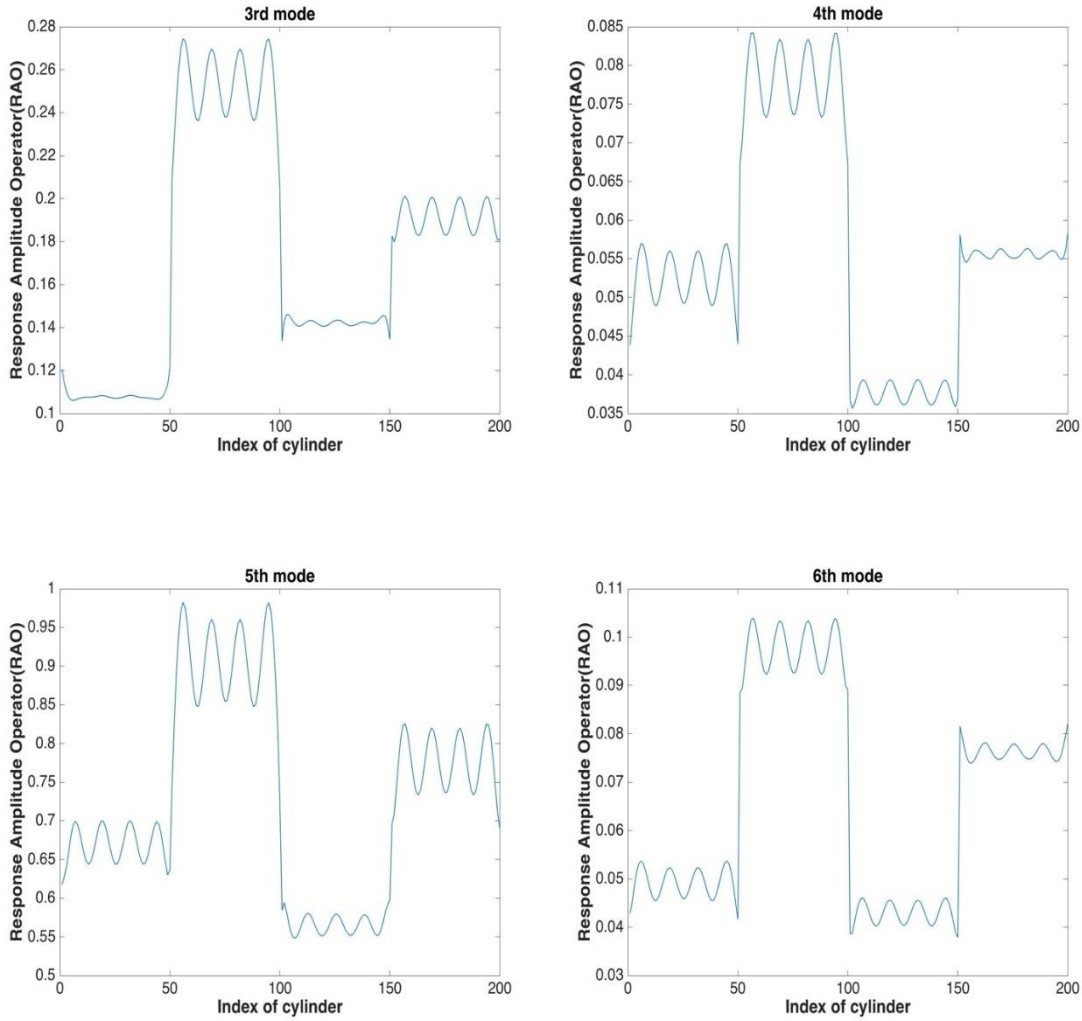

Figure 4.21. Continued.

4.4. Relation Between Radiation and Scattering

Although the scattering problem is different from the radiation, there exist certain relationships between them. In our analysis of wave interactions with elastic cylinder arrays, attention is mainly focused on the relationships between the reflection and transmission coefficients of the scattered waves and the radiated wave amplitudes. The objective of this analysis is to verify that the energy is conserved during the refraction process. Newman (1975) related the properties of the scattering problem and the radiation

problem for the interaction of an incident plane progressive wave system with a cylinder body. His analytical solutions have been used in this study to verify WAMIT's results of surface elevations of radiated and diffracted wave field.

At large distances from the body, on the free surface, the radiation potential can be expressed as

$$\phi_R \sim A_{\pm} e^{\mp iKx}, x \to \pm\infty \tag{4.1}$$

where $A_{\pm}$ are complex coefficients, representing the wave amplitude and phase at infinity.

For the scattering problem, the body is stationary, and at infinity on the free surface the scattering wave potential is

$$\phi_S \sim \begin{cases} e^{iKx} + Re^{-iKx}, & x \to +\infty \\ Te^{iKx}, & x \to -\infty \end{cases} \tag{4.2}$$

where *R* and *T* are the complex reflection and transmission coefficients. Here, e^{iKx} represents the incident wave of unit amplitude.

Define the composite potential

$$\phi_C = \phi_R - (\frac{A_-}{T})\phi_S \tag{4.3}$$

such that there are no waves at $x = -\infty$.

On the free surface at infinity, the composite potential should satisfy the following boundary condition:

$$\phi_c \sim \begin{cases} \left(A_+ - \frac{A_- R}{T}\right) e^{-iKx} - (\frac{A_-}{T}) e^{iKx}, & x \to +\infty \\ 0, & x \to -\infty \end{cases} \tag{4.4}$$

whereas on the cylinder body,

$$\frac{\partial \phi_C}{\partial n} = f \tag{4.5}$$

Here *f* is a given function of position on the body.

Assuming that the body geometry and wavelength are such that complete reflection is impossible, the upstream standing wave for the boundary-value problem $\psi_c = Im(\phi_C)$ must vanish. Therefore, the imaginary part of equation (4.4) must be zero,

$$Im\left[\left(A_+ - \frac{A_- R}{T}\right)e^{-iKx} - \left(\frac{A_-}{T}\right)e^{iKx}\right] = 0 \tag{4.6}$$

which means

$$A_+ - \frac{A_- R}{T} + \frac{A_-^*}{T^*} = 0 \tag{4.7}$$

where an asterisk denotes a complex conjugate. Multiplying the complex conjugate of the above equation by *R*, and adding this product to itself, we have

$$A_+ + A_+^* R + \frac{A_-^*(1 - RR^*)}{T^*} = 0 \tag{4.8}$$

From conservation of energy,

$$RR^* + TT^* = 1 \tag{4.9}$$

From equation (4.8) and (4.9), we have

$$A_+ + A_+^* R + A_-^* T = 0 \tag{4.10}$$

Equation (4.8) and equation (4.10) are used to verify the relation between scattering and radiation problem for the three elastic cylinder cases. The selected field points for this calculation are in the area close to the x-axis, which indicates they are less affected by the tip effect. The reflection and transmission coefficients are derived from WAMIT's numerical results as in the previous section of rigid cylinder arrays. The complex coefficients for the radiated wave can be found in the .6p output file from WAMIT. The results are shown in Table 4.4, where we can see that equation (4.8) and (4.10) are satisfied for the WAMIT cases of elastic cylinders. Therefore, the energy is conserved during the diffraction and radiation processes.

Table 4.4 Relation of radiation and scattering problems for the elastic cylinder cases.

	Case D1	Case D2	Case D3
Equation (4.8)	0.00107+0.0005i	0.00124+0.0009i	0.00079+0.001i
Equation (4.10)	0.00082+0.0008i	0.00101+0.0011i	0.00058+0.0002i

5. SUMMARY AND CONCLUSIONS

In this research, wave interactions with arrays of bottom-mounted vertical circular cylinders have been studied. The main objective is to study the degree to which the incident waves may be trapped inside the cylinder array, and to investigate acoustical and optical analogies. In fact, in the field of acoustics, an incident acoustic wave of certain frequency may be attenuated when it propagates through a layer of a bubbly liquid.

The research starts with the wave interactions with arrays of bottom-mounted rigid cylinders, which simplifies the problem and enables us to verify the setup for the WAMIT program. Hu and Chan's (2005) effective medium approach and the theory of the Fabry-Pérot interferometer are integrated to predict the coefficients associated with the reflection and transmission processes when incident waves encounter the rigid cylinder array, and the theoretical results are compared with WAMIT's numerical output. The equations of motion for a single elastic cylinder exposed to incident waves are derived, and the analytical expressions for the added mass, radiation damping, and exciting force are determined, as well as those for the structural mass and stiffness of the cylinder in the generalized modes of interest. Hydro-elastic analysis is then performed using WAMIT, and the numerical results are shown to match those obtained from the theoretical derivations. For the last step of this research, generalized modes are activated for the cylinder arrays, and hence the radiation problem is taken into account.

This research is the continued work of the master's thesis of Aldric Baquet (2010), who is a former student of Dr. Richard S. Mercier. Because of the large number of cylinders and the nine generalized body modes considered for each cylinder, the computational time for the case of arrays of deformable cylinders is very large. Each of the cases requires about one week to complete the POTEN part of WAMIT. The FORCE

part takes even longer when we have a great number of field points. Therefore, the outcome of this research is limited because of the huge computational effort involved.

The following conclusions can be made from this research:

i. The application of the effective medium approach in our research is successful. When integrated with the effect of the Fabry-Pérot interferometer, the approach can predict model reflection and transmission by a cylinder array. The pseudo-inverse method can be used to process WAMIT's surface elevation output, and hence evaluate reflection and transmission coefficients for the array. The results present a good agreement with those determined by the effective medium approach.

ii. A set of equations of motion of the pulsating cylinder can be derived according to the theory of vibrating thin shells. Added mass, radiation damping, and exciting force were calculated from the velocity potentials and expressed in matrix form. Agreement with WAMIT's numerical results has been reached. This indicates that our analytical formulas are valid and can be further incorporated into WAMIT in the hydro-elastic analysis of vibrating cylinders.

iii. The modal superposition method is successfully applied in the research. If the elastic cylinder is undergoing free vibrations, the total displacements in the vertical, tangential and radial directions can be expanded into Fourier series. Generalized body modes have been added into WAMIT's NEWMODE subroutine. These modes are circumferential modes and they describe the radial deformations of the cylinder.

iv. The cylinder must be considered as filled with water in order to equilibrate the exterior hydrostatic pressure since the cylinder shell is very flexible. This means that the interior modes of fluid motion must be considered in the model.

v. Values of cylinder dimensions and material properties have been selected to set the natural period at the lower end of the studied wave band. However, those dimensions may not ensure the water is shallow enough. Therefore, a redesign process might be needed.

vi. Analytical expressions of the reflection index, reflectance, and transmittance of the rigid cylinder arrays have been formulated. The values are in good agreement with those determined from WAMIT's output file of wave elevation using the pseudo-inverse method.

vii. When the length of the array is finite, a so-called "tip effect" can be observed at the top end of each array, where the wave field is more interfered than the area near the plane of symmetry through the middle of the array. In addition, the intensity of the effect changes with the array length. Throughout the different arrays of cylinders studied in the research we can easily notice a weaker disturbance of the wave amplitude for a longer array.

viii. The "tip effect" can affect the transmitted wave amplitude, and hence the reflection and transmission coefficients identified from WAMIT's result. Therefore, it is not possible to identify the transmitted wave component using the surface elevation data on the field points that are close to the tip.

ix. For a given (m,n) mode, the natural period of the elastic cylinder that is not filled with water can be determined by finding the roots of the characteristic equation. The natural period of the cylinder filled with water can be obtained from the plots of RAO for certain modes, and the result is consistent with the theoretical values.

x. As the mode index goes higher, its contribution of the radiated wave to the total wave surface elevation becomes smaller or even negligible.

xi. The anomaly detection is proved to be effective in term of revealing the changes of wave amplitude in the wave domain, and hence the "tip effect" occurring at the ends of the arrays. In order to obtain the anomaly of the surface elevations, we can subtract the incident wave from WAMIT's output of the refracted wave field.

xii. For the elastic cylinder cases, the relationships between the reflection and transmission coefficients of the scattered waves and the radiated wave amplitudes are verified.

xiii. When the radiation problem is added in the elastic cylinder cases, the transmission

coefficients become larger than those in the cases where only the diffraction problem is considered. Therefore, for the combinations of the wave conditions, the deformable cylinder array sizes and the cylinder dimension currently studied in this research, a significant attenuation of waves has not yet been found.

The future work for this research would be looking for the combination of wave condition, cylinder array size and cylinder dimension that can cause a trapping of waves inside the array. It can also be focused on conducting experimental tests for the elastic cylinder arrays. Redesigning the cylinder dimensions and material properties may be needed during the process. It would also be interesting to investigate the number of cylinders needed that will cause a significant attenuation given a certain wave condition.

In this research, periodic spacing is used for the cylinder arrays in order to reduce the computational effort. It will be more analogous to the acoustic problem if random spacing is introduced in the study.

REFERENCES

Baquet, A., 2010. Wave interactions with arrays of bottom-mounted circular cylinders: Investigation of optical and acoustical analogies. Master's thesis. Texas A&M University, College Station, Texas.

Commander, K.W., Prosperetti, A., 1989. Linear pressure waves in bubbly liquids: Comparison between theory and experiments. J. Acoust. Soc. Am. 85 (2), 732-746.

Dean, R.G., Dalrymple, R.A., 1991. Water wave mechanics for engineers and scientists. Advanced Series on Ocean Engineering. 2, 171-185.

Evans, D., Porter, R., 1997. Near-trapping of waves by circular arrays of vertical cylinders. Applied Ocean Research. 19, 83–99.

Goncalves, P.B., Ramos, N.R.S.S., 1996. Free vibration analysis of cylindrical tanks partially filled with liquid. J. Sound and Vibration. 195 (3), 429–444.

Hu, X., Chan, C.T., 2005. Refraction of water waves by periodic cylinder arrays. Physical Review Letters. 95, 154501, 1-4.

Junger, M.C., Cole, J.E., 1980. Bubble swarm acoustics: Insertion loss of a layer on a plate. J. Acoust. Soc. Am. 68 (1), 241-247.

Koga, T., Tsushima, M., 1990. Breathing vibrations of a liquid-filled circular cylindrical shell. Int. J. Solids Structures. 26 (9-10), 1005-1015.

Lee, K.M., Hinojosa, K.T., Wochner, M.S., Argo, T.F., Wilson, P.S., Mercier, R.S., 2011. Sound propagation in water containing large tethered spherical encapsulated gas bubbles with resonance frequencies in the 50 Hz to 100 Hz range. J. Acoust. Soc. Am. 130 (5), 3325-3332.

Leissa, A.W., 1973. Vibration of shells. Scientific and Technical Information Office, NASA, SP-288, 31-184.

MacCamy, R.C., Fuchs, R.A., 1954. Wave forces on piles: A diffraction theory. Technical Memorandum No.69, U.S. Beach Erosion Board.

Newman, J.N., 1975. Interaction of waves with two-dimensional obstacles: A relation between the radiation and scattering problems. J. Fluid Mech. 71(02), 273 - 282.

Newman, J.N., 1994. Wave effects on deformable bodies. Applied Ocean Research. 16, 47-59.

Van Wijngaarden, L., 1968. On equations of motion for mixtures of liquid and gas bubbles. J. Fluid Mech. 33, 465-474.

Wang, K., Ye, Z., 2001. Acoustic pulse propagation and localization in bubbly water. Phys. Rev. E. 64, 056607, 1-9.